CHIRALITY AND ITS SPONTANEOUS SYMMETRY BREAKING IN TWO LIQUID CRYSTAL SYSTEMS

Louis Kang

A DISSERTATION

in

Physics and Astronomy

Presented to the Faculties of the University of Pennsylvania

in

Partial Fulfillment of the Requirements for the

Degree of Doctor of Philosophy

2015

Supervisor of Dissertation

_____

Tom C. Lubensky, Professor of Physics and Astronomy

Graduate Group Chairperson

_____

Marija Drndic, Professor of Physics and Astronomy

Dissertation Committee

Andrea J. Liu, Professor of Physics and Astronomy

Bhuvnesh Jain, Professor of Physics and Astronomy

Paul A. Janmey, Professor of Physiology

Philip C. Nelson, Professor of Physics and Astronomy

CHIRALITY AND ITS SPONTANEOUS SYMMETRY BREAKING IN TWO LIQUID CRYSTAL SYSTEMS

COPYRIGHT

2015

Louis Kang

Dedication

For Yan and Bowen.

Acknowledgments

Many people have made this dissertation possible and my time pursuing it wonderful.

I am extremely fortunate to have started my scientific journey under the direction of my advisor Tom Lubensky. Beyond knowledge and reason, through words and by example, Tom has helped me become more creative, open-minded, generous, responsible, and fair. His wisdom will follow me and those with whom I interact throughout my career. Andrea Liu also provided indispensable guidance, especially at the start of graduate school as I was first introduced to research. She helped me through the difficulties and disorientation of my first two years and has continued to support me through the last two.

Penn Physics has been a great home for my graduate education. Randy Kamien challenged me with lively discussions, expanded my understanding with his unique insights, and opened me to the power of peat. Timon Idema helped me through my first project. I also thank the rest of the soft matter theory group for their help and camaraderie, including Natalie Arkus, Ed Banigan, Dan Beller, Toen Castle, Kevin Chiou, Simon Čopar, Xingting Gong, Carl Goodrich, Eric Horsley, Eleni Katifori, Max Lavrentovich, Ricardo Mosna, Jason Rocks, Sam Schoenholz, Francesca Serra, Daniel Sussman, and Lisa Tran. I also thank my cohort with whom we will eternally remain as "first-years": John Briguglio, Jeff Cochran, Zoey Davidson, Sergey Nisnevich, Mehmet Noyan, Madeleine Phillips, Kevin Tian, Davis Varghese, and Rachel Wolf. Support from the administrative staff, including Millicent Minnick, has been unwavering.

I have worked with gifted and charitable experimental collaborators without whom my research would not be possible. They include Peter Collings, Zoey Davidson, Joonwoo

Jeong, Tim Still, and Arjun Yodh; Zvonimir Dogic, Thomas Gibaud, Bob Pelcovits, and Prerna Sharma; Priyanka Kothari and Mike Lampson; and Nam Woo Cho and Roger Greenberg. The Penn MD/PhD program has provided warmth, continuity, and biomedical perspective, including its leaders Skip Brass, Aimee Payne, Maggie Krall, and Maureen Kirsch, and my classmates that include Nam Woo Cho, Michael Nakazawa, Jon Parker, Bo Qiu, and Ashwin Ramayya.

Finally, I thank my friends, Friedi for her love and support, and my parents for the same and all that they have done for me.

ABSTRACT

CHIRALITY AND ITS SPONTANEOUS SYMMETRY BREAKING IN TWO LIQUID CRYSTAL SYSTEMS

Louis Kang

Tom C. Lubensky

Chirality, or handedness, is a key concept spanning all fields of natural science, from biology to mathematics. Chiral structures can arise from achiral building blocks that lack a handedness if their assembly is unstable to chiral deformations, a phenomenon called spontaneous symmetry breaking. We theoretically study the role of chirality in two systems composed of liquid crystals dissolved or suspended in water, and our results match those obtained experimentally by our collaborators. In the first system, we study achiral liquid crystals whose Frank twist modulus is much lower than their splay and bend Frank moduli and which are confined in capillaries. Under homeotropic anchoring, their ground state configuration undergoes spontaneous chiral symmetry breaking when the twist modulus decreases enough relative to the splay and bend moduli. Under degenerate planar anchoring, a small twist-to-saddle-splay ratio of elastic moduli leads to degenerate twisted configurations even though an undeformed configuration is possible. Measuring the twist profile of an experimental system produces a value for the saddle-splay constant, which has been difficult to achieve previously. Under either boundary condition, domain walls and point defects, whose topological charges depend on chirality, separate domains with different degenerate configurations, and certain ones are energetically preferred over others. In the second system, we study filamentous viruses acting as colloidal liquid crystals under the influence of depletion, which promotes condensation of the viruses into 2D colloidal monolayers. These membranes have tunable chirality and show a rich array of emergent behaviors, including a transition from a circular shape to a striking starfish shape upon changing the chirality of constituent viruses, partial coalescence via domain walls through which the viruses twist by 180°, and phase-separated rafts of a particular size when two virus species with different lengths and

opposite chiralities are used. We formulate a simple theory combining Frank elasticity and depletion that shows how entropy and chirality drive the formation and behavior of these diverse structures. Our work may facilitate the design of chiral sensors and reconfigurable materials and suggests that chirality contributes not only biochemically but also physically to the behavior of lipid rafts in biomembranes.

Contents

List of Tables

List of Figures

Chapter 1

Introduction

1.1 Chirality in liquid crystal systems

Chirality is fundamentally encoded into the space in which we live. Any distance preserving-transformation, or isometry, of Euclidean space can be decomposed as a rotation about the origin, a translation, and/or a reflection, which is also known as parity inversion. With the exception of the weak interaction, our current description of physics is invariant under a global parity inversion; however, locally replacing components of a physical system with their mirror images can have a drastic effect. Thus, there is an important distinction between an object that is identical to its mirror image and one whose "image in a plane mirror, ideally realized, cannot be brought to coincide with itself," as stated by Lord Kelvin in 1904 as he coined the term *chirality* [1]. And while rotations and translations are continuous transformations, parity inversion is a discrete transformation, which gives chirality a topological nature, as highlighted by the currently flourishing field of topological materials that possess chiral currents [2, 3]. Yet, despite success in understanding and leveraging chiral systems and anthropomorphic intuition arising from our left and right hands, one should not forget that chirality is a highly nuanced concept. Quantifying the amount or even the absolute sign of chirality in chiral molecules is fraught with difficulties [4, 5].

Chirality played a pivotal role in the discovery of liquid crystals, which are phases of

matter whose symmetries and mechanical properties lie between those of solids and those of liquids. We first review some liquid crystal basics [6, 7]. The uniaxial nematic phase is formed by particles having no positional order but having orientational alignment with their neighbors in either parallel or anti-parallel fashion. The coarse-grained alignment axis can be indicated by a unit vector called the nematic director $\mathbf{n}$ (Fig. 1.1a). Since the particles do not distinguish between head and tail, the direction of $\mathbf{n}$ is only physically meaningful up to an overall sign. Uniform alignment can be distorted by external fields applied to the bulk or by boundary conditions set at the surface of the enclosing container. These distortions, in the long-wavelength limit, can be decomposed into three main elastic modes—splay, twist, and bend—and a fourth mode—saddle-splay—whose elastic energy can be integrated to the boundary (Fig. 1.1b). Large distortions can acquire a topological charge such that the director field cannot be smoothly deformed back to the undistorted state. They are usually accompanied by defect(s) at which $\mathbf{n}$ is not well-defined and the nematic phase is locally melted. Point defects are called hedgehogs and line defects are called disclination lines.

Heating the nematic phase past a critical temperature eliminates its orientational order via a first-order transition and the system becomes a liquid. For some liquid crystals, cooling the nematic phase brings it into a smectic-A phase before it becomes a solid. This transition is second-order in mean-field theory. The smectic gains positional order as a mass density wave in the direction of the nematic director, and it can be conceptualized as equally spaced layers of particles oriented normal to the layers. Distortion of this preferred layered structure leads to two additional elastic modes corresponding to changes in layer spacing and deviations of the director from the layer normal (as well as another saddle-splay mode that can be integrated to the surface). Splay, twist, and bend director modes are still present, though only splay is compatible with the layered structure and existent in the bulk. Smectics exhibit wide array of defects, but their discussion is outside the scope of this overview.

Certain particles with chiral structures prefer to be oriented with some chiral relationship to their neighbors rather than simply parallel or anti-parallel to them. Of the three director

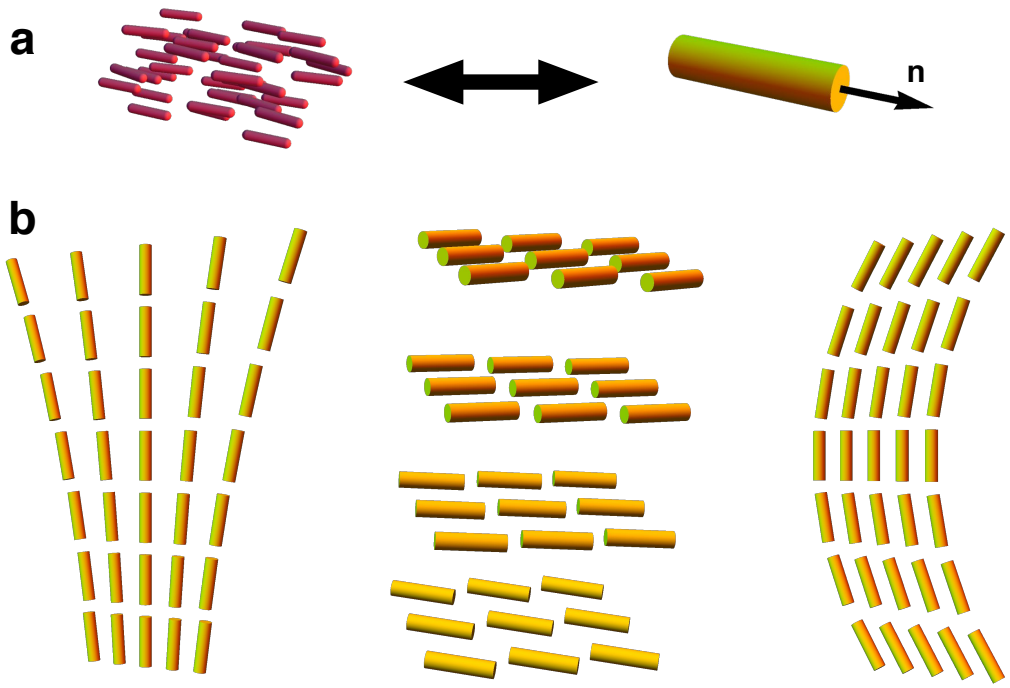

Figure 1.1: The nematic director and its distortion modes. (a) The nematic director $\mathbf{n}$. Anisotropic particles (red spherocylinders) with quadrupolar symmetry may entropically or electrostatically favor local orientational alignment. The coarse-grained alignment axis is called the nematic director $\mathbf{n}$ (yellow cylinder). Notice that $-\mathbf{n}$ could also describe this alignment axis, so $\mathbf{n}$ is only physically meaningful up to an overall sign. (b) From left to right, splay, twist, and bend distortion modes. Splay and bend distortions do not have a handedness, but twist distortion is chiral, and its depiction here is right-handed.

distortion modes, only twist has chirality, so the ground state of a chiral nematic has sponataneous twist of a particular wavelength and handedness. Its elastic modes are still splay, twist, and bend, with twist now taken relative to its preferred value. This chiral nematic, or cholesteric, phase was the first liquid crystalline phase observed in 1888 by Friedrich Reinitzer while investigating cholesteryl esters [8].

Many biological systems, whose building blocks are fundamentally chiral, demonstrate liquid crystalline phases [9, 10]. Cell membranes contain phospholipids which are fluid within the membrane but have orientational order. Not only are these phospholipids chiral, but membranes also contain cholesterol, which as mentioned above, can imbue liquid crystal phases with strong chiral character. Outside of membranes, improper phase separation and accumulation of cholesterols are hallmarks of diseases like atherosclerosis and cholelithiasis (gallstones). Deoxyribonucleic acid (DNA) can form cholesteric phases in mitochondria, as well as many other liquid crystal phases *in vitro* [11]. Protein fibers such as actin, microtubules, and collagen have a helical microstructure and align to form cellular structures such as muscle fibers, cell division spindles, and cornea fibers. Moreover, cellular structures such as chloroplasts and rods can form higher-order aligned structures themselves.

The study of chirality in liquid crystal systems has been fruitful for developing novel technologies. For example, the RealD 3D system used for stereoscopic film projection uses liquid crystals arranged in chiral configurations to simultaneously transmit left-eye images with circularly polarized light of one handedness and right-eye images with light of the other handedness [12]. Viewers wear eyeglasses with circularly polarized lenses of opposite handednesses that allow only the correct images through. This technology requires only one projector and, unlike systems using linearly polarized light, allows the viewer to tilt her head without compromising image separation. Furthermore, achiral liquid crystals that demonstrate spontaneous chiral symmetry breaking show promise for use as sensors of molecular chirality. In an achiral or racemic environment, these liquid crystals will show configurations of either handedness with equal probability, but a chiral imbalance will favor configurations of one handedness over the other. One such system uses the ratio of domains

with left- and right-handed twists in disclination lines as a readout of chirality [13].

1.2 Outline of subsequent chapters

We study the role of chirality in two liquid crystal systems. In Chapter 2, we investigate achiral nematic liquid crystals whose twist Frank constant is much less than their splay, bend, and saddle-splay constants. Experimentally, an aqueous solution of Sunset Yellow FCF (SSY) serves as such a material. When confined into cylindrical capillaries with the director at the capillary surface enforced to be either perpendicular or parallel to the surface, these liquid crystals will undergo spontaneous chiral symmetry breaking and form twisted structures. With perpendicular boundary conditions, the twist-to-bend and twist-to-splay elastic modulus ratios are the control parameters whose values govern this process. With planar anchoring, the twist-to-saddle-splay elastic modulus ratio is the most important control parameter. Comparison of experimentally observed structures using SSY with theory yields a large value for the saddle-splay elastic constant, which is typically difficult to measure, that violates the Ericksen inequalities. Furthermore, for both boundary conditions, chiral degeneracy leads to domain walls and point defects between domains of opposite handedness, with certain stuctures energetically preferred over others.

Chapter 3 describes a liquid crystal system with drastically different dimensionality, particle sizes, and emergent behaviors. Micron-length rod-like viruses with tunable chiral properties can be induced by depleting polymers to form 2D colloidal monolayers that have a rich phenomenology. Membranes formed from a macroscopically achiral mixture of viruses undergo spontaneous chiral symmetry breaking and exhibit twist of either handedness with equal probability. Two membranes of the same chirality can partially coalesce and trap a twist domain wall through which the viruses twist by 180°. Upon a temperature quench, these circular membranes grow twisted arms and adopt a striking starfish shape. Finally, by combining two different virus species, circular rafts of one species form inside a background membrane of the other species. These rafts have a preferred size and repel one another. These diverse behaviors arise in a system with only effective hard-core interactions. We

formulate an entropically-motivated theory that combines Frank elasticity with the depletion interaction to describe how entropy and chirality drive these phenomena. Our results suggest new ways that chirality may influence the properties of biomembranes and new principles that may guide the design of reconfigurable colloidal structures.

Finally, we summarize our work in Chapter 4 and discuss its implications.

Chapter 2

Liquid crystals with low twist modulus confined in capillaries

2.1 Introduction

2.1.1 Confinement-induced chiral symmetry breaking

Elastic deformations of achiral nematic liquid crystals (LCs) can be described by the Frank free energy

$$F = \int \mathrm{d}^3\mathbf{x} \left[\frac{K_1}{2} \left(\mathbf{n}\boldsymbol{\nabla}\cdot\mathbf{n}\right)^2 + \frac{K_2}{2} \left(\mathbf{n}\cdot\boldsymbol{\nabla}\times\mathbf{n}\right)^2 + \frac{K_3}{2} \left(\mathbf{n}\times\boldsymbol{\nabla}\times\mathbf{n}\right)^2 - \frac{K_{24}}{2}\boldsymbol{\nabla}\cdot\left(\mathbf{n}\times\boldsymbol{\nabla}\times\mathbf{n} + \mathbf{n}\boldsymbol{\nabla}\cdot\mathbf{n}\right) \right], \tag{2.1.1}$$

where $\mathbf{n}$ is the nematic director and K_1, K_2, K_3, and K_{24} are respectively splay, twist, bend, and saddle-splay moduli [7, 14, 15]. Note that the K_{24} term can be integrated to the boundary.

Confinement can induce distortion in LC systems that would otherwise prefer to have no distortion. Strong anchoring conditions at the surface of the confining container fix the direction of $\mathbf{n}$. Homeotropic anchoring means that $\mathbf{n}$ must be perpendicular to the boundary surface, degenerate planar anchoring means that $\mathbf{n}$ lies in the plane of the surface

Table 2.1: Bulk elastic moduli of 31.5 w% Sunset Yellow FCF (SSY) and of 4-cyano-4'-pentylbiphenyl (5CB), a typical thermotropic LC, at 25 °C.

LC	K_1 [pN]	K_2 [pN]	K_3 [pN]	Reference
SSY	8.1	0.8	8.7	[26]
5CB	5.2	2.9	6.8	[27]

with no preferred direction, and directional planar anchoring means that **n** points along a particular axis in the plane of the surface. Experimentally, these boundary conditions may be set by the natural properties of the interface or by chemical or mechanical modification of the surface. We study achiral LCs whose twist modulus K_2 is considerably less than their other moduli. In this case, the Frank elastic energy may be minimized when strong splay and/or bend deformations are relieved by twisting. The system undergoes spontaneous chiral symmetry breaking and twisted configurations of either handedness will be found with equal probability.

Confinement-induced chiral symmetry breaking often arises in systems whose boundary conditions are incompatible with a uniform nematic configuration. For example, spherical or tactoidal LC droplets with either homeotropic or degenerate planar anchoring can gain twist when their elastic moduli have enough anisotropy [16–21]. In these cases, most of the director distortion is found around topological defects whose presence is required by the boundary conditions. We explore this phenomenon under a cylindrical confinement geometry with homeotropic anchoring, with defect-free ground states, in Sec. 2.2 [22]. However, confinement with degenerate planar anchoring can also produce chiral symmetry breaking via saddle-splay elasticity, which favors surface alignment along the direction of greatest curvature [23, 24]. Even when a uniform configuration is permitted by the boundary conditions, a difference in the principal curvatures of the boundary surface can induce chiral deformations. We explore saddle-splay-driven chiral symmetry breaking under a cylindrical confinement geometry with planar anchoring in Sec. 2.3 [25].

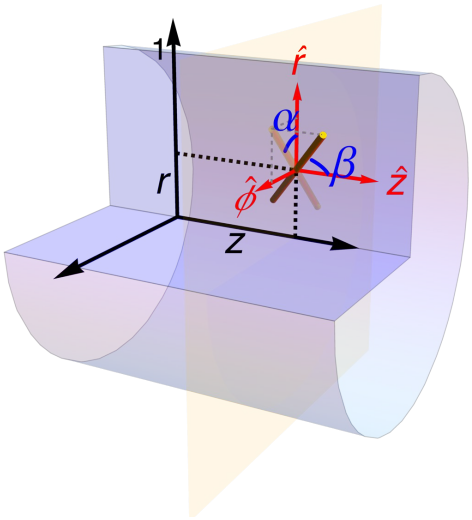

Figure 2.1: Parametrization of the nematic director $\mathbf{n}$ in a capillary. β is the polar angle between $\mathbf{n}$ and $\hat{\mathbf{z}}$. α is the azimuthal angle between the projection of $\mathbf{n}$ in the $\hat{\mathbf{r}}$-$\hat{\boldsymbol{\phi}}$ plane and $\hat{\mathbf{r}}$. Radial and axial coordinates r and z are normalized by the capillary radius R, so that $r = 1$ corresponds to the capillary surface.

2.1.2 Parametrization and experimental details

We study achiral LCs with relatively small K_2 confined in cylindrical capillaries. The director is parametrized in terms of an azimuthal angle α and a polar angle β (Fig. 2.1):

$$\mathbf{n} = \cos\alpha \sin\beta\, \hat{\mathbf{r}} + \sin\alpha \sin\beta\, \hat{\boldsymbol{\phi}} + \cos\beta\, \hat{\mathbf{z}}. \tag{2.1.2}$$

Since each term in the Frank free energy integrand (Eq. 2.1.1) has the same number of derivatives, the integral can be converted to a dimensionless form by pulling out a lengthscale set by the boundary, which we take to be capillary radius R. The radial and axial coordinates r and z are thus normalized by R, so that $r = 1$ corresponds to the capillary surface. This dimensionless scaling property also means that configurations for cylinders of different radii are simply scaled versions of each other.

The total topological charge inside a liquid crystal region that contains point hedgehog defects is [28]

$$d = \frac{1}{4\pi} \int_S \mathrm{d}u\, \mathrm{d}v\, \mathbf{n} \cdot (\partial_u \mathbf{n} \times \partial_v \mathbf{n}), \tag{2.1.3}$$

where S is the 2D surface bounding the region and parametrized by the coordinates u and v. Taking the surface to be the boundary of a capillary domain $0 \leq r \leq 1$, $-Z \leq z \leq Z$, and $0 \leq \phi < 2\pi$, we calculate

$$d = \frac{\cos\beta(0,Z) - \cos\beta(0,-Z)}{2} \tag{2.1.4}$$

for any ϕ-independent configuration that satisfies either homeotropic or degenerate planar anchoring. Liquid crystal topological charges are only consistent up to an overall sign; note that Eq. (2.1.3) is odd in $\mathbf{n}$ whereas director configurations are invariant under $\mathbf{n} \to -\mathbf{n}$.

The theoretical work reported in this chapter is complemented by experiments employing Sunset Yellow FCF (SSY), a lyotropic chromonic LC with a small twist modulus compared to its splay and bend moduli (Table 2.1) [22, 25]. Lyotropic chromonic LCs are composed of columnar aggregates of organic, plank-like molecules dissolved in water and are thus biocompatible [29, 30]. To achieve homeotropic anchoring, glass capillary surfaces are conformally coated with a polymer that induces homeotropic alignment of the aggregates via noncovalent interactions [31]. No treatment of glass capillary surfaces is necessary to achieve degenerate planar anchoring [32].

2.2 Homeotropic anchoring

2.2.1 Achiral configurations and defects with equal Frank moduli

For comparison, we first consider the case of a common, well-established nematic LC like 4-cyano-4'-pentylbiphenyl (5CB) whose bulk elastic moduli can be approximated as being equal (Table 2.1), so $K \equiv K_1 = K_2 = K_3$. Since the saddle-splay term can be integrated to the boundary, and $\mathbf{n}$ is fixed to be homeotropic at the boundary, K_{24} plays no role in this system. Indeed, if $\mathbf{n} = \hat{\boldsymbol{\nu}}$, the outward-pointing unit normal,

$$F_{24} = -\frac{K_{24}}{2}\int \mathrm{d}^3\mathbf{x}\,\boldsymbol{\nabla}\cdot(\mathbf{n}\times\boldsymbol{\nabla}\times\mathbf{n} + \mathbf{n}\boldsymbol{\nabla}\cdot\mathbf{n}) = -\frac{K_{24}}{2}\int \mathrm{d}^2S\,\boldsymbol{\nabla}\cdot\hat{\boldsymbol{\nu}} = \frac{K_{24}}{2}\int \mathrm{d}^2S\,L_{ii},$$

where $\mathbf{L}$ is the surface curvature tensor, or second fundamental form, whose eigenvalues are the principal curvatures of the surface [28]. Thus, for homeotropic anchoring, F_{24} is proportional to the integrated mean curvature of the confining surface and can thus be neglected.

To find ground state configurations, we assume that $\mathbf{n}$ only depends on r. The Frank free energy Eq. 2.1.1 simplifies to

$$\frac{F}{\pi LK} = \int_0^1 \mathrm{d}r \left[r(\partial_r \beta)^2 + r \sin^2\beta (\partial_r \alpha)^2 + \sin 2\beta \, \partial_r \beta + \frac{\sin^2 \beta}{r} \right],$$

where L is the length of the capillary. Note that the capillary dimensions do not appear in this dimensionless integral, as discussed in Sec. 2.1.2. Strong homeotropic anchoring imposes the boundary conditions $\alpha(1) = 0$ and $\beta(1) = \pi/2$. Cylindrical symmetry requires $\beta(0) = 0$ or π. $\alpha(0)$ is free, and the natural boundary conditions at $r = 0$ are trivially satisfied (see Appendix A); however, the Euler-Lagrange equations in the $r \to 0$ limit require $\partial_r \alpha(0) = 0$. Solving the Euler-Lagrange equations with these four boundary conditions yields the two escaped-radial configurations

$$\alpha(r) = 0, \tag{2.2.1}$$

$$\beta_{\mathrm{W}}(r) = 2 \arctan r, \quad \beta_{\mathrm{E}}(r) = \pi - 2 \arctan r, \tag{2.2.2}$$

corresponding to escape towards $z \to -\infty$ (west) or towards $z \to \infty$ (east), respectively [23]. For capillaries with infinite anchoring strength, these configurations have lower energy than other configurations containing disclination lines [23]. Since $\alpha = 0$, they are achiral, and since 180°-rotations transform one to the other, they have equal energy. Director schematics and plots of Eq. 2.2.2 are provided in Fig. 2.2.

Now we consider defects between regions of opposite escape directions [33–35]. We allow $\mathbf{n}$ to depend on both r and z, and calculate the Euler-Lagrange equations for $\alpha(r, z)$ and $\beta(r, z)$. To solve them numerically, we use a relaxational method described in Appendix A. In addition to the previously-discussed boundary conditions at the cylinder wall and axis,

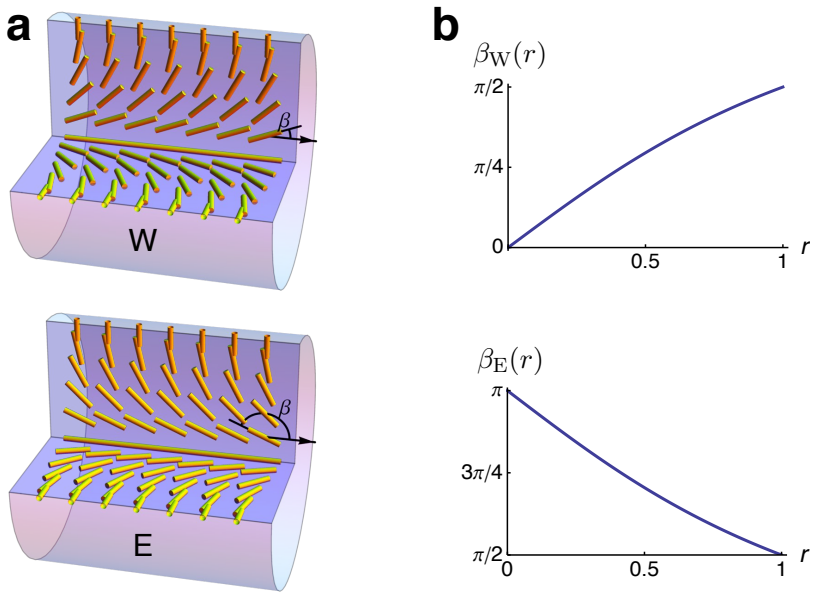

Figure 2.2: Achiral escaped-radial configurations. There are degenerate west (W) and east (E) escape directions, corresponding to escape towards $z \to -\infty$ and $z \to \infty$, respectively. (a) Director schematics and (b) plots of Eq. 2.2.2.

which are $\alpha(1, z) = 0$, $\beta(0, z) = 0$ or π, and $\beta(1, z) = \pi/2$, we impose opposite escape directions at the ends of the cylinder where $z = \pm Z$. For example, we can set $\beta(r, -Z) = \beta_{\rm W}(r)$ and $\beta(r, Z) = \beta_{\rm E}(r)$ to obtain a hyperbolic hedgehog, shown in the top rows of Figs. 2.3a and b. On the other hand, setting $\beta(r, -Z) = \beta_{\rm E}(r)$ and $\beta(r, Z) = \beta_{\rm W}(r)$ gives a radial hedgehog, shown in the bottom rows of Figs. 2.3a and b. Notice that $\beta(0, 0)$ is not well-defined for either hedgehog in Fig 2.3b, so the nematic phase is locally melted at that point. In both cases, $\alpha(r, \pm Z) = 0$ is imposed at the cylinder ends and leads to no chirality in the bulk. These two types of hedgehogs have opposite topological charges of ± 1 according to Eq. 2.1.4.

2.2.2 Chiral ground state configurations

Now we consider the case where K_2 is significantly less than $K \equiv K_1 = K_3$. The boundary conditions are the same as in the previous subsection:

$$\partial_r \alpha(0) = 0, \quad \alpha(1) = 0, \quad \beta(0) = 0 \text{ or } \pi, \quad \beta(1) = \pi/2.$$

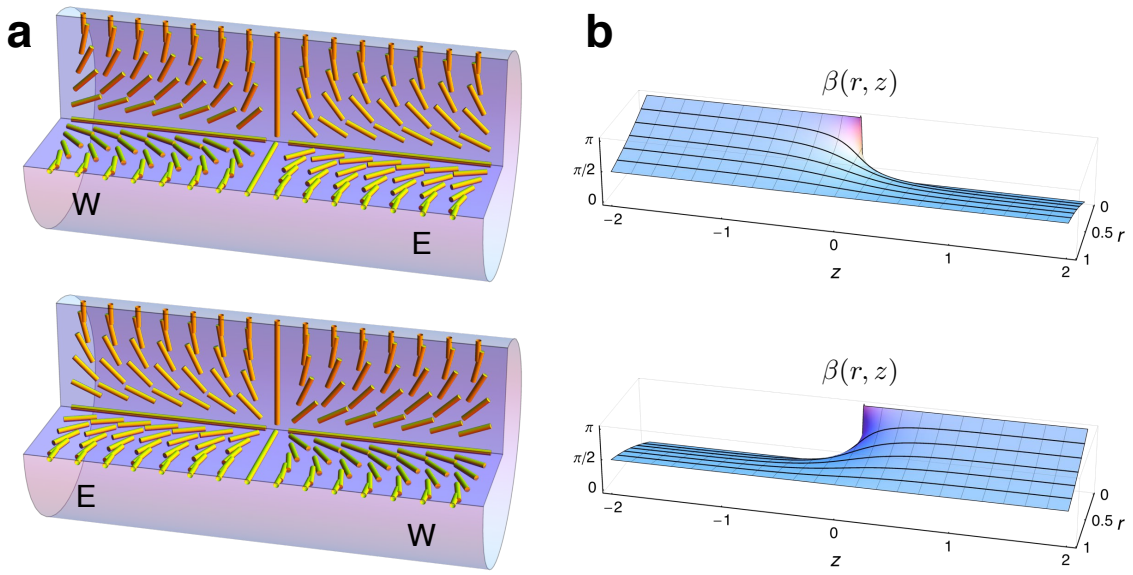

Figure 2.3: Hedgehogs between escaped-radial configurations of opposite escape directions. (a) Director schematics and (b) plots of $\beta(r,z)$. Both (a) and (b) show a hyperbolic hedgehog (top) with a west domain followed by an east domain and a radial hedgehog (bottom) with an east domain followed by a west domain. In all cases, $\alpha = 0$.

Solving the Euler-Lagrange equations leads to the achiral escaped-radial configuration of Eqs. 2.2.1 and 2.2.2 if $K_2 > K_2^c \approx 0.2694K$. As K_2 decreases below K_2^c, new configurations with $\alpha \neq 0$ grow continuously from the escaped-radial configuration via a second-order transition (Figs. 2.4a and b). These configurations have opposite signs of α, corresponding to opposite handednesses obtained via spontaneous chiral symmetry breaking, and have a lower energy than the escaped-radial configuration 2.4c. We call them the twisted- and escaped-radial (TER) configurations.

Let's look at the TER configuration in more detail for $K_2 = 0.1K$, which approximates the elastic moduli of SSY (Table 2.1). As shown in Fig. 2.5, there are 4 possible configurations due to two degenerate options for both twist and escape. The escape direction depends on whether $\beta(0) = 0$ or π, as was the case for the escaped-radial configuration, and is designated by west (W) or east (E) for escape towards $z \to -\infty$ and $z \to \infty$, respectively. Twist handedness is controlled by the sign of $\alpha(r)$, which is either positive (+) or negative (−). Instead of using this sign directly, we designate handedness by the helical handedness

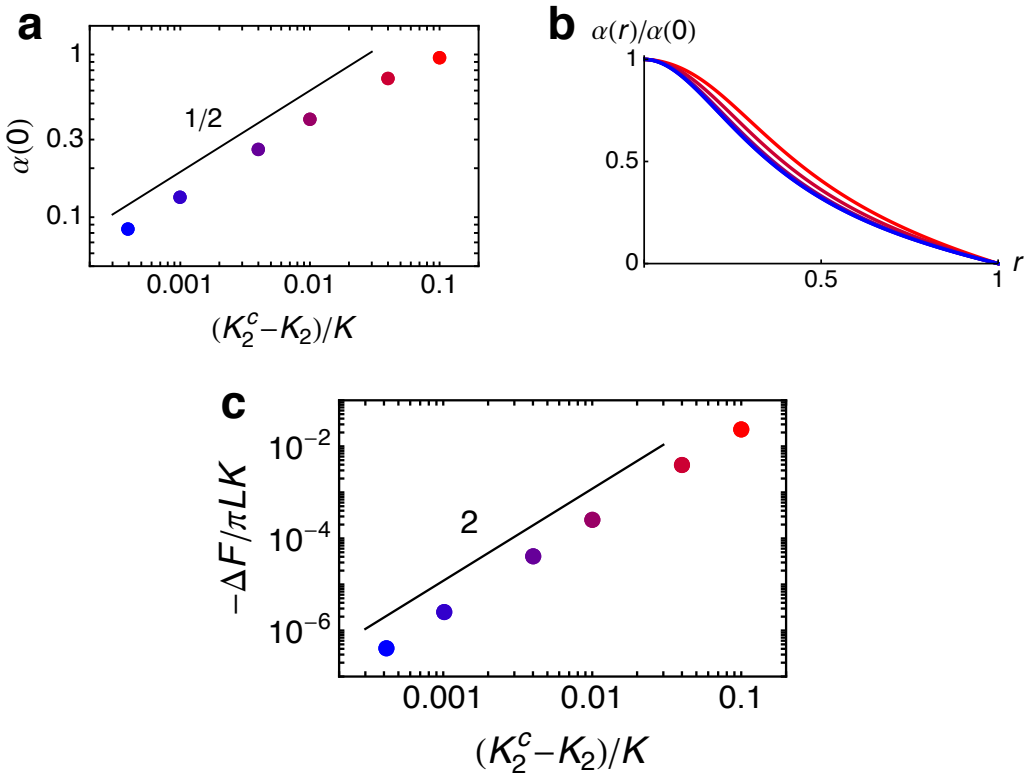

Figure 2.4: Transition from the achiral escaped-radial configuration to the chiral twisted- and escaped-radial (TER) configuration when K_2 decreases past its critical value $K_2^c \approx 0.2694K$, where $K \equiv K_1 = K_3$. This transition is second-order and spontaneously breaks chiral symmetry. Each color represents numerical calculations performed for a particular value of K_2/K. (a) The azimuthal twist angle along the capillary axis $\alpha(0)$ grows from 0 with critical exponent 1/2 (black line). Positive $\alpha(0)$'s represent TER configurations with one handedness; $\alpha(0) \to -\alpha(0)$ produces the degenerate configurations with the opposite handedness. (b) The profile of the azimuthal twist angle $\alpha(r)$ for various K_2/K, with colored lines corresponding to points of the same color in (a). (c) The relative free energy ΔF between the TER configuration and the escaped-radial configuration of Eqs. 2.2.1 and 2.2.2. L is the length of the capillary. Since ΔF is negative, the TER configuration has lower energy. Its magnitude grows from 0 with critical exponent 2 (black line).

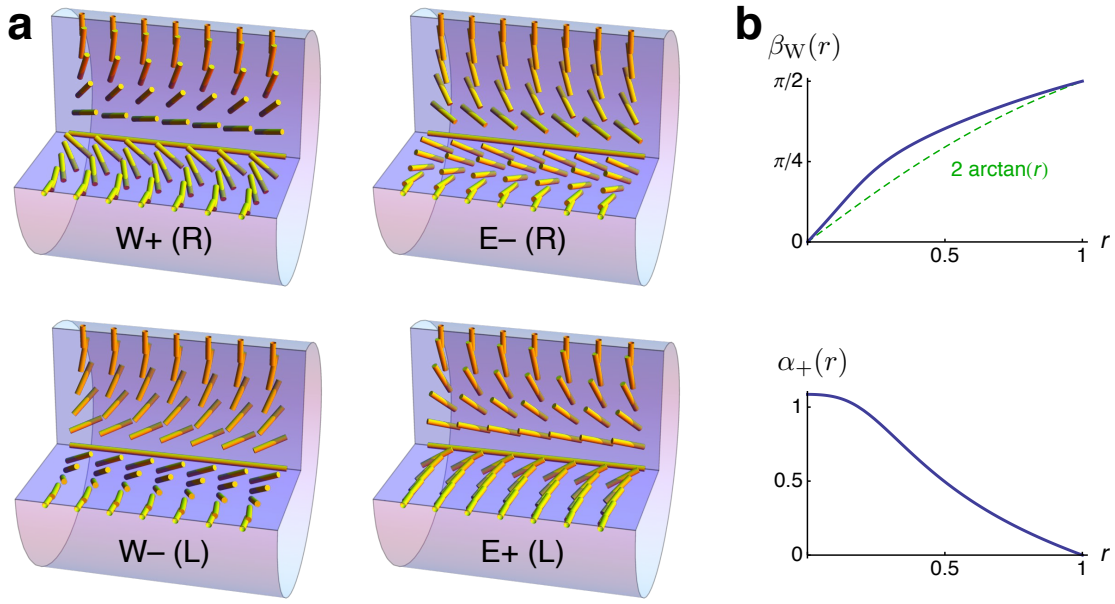

Figure 2.5: Chiral twisted- and escaped-radial configurations. There are four configurations corresponding to two degenerate options for both twist and escape. The escape directions are either west (W) or east (E) depending on β, and the twist handednesses are either positive (+) or negative (−) depending on α. Instead of + and −, we use left (L) and right (R) to designate handedness based on the helical handedness of the streamlines formed by the director field. (a) Director schematics. (b) Plots of $\beta_W(r)$ and $\alpha_+(r)$. Notice that $\beta_W(r)$ deviates significantly from its escaped-radial value $2 \arctan r$. Not shown are $\beta_E(r) = \pi - \beta_W(r)$ and $\alpha_-(r) = -\alpha_+(r)$.

of the streamlines formed by the director field, which is either right (R) or left (L). As shown in Fig. 2.5a, the WR and ER configurations are 180°-rotations of each other, as are the WL and EL configurations. The free energy is invariant under $\beta \to \pi - \beta$, which reverses the escape direction everywhere, and under $\alpha \to -\alpha$, which reverses the twist handedness everywhere.

To confirm our theory, we can compare polarized optical microscopy (POM) textures of SSY obtained experimentally under crossed-polarizers with those simulated numerically using our director solutions and Jones matrix calculations. Methods for POM imaging and Jones matrix calculations are found in Ref. [22]. Moreover, we make these POM comparisons for a range of capillary radii R, SSY weight fractions in water ϕ, and temperatures T. As reported by Ref. [26], the bulk elastic moduli vary with ϕ and T, and we input their values into Euler-Lagrange equations derived from the three-constant Frank free energy. The

experimental and theoretical POM images show respectable agreement for various polarizer orientations, without and with a waveplate that distinguishes between the four degenerate TER configurations (Fig. 2.6).

The TER configuration has never been observed before. Williams and Bouligand observed a similar structure in a nematic LC confined to a capillary, but their system included a chiral dopant that favored one handedness over another [36]. Our structure, on the other hand, arises from achiral LCs that undergo spontaneous chiral symmetry breaking.

2.2.3 Chiral defects

Domain walls and defects arise between domains of opposite twist handedness and/or escape direction, and we can calculate them by allowing the director $\mathbf{n}$ to depend on both r and z, where z ranges from $-Z$ to Z. We apply our relaxational method to solve the Euler-Lagrange equations of the Frank free energy for $\alpha(r,z)$ and $\beta(r,z)$ (Appendix A). For all domain walls and defects, homeotropic boundary conditions again require $\alpha(1,z)=0$ and $\beta(1,z)=\pi/2$; the TER configuration requires $\beta(0,z)=0$ or π; and the $r\to 0$ limit of the Euler-Lagrange equations enforces $\partial_r\alpha(0,z)=0$. The identity of the domain wall or defect will depend on the boundary conditions at $z=\pm Z$. In all cases, $\beta\to\pi-\beta$ changes the escape direction everywhere and $\alpha\to-\alpha$ changes the twist direction everywhere.

We first consider two domains of opposite twist handedness and same escape direction, so $\alpha(r,\pm Z)=\alpha_{\pm}(r)$ and $\beta(r,\pm Z)=\beta_{\mathrm{W}}(r)$, for example. The total topological charge (Eq. 2.1.4) in the region they span is 0, so topological defects are not required, and they form a smooth domain wall through which the director untwists from one handedness and retwists to the other (Fig. 2.7). Note that there is no symmetry about the mid-plane of the defect, since the escape direction breaks east/west symmetry.

We next consider two domains of opposite twist handedness and opposite escape direction, so $\alpha(r,\pm Z)=\alpha_{+}(r)$, for example. $\beta(r,-Z)=\beta_{\mathrm{W}}(r)$ and $\beta(r,Z)=\beta_{\mathrm{E}}(r)$ leads to a heterochiral hyperbolic hedgehog, and $\beta(r,-Z)=\beta_{\mathrm{E}}(r)$ and $\beta(r,Z)=\beta_{\mathrm{W}}(r)$ leads to a heterochiral radial hedgehog (Fig. 2.8). These two defects have opposite topological charge.

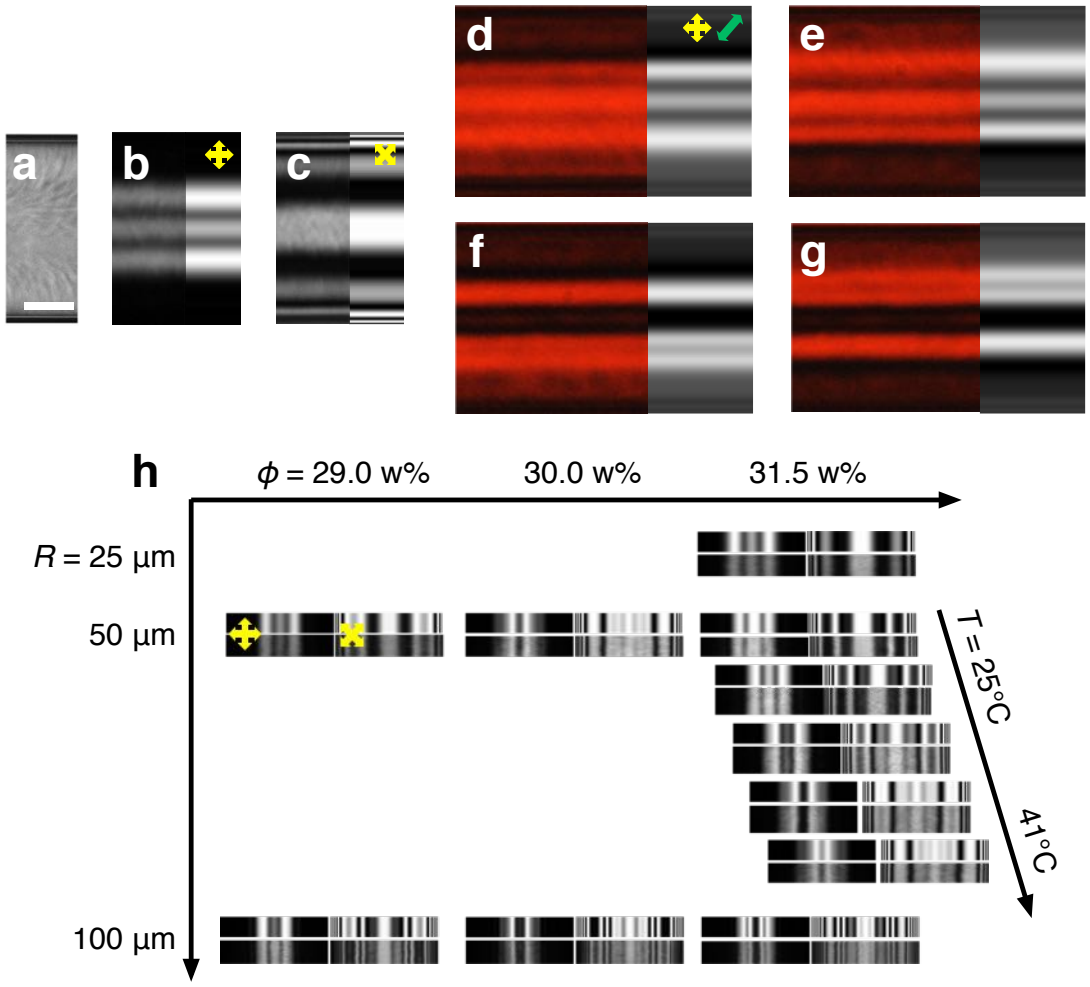

Figure 2.6: Comparison between experimentally-observed and theoretically-simulated polarized optical microscopy (POM) textures of TER configurations. Yellow arrows indicate pass axes of the polarizer and analyzer, and the green arrow indicates the slow axis of a waveplate. (a) Brightfield microscopy image. Anisotropy in the director fluctuations indicates escape to the west. Scale bar, 25 µm. (b)–(g) Experimentally-observed (left) and theoretically-simulated (right) POM textures of 31.5 w% SSY at 25 °C in a cylinder of radius 25 µm. (b) and (c) POM textures without waveplate. (d)–(g) POM textures with waveplate to differentiate twist handedness and escape direction. These textures correspond to the (d) WR, (e) ER, (f) WL, and (g) EL configurations. (h) Theoretically-simulated (top) and experimentally observed (bottom) POM textures for various capillary radii R, SSY weight fractions in water ϕ, and temperatures T. Elastic moduli used in calculations come from Ref. [26]. Experimental data and methods are reported in Ref. [22].

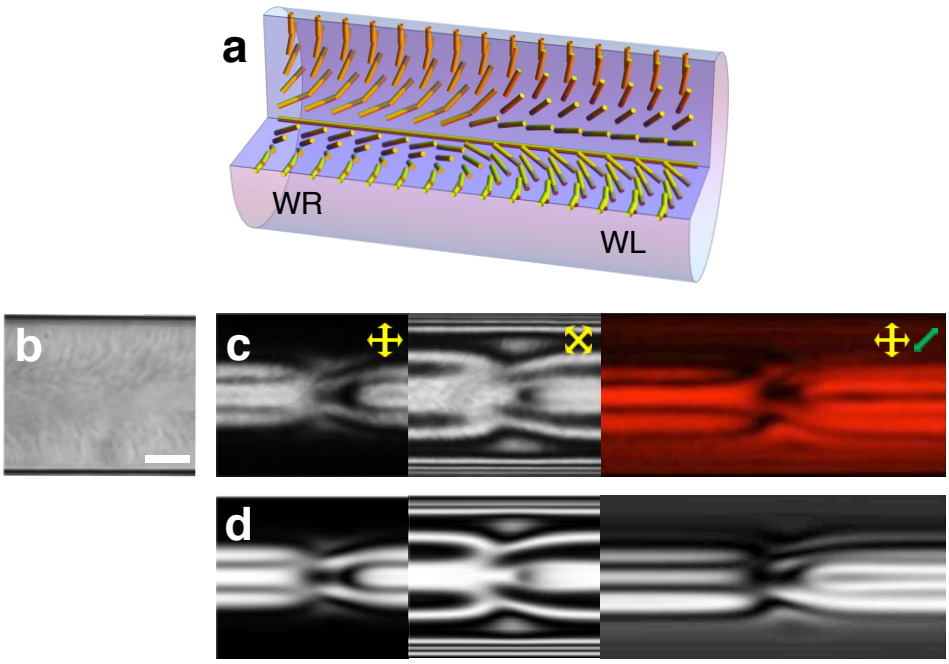

Figure 2.7: Structure of a domain wall, which separates domains of opposite twist handedness and same escape direction. (a) Nematic director schematic. (b) Brightfield microscopy image. Anisotropy in the director fluctuations indicates escape to the west. Scale bar, 25 µm. (c) and (d) Comparison between (c) experimentally-observed and (d) theoretically-simulated polarized optical microscopy (POM) textures of a domain wall. Yellow arrows indicate pass axes of the polarizer and analyzer, and the green arrow indicates the slow axis of a waveplate. Experimental data and methods are reported in Ref. [22].

We finally consider two domains of same twist handedness and opposite escape direction, so $\alpha(r, \pm Z) = \alpha_{\pm}(r)$, for example. $\beta(r, -Z) = \beta_{\mathrm{W}}(r)$ and $\beta(r, Z) = \beta_{\mathrm{E}}(r)$ leads to a homochiral hyperbolic hedgehog, and $\beta(r, -Z) = \beta_{\mathrm{E}}(r)$ and $\beta(r, Z) = \beta_{\mathrm{W}}(r)$ leads to a homochiral radial hedgehog (Fig. 2.9), and these two defects have opposite topological charge.

Surprisingly, homochiral hedgehogs have never been experimentally observed. To investigate this matter, we calculate the energies of the domain wall and each defect. As shown in Fig. 2.10a, heterochiral hedgehogs have lower energy than their homochiral counterparts, even with the small energy of a domain wall added. (Note that although hyperbolic defects have lower energy than the ground state TER configurations, the combination of a hyperbolic and a radial defect, which must alternate along the capillary, does not, so hedgehogs will not spontaneously arise from the ground state.) Moreover, the combination of a domain wall and a heterochiral defect spans domains of same twist handedness and opposite escape direction, just as a homochiral defect does (Figs. 2.10b and c). Thus, although they seem by our relaxational method to occupy local free energy minima, homochiral hedgehogs are energetically disfavored and can be replaced by their heterochiral counterparts plus a domain wall. Slow-cooling experiments around the isotropic-nematic transition temperature have confirmed this process [22]. Indeed, when domains of same twist handedness and opposite escape direction expand into the same isotropic region and meet, they form the two energetically-preferred defects with an extra TER domain in between (Figs. 2.10d and e).

2.3 Degenerate planar anchoring

2.3.1 Saddle-splay elasticity

The bulk nematic LC deformation modes, splay, twist and bend, are well known and have elastic moduli K_1, K_2 and K_3, respectively. They are easy to visualize and to independently

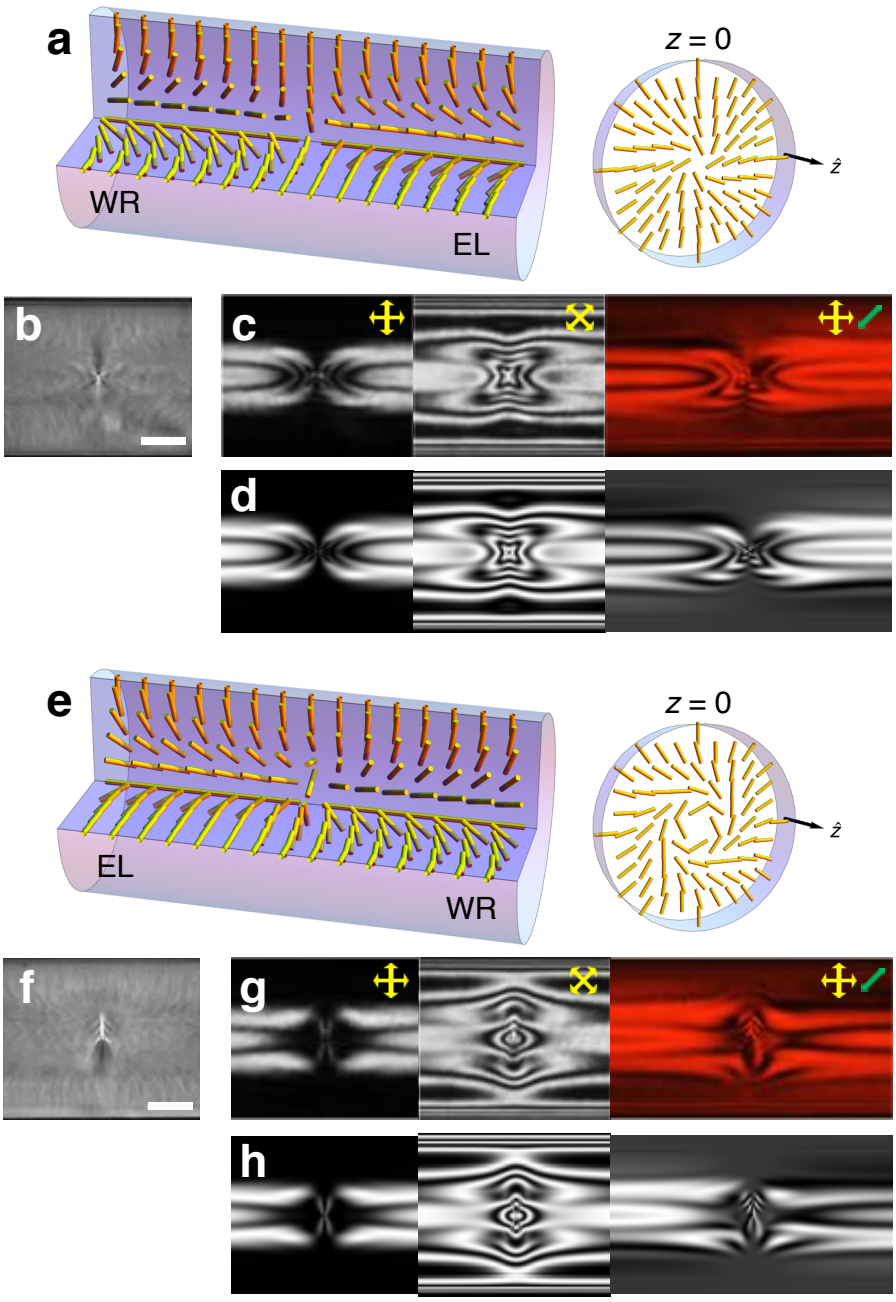

Figure 2.8: Structure of heterochiral hedgehogs, which separate domains of opposite twist handedness and opposite escape direction. (a)–(d) Heterochiral hyperbolic hedgehog. (a) Nematic director schematic, including an isolated view of the defect mid-plane at $z = 0$. (b) Brightfield microscopy image. Singular feature and anisotropy in the director fluctuations indicate a hyperbolic hedgehog. Scale bar, 25 µm. (c) and (d) Comparison between (c) experimentally-observed and (d) theoretically-simulated polarized optical microscopy (POM) textures. Yellow arrows indicate pass axes of the polarizer and analyzer, and the green arrow indicates the slow axis of a waveplate. (e)–(h) Corresponding information for a heterochiral radial hedgehog. Experimental data and methods are reported in Ref. [22].

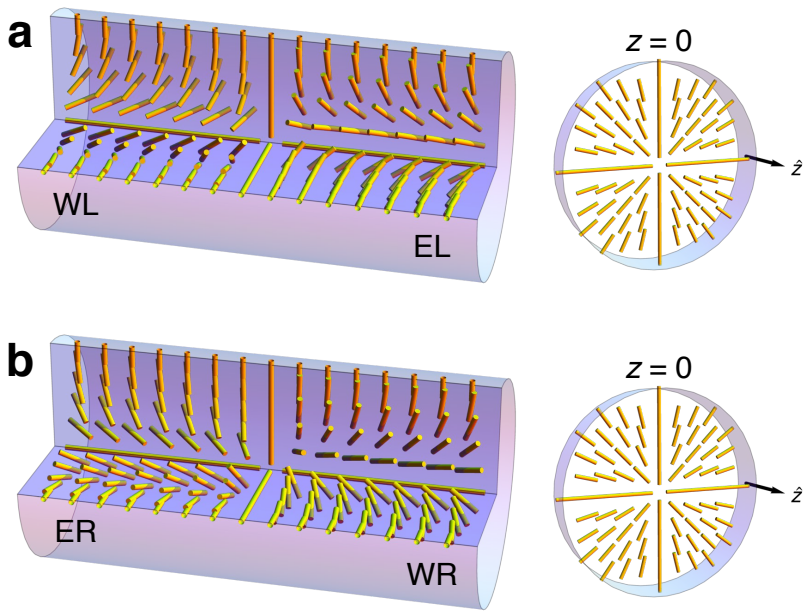

Figure 2.9: Structure of homochiral hedgehogs, which presumably separate domains of same twist handedness and opposite escape direction. (a) Homoochiral hyperbolic hedgehog. Nematic director schematic, including an isolated view of the defect mid-plane at $z = 0$. (b) Corresponding information for a heterochiral radial hedgehog. These defects have never been observed.

excite via clever usage of sample geometry [37–39], LC boundary conditions [40, 41], and external fields [26, 42]. As a result, these moduli have been measured for a variety of thermotropic and lyotropic LCs [26, 27, 39, 43–45]. By contrast, a much less studied fourth independent mode [46–48] of elastic deformation in nematic LCs can exist; it is called saddle-splay. Saddle-splay is hard to visualize and to independently excite [48]. Moreover, the energy of this deformation class can be integrated to the boundary, so that the mode does not appear in the Euler-Lagrange equations. With fixed boundary conditions, such as strong homeotropic anchoring discussed in the previous section, the saddle-splay energy will have no effect on the LC director configuration. Even with free boundary conditions, the saddle-splay energy will not affect the bulk LC configuration unless the principal curvatures of the surface are different, i.e., saddle-splay effects are not expected for spherical or flat surfaces. Thus, although much progress in understanding saddle-splay has been made [7, 28], especially with thermotropic nematic LCs, unambiguous determination of saddle-splay

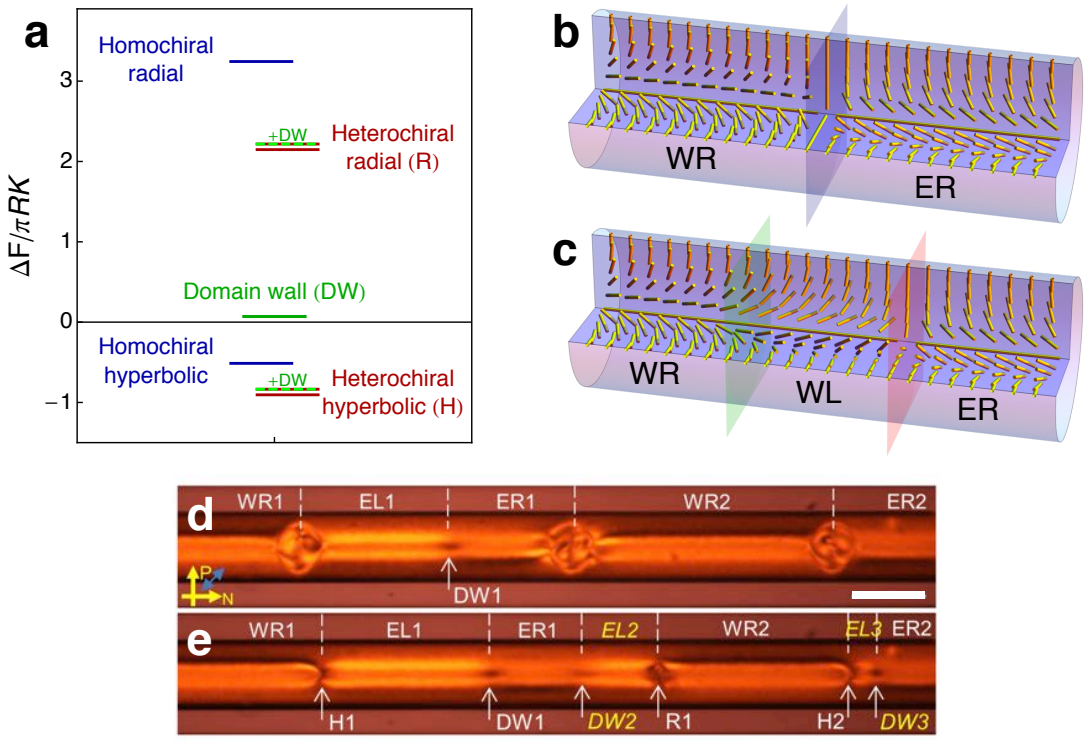

Figure 2.10: Energetic selection against homochiral hedgehogs. (a) Free energy differences ΔF between defects and the ground state TER configurations. The green-and-red dashed lines indicate the combination of a domain wall and a heterochiral hedgehog. (b) A homochiral hyperbolic hedgehog (blue) separating WR and ER domains. (c) A combination of a domain wall (green) and a heterochiral hyperbolic hedgehog (red) separating WR and ER domains with a WL domain in between. (d) and (e) Slow-cooling experiment from the isotropic phase into the nematic phase performed in 31.5 w% SSY. TER domains are labeled above the capillary and domain walls (DW), heterochiral hyperbolic hedgehogs (H), and heterochiral radial hedgehogs (R) are labeled below the capillary with sequential indices. Yellow arrows indicate pass axes of the polarizer (P) and analyzer (N), and the blue arrow indicates the slow axis of a waveplate. (d) The capillary at 40 °C. Convex isotropic regions separate domains of opposite escaping direction. Scale bar, 100 µm. (e) The same capillary cooled to 38 °C. Note that domains of same twist handedness and opposite escape direction that expanded into the same isotropic regions (ER1 and WR2, for example) have formed heterochiral hedgehogs (R1, for example) instead of homochiral ones. In the process of doing so, they have created domain walls and new TER domains (yellow). Experimental data and methods are reported in Ref. [22].

energy effects on liquid crystal configurations and measurement of the saddle-splay elastic modulus, K_{24}, remain difficult [49].

While the bulk elastic constants described above strongly influence LC director configurations, LC boundary conditions at material interfaces also influence bulk structure. Indeed, considerable effort has gone into development of surface preparation techniques to produce particular bulk director configurations [32, 40, 50–54]. The saddle-splay term integrates to the boundary and, for degenerate planar anchoring, effectively imposes boundary conditions at free surfaces favoring director alignment along the direction of smallest or most negative surface curvature for positive K_{24} and outwardly pointing surface normals [24]. Indeed, using both $\hat{\boldsymbol{\nu}} \cdot \mathbf{n} = 0$ and $\partial_j(\nu_i n_i) = 0$, where again $\hat{\boldsymbol{\nu}}$ is the outwardly-pointing surface normal, we obtain

$$\begin{aligned} F_{24} &= -\frac{K_{24}}{2} \int \mathrm{d}^3\mathbf{x}\, \boldsymbol{\nabla} \cdot (\mathbf{n} \times \boldsymbol{\nabla} \times \mathbf{n} + \mathbf{n}\boldsymbol{\nabla} \cdot \mathbf{n}) \\ &= \frac{K_{24}}{2} \int \mathrm{d}^3\mathbf{x}\, \boldsymbol{\nabla} \cdot [(\mathbf{n} \cdot \boldsymbol{\nabla})\mathbf{n} - \mathbf{n}\boldsymbol{\nabla} \cdot \mathbf{n}] \\ &= \frac{K_{24}}{2} \int \mathrm{d}^2 S\, \hat{\boldsymbol{\nu}} \cdot (\mathbf{n} \cdot \boldsymbol{\nabla})\mathbf{n} \\ &= \frac{K_{24}}{2} \int \mathrm{d}^2 S\, \nu_i n_j \partial_j n_i \\ &= -\frac{K_{24}}{2} \int \mathrm{d}^2 S\, n_i n_j \partial_j \nu_i \\ &= \frac{K_{24}}{2} \int \mathrm{d}^2 S\, n_i n_j L_{ij} \end{aligned} \tag{2.3.1}$$

i and j are coordinate indices in 3D space, $\mathrm{d}^2 S$ is the magnitude of the surface area element, and $L_{ij} = -\partial_i \nu_j$ is the surface curvature tensor, or second fundamental form, in the 3D basis. Perhaps a more common form for $\mathbf{L}$, as described in Ref. [55], uses a local 2D basis of surface tangent unit vectors $\hat{\mathbf{e}}_1$ and $\hat{\mathbf{e}}_2$: $L_{ab} = e_{ai} e_{bj} L_{ij}$, where a and b indicate the basis vector index 1 or 2. If we choose $\hat{\mathbf{e}}_1$ and $\hat{\mathbf{e}}_2$ to be the eigenvectors of L_{ab} with eigenvalues κ_1 and κ_2, which are the principal curvatures, then Eq. 2.3.1 becomes [24]

$$F_{24} = \frac{K_{24}}{2} \int \mathrm{d}^2 S \left(\kappa_1 n_1^2 + \kappa_2 n_2^2\right). \tag{2.3.2}$$

$n_1 = \hat{\mathbf{e}}_1 \cdot \mathbf{n}$ and $n_2 = \hat{\mathbf{e}}_2 \cdot \mathbf{n}$ are the components of $\mathbf{n}$ along the principal directions. This form explicitly shows that $\mathbf{n}$ prefers to align along the principal direction with smallest or most negative curvature.

The potential role of saddle-splay effects in determining bulk director configurations by spontaneous symmetry breaking has been appreciated [40, 56, 57] but has been difficult to fully characterize; generally, molecular surface forces can impose preferred boundary conditions that are hard to disentangle from effects due to K_{24} [58, 59]. As a result, the measurements of K_{24} to date have wide confidence intervals [56, 60, 61] and even vary in sign [61]. Finally, additional factors that have complicated assignment of saddle-splay effects are the so-called Ericksen inequalities [62], which claim that thermodynamic stability requires $0 < K_{24} < 2K_2$ and $K_{24} < 2K_1$. These inequalities were derived assuming spatially-uniform gradients of the director. They do not, however, apply in geometries such as ours in which gradients are not uniform.

2.3.2 Chiral ground state configurations

We take $\mathbf{n}$ to depend only on r, and we wish to solve the Euler-Lagrange equations to the full four-constant Frank free energy of Eq. 2.1.1. Degenerate planar anchoring enforces the boundary condition $\alpha(1) = \pi/2$, and cylindrical symmetry requires $\beta(0) = 0$ for a defect-free configuration. Both $\alpha(0)$ and $\beta(1)$ are free to vary, but stationarity of the free energy produces the natural boundary conditions $\partial_r \alpha(0) = 0$ and $\partial_r \beta(1) = \left(\frac{K_{24}}{2K_2} - \frac{1}{2}\right) \sin 2\beta(1)$. The Euler-Lagrange equation for $\alpha(r)$ can be solved by

$$\alpha(r) = \pi/2, \tag{2.3.3}$$

which simplifies the free energy to

$$\begin{aligned}
\frac{F}{\pi L} &= \int_0^1 \mathrm{d}r\, r \left[K_2 \left(\partial_r \beta + K_3 \frac{\sin 2\beta}{2r} \right)^2 + \frac{\sin^4 \beta}{r^2} - K_{24} \sin 2\beta\, \partial_r \beta \right] \\
&= \int_0^1 \mathrm{d}r \left[K_2 r (\partial_r \beta)^2 + K_2 \frac{\sin^2 2\beta}{4r} + K_3 \frac{\sin^4 \beta}{r} \right] - (K_{24} - K_2) \sin^2 \beta_1,
\end{aligned}$$

where L is the length of the capillary.

The Euler-Lagrange equation for $\beta(r)$ is

$$2K_2 r\partial_r(r\partial_r\beta) - K_2\cos 2\beta\sin 2\beta - 4K_3\cos\beta\sin^3\beta = 0,$$

and its solution is [58]

$$\beta_{\mathrm{ET}}(r) = \arctan\frac{2\sqrt{K_2K_{24}(K_{24}-2K_2)}r}{\sqrt{K_3}[K_{24}-(K_{24}-2K_2)r^2]}. \tag{2.3.4}$$

This configuration exists for $K_{24} > 2K_2$ and has right-handed chirality, i.e., the director streamlines form right-handed helices. It is depicted in Fig 2.11a alongside its mirror image with the same energy, which can be obtained by either $\beta \to \pi - \beta$ or $\alpha \to -\alpha$. Following [58], we call them the escaped-twisted (ET) configurations. If $K_{24} < 2K_2$, then only the trivial $\beta(r) = 0$ solution exists, which corresponds to the undistorted parallel-axial configuration [23]. As K_{24} surpasses $2K_2$, which is exactly the upper bound found by Ericksen, the system spontaneously breaks chiral symmetry, and an ET configuration of one handedness grows continuously from the trivial solution with critical exponent 1/2. $\beta(1)$ tracks this process and its right-handed solution is plotted in Fig. 2.11b. The free energy of the ET configurations is

$$\frac{F}{\pi L} = -(K_{24}-2K_2) + \frac{\sqrt{K_2}K_3}{\sqrt{K_3-K_2}}\arctan\frac{\sqrt{K_3-K_2}(K_{24}-2K_2)}{\sqrt{K_2}(K_3+K_{24}-2K_2)}, \tag{2.3.5}$$

Notice that as K_{24} increases beyond $2K_2$, the free energy decreases continuously from 0 (with critical exponent 2), thereby confirming that the ET configuration as a ground state is preferred over the uniform configuration whenever it can exist. $K_{24} = 2K_2$ marks a second-order phase transition line.

Experimental investigations of this system are reported in Ref. [25] and find that SSY does indeed adopt ET configurations. Measurements of $\beta(r)$ from anisotropic flickering arising from thermal director fluctuations match well with Eq. 2.3.4 and show large values

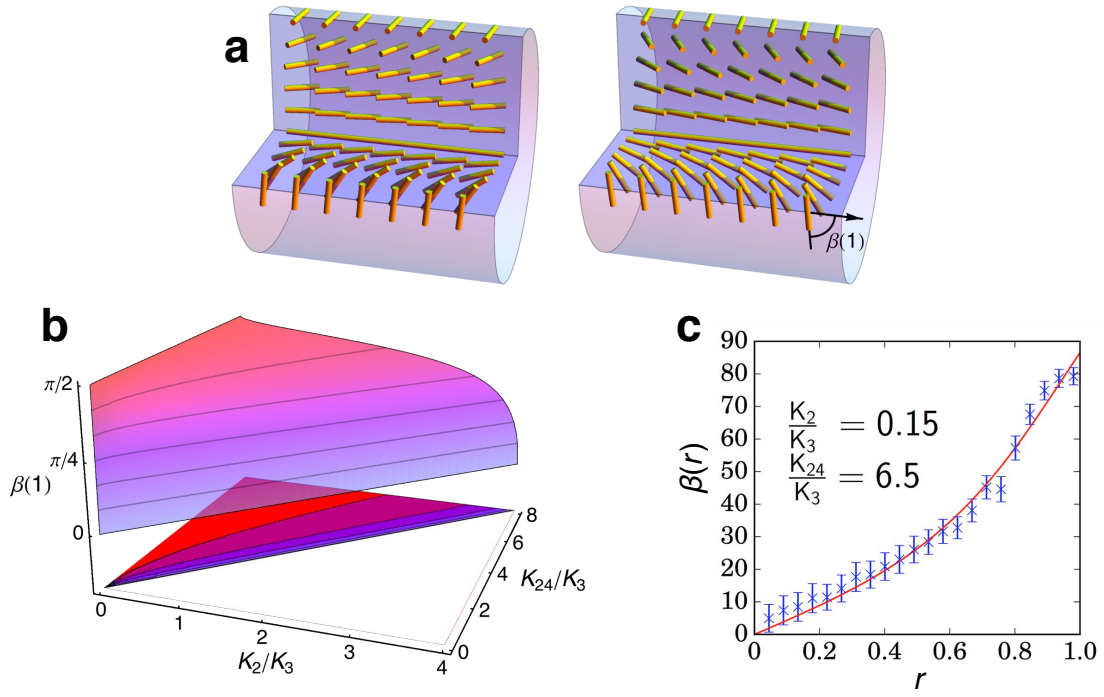

Figure 2.11: Chiral escaped-twisted (ET) configurations. (a) Director schematics of left-handed (left) and right-handed (right) ET configurations, with handedness assigned by the helical handedness of director streamlines. (b) Phase diagram of right-handed $\beta(1)$ as a function of K_2/K_3 and K_{24}/K_3. When $K_{24} < 2K_2$, the ET solution does not exist. As K_{24} is increased past $2K_2$, $\beta(r)$, as indicated by $\beta(1)$, grows continuously from the trivial $\beta(r) = 0$ solution via a second-order transition. (c) Fit of Eq. 2.3.4 (red line) to experimental measurements of $\beta(r)$ (blue points) obtained from anisotropic flickering arising from thermal director fluctuations. The values of K_2/K_3 and K_{24}/K_3 are extracted from the fit. Experimental data and methods are reported in Ref. [25].

for $\beta(1)$ and K_{24} (Fig. 2.11c). The measured values of $K_2/K_3 \approx 0.1$ agree with previously reported values for SSY (Table 2.1). The mean value of K_{24}/K_3 averaged across experiments is 6.6 with bounding interval [3.8, 9.4] and corresponds to a very large ratio $K_{24}/K_2 \sim 50$, which strongly violates the Ericksen inequality $K_{24} < 2K_2$. Moreover, the mere observation of any twist necessitates its violation. We can also theoretically confirm that the ET configuration is thermodynamically stable. We set $\alpha(r) = \alpha_0(r) + \delta\alpha(r)$ and $\beta(r) = \beta_0(r) + \delta\beta(r)$, where $\alpha_0(r)$ and $\beta_0(r)$ are set to ET values of Eqs. 2.3.3 and 2.3.4, and expand the Frank free energy to quadratic order in small deviations $\delta\alpha$ and $\delta\beta$. The free energy takes this form

$$\frac{F}{\pi L} = \frac{F_0}{\pi L} + \frac{1}{2\pi L}\int_0^R \mathrm{d}r \begin{pmatrix} \delta\alpha & \delta\beta \end{pmatrix} \begin{pmatrix} M_{\alpha\alpha} & 0 \\ 0 & M_{\beta\beta} \end{pmatrix} \begin{pmatrix} \delta\alpha \\ \delta\beta \end{pmatrix}.$$

The stability matrix operator $\mathbf{M}$ is diagonal, so $\delta\alpha$ and $\delta\beta$ are decoupled. Stability requires that $\mathbf{M}$ has only positive eigenvalues. We can solve the two eigenvalue equations

$$M_{\alpha\alpha}\delta\alpha = \lambda_\alpha\delta\alpha \quad \text{and} \quad M_{\beta\beta}\delta\beta = \lambda_\beta\delta\beta$$

subject to the boundary conditions of our system. We can do this analytically in the limit that $(K_{24} - 2K_2)/2K_2 \ll 1$ and numerically in general by variationally minimizing the Rayleigh quotient [63]. We find that when $K_{24} > 2K_2$, the λ_α's and λ_β's are all positive, so the ET configuration is thermodynamically stable even though it violates the Ericksen inequalities.

Prior work with thermotopic LCs has found this ET configuration when an external anchoring condition dominates the behavior of $\beta(1)$ at the capillary surface through a chemical or mechanical treatment of the surface [34, 58, 59]. These treatments explicitly favor the azimuthal direction with no relationship to surface curvature; thus, in our cylindrical ge-

ometry, their free energy has an extra factor of the radius R:

$$\frac{F_\phi}{\pi L} = -RW_\phi \sin^2 \beta(1)$$

where W_ϕ is the azimuthal alignment energy density. On the other hand, we have no such azimuthal surface effects in our system, since we used capillaries without chemical treatment and, via atomic force microscopy and scanning electron microscopy, found no microscropic structures on the capillary surface that could favor anisotropic alignment [25]. Instead, the ET configuration is energetically stabilized by saddle-splay free energy, which takes the R-independent form

$$\frac{F_{24}}{\pi L} = -K_{24} \sin^2 \beta(1)$$

in our system.

There is a possibility that azimuthal surface alignment could be favored by a surface anchoring energy that couples the director to the curvature tensor, which has been proposed in models of deformable membranes [64, 65] but has never been directly experimentally observed in LC systems to our knowledge. Such a symmetry-allowed anchoring energy would look like

$$F_w = \frac{w}{2} \int \mathrm{d}^2 S \, n_i n_j L_{ij}, \tag{2.3.6}$$

which is identical to Eq. 2.3.1 with K_{24} replaced by the anchoring strength w. Again, i and j are coordinate indices in 3D space, $\mathrm{d}^2 S$ is the magnitude of the surface area element, and $L_{ij} = -\partial_i \nu_j$ is the surface curvature tensor, or second fundamental form, in the 3D basis. Thus, saddle-splay energy and curvature-coupled surface anchoring energy have the same mathematical form for systems with degenerate planar boundary conditions. The only difference between these two effects is their microscopic origin. Saddle-splay energy arises solely from energetic and entropic interactions among LC molecules/mesogens themselves due to confinement into a curved geometry; it is independent of the identity of the confining container. An anchoring energy must arise from energetic interactions between LC molecules/mesogens and the confining container; presumably, changing the surface chem-

istry of the container can change the magnitude and/or sign of this energy.

2.3.3 Chiral defects

ET domains of opposite handedness must be separated by domain walls or hedgehogs, the latter of which were qualitatively proposed in Ref. [59]. We first calculate the structure of chiral hedgehogs through Euler-Lagrange relaxation (Appendix A). The boundary conditions from the previous subsection still apply here: $\partial_r\alpha(0,z) = 0$, $\alpha(1,z) = \pi/2$, $\beta(0,z) = 0$, and $\partial_r\beta(1,z) = \left(\frac{K_{24}}{2K_2} - \frac{1}{2}\right)\sin 2\beta(1,z)$. The boundary conditions at the ends of the cylinder where $z = \pm Z$ are, for example $\alpha(r,\pm Z) = \pi/2$, $\beta(r,-Z) = \pi - \beta_{\mathrm{ET}}(r)$, and $\beta(r,Z) = \beta_{\mathrm{ET}}(r)$. Note that β changes by π along the capillary axis from one side of the defect to the other, so its topological charge must be ± 1 (Eq. 2.1.4). A schematic of this chiral hedgehog, along with comparisons between experimentally-measured and theoretically-simulated POM images [25], is shown in Fig. 2.12. The chirality can be inverted everywhere by either $\beta \to \pi - \beta$ or $\alpha \to -\alpha$.

These hedgehog configurations are very similar to what one gets if one takes the achiral radial and hyperbolic hedgehogs and simply rotates all directors by $\pi/2$ about the z-axis (Fig. 2.13). This simple operation, which is guaranteed to preserve hedgehog charge, automatically produces domains of opposite chirality on opposite sides of the hedgehog defect regardless of the sign of its charge. By continuing this rotation through a full 2π rotation, each domain transforms among achiral escaped-radial configurations of both escape directions and chiral ET configurations of both handednesses, and each defect transforms among radial, hyperbolic, and both chiral hedgehogs. Note that we started with a hyperbolic and a radial defect, which have charge ± 1, and through rotation, we arrive at chiral hedgehog pairs of opposite chirality. Since topological charge is conserved throughout this transformation, chiral hedgehogs must also have charge ± 1, with opposite signs for defects of opposite chirality. Charges of successive hedgehogs necessarily alternate in sign. Note that the overall sign is not well-defined, since a hyperbolic hedgehog can be transformed into a radial one, and a right-to-left hedgehog can be transformed into a left-to-right one;

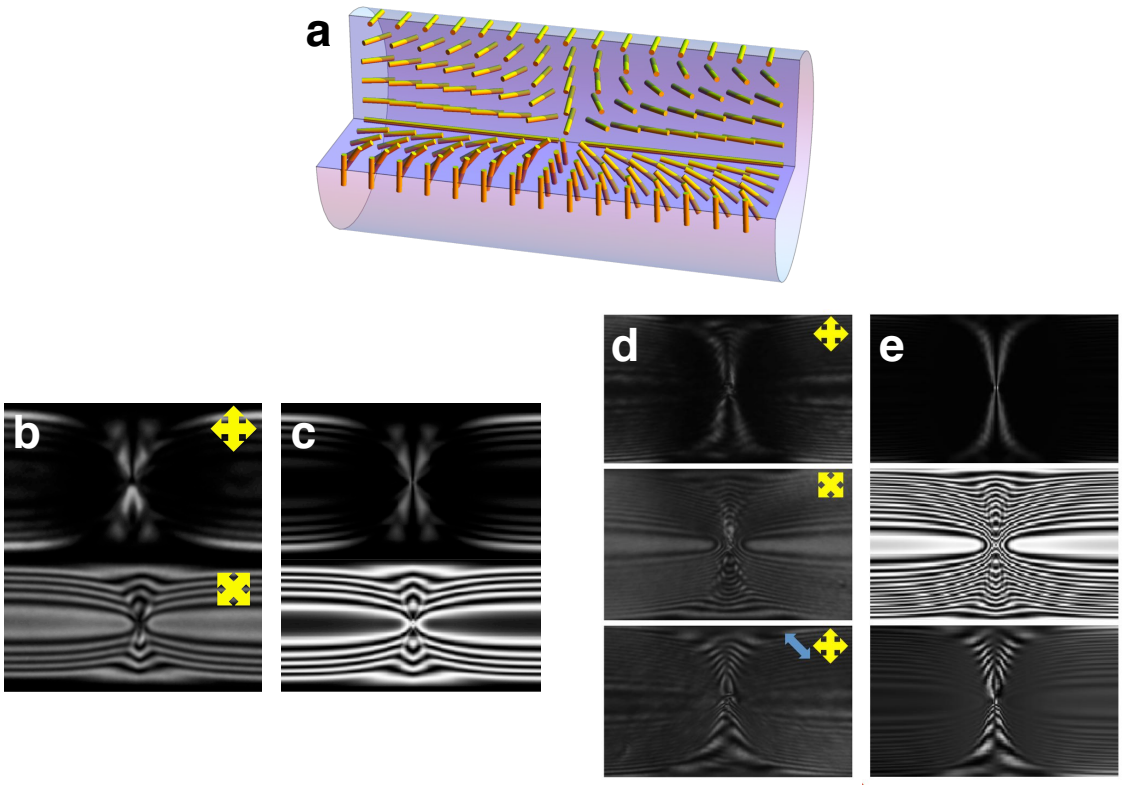

Figure 2.12: Chiral hedgehog between escaped-twisted domains of opposite handedness. (a) Director schematic. (b)–(e) Comparison between experimentally-observed and theoretically-simulated polarized optical microscopy (POM) images of 30 w% SSY at 25 °C. Theoretical configurations are calculated using $K_1 = K_3 \equiv K$, $K_2/K = 0.1$, and $K_{24}/K = 4.6$, which are consistent with measurements of the ET ground state (Fig. 2.11). Yellow arrows indicate pass axes of the polarizer and analyzer, and the blue arrow indicates the slow axis of a waveplate. (b) Experimentally-calculated and (c) theoretically-simulated POM images using a capillary of radius 25 µm. (d) Experimentally-calculated and (e) theoretically-simulated POM images using a capillary of radius 69 µm. Experimental data and methods are reported in Ref. [25].

as discussed in [28], it can be set by choosing one of the two physically equivalent directions for the director at one location.

We now calculate the structure of chiral domain walls through Euler-Lagrange relaxation. The boundary conditions at the ends of the cylinder where $z = \pm Z$ are, for example $\alpha(r, \pm Z) = \pm\pi/2$ and $\beta(r, \pm Z) = \beta_{\mathrm{ET}}(r)$. Unlike the hedgehog case in which β changes between the two ends and α remaines constant, here α changes sign while β remains constant. These boundary conditions still bring the system back to ET configurations of opposite signs, but now the topological charge is 0 (Eq. 2.1.4). Fig. 2.14 depicts this domain wall, in which the escaped-twist configuration continuously untwists from one domain to the wall mid-plane and then continuously re-twists with opposite handedness into the other domain (see Fig. 2.14a). In this case, throughout the mid-plane, the director would align along the capillary axis. However, such a domain-wall structure has never been experimentally observed in SSY [25]. Defect energetics provide an explanation for this observation. We numerically calculate the configurations of both domain walls and point defects to obtain their energies. For these calculations, we fix $K \equiv K_1 = K_3$ and $K_2/K = 0.1$ in accordance with Ref. [26] and our fluctuation experiments, and we allow K_{24} to vary. As shown in Fig. 2.14b, hedgehogs (domain walls) have lower energy than domain walls (point defects) for $K_{24}/K \gtrsim 4$ ($K_{24}/K \lesssim 4$). This result can be understood by considering the $\beta(1, z)$ of hedgehogs and domain walls, corresponding to the director at the capillary surface as depicted in Figs. 2.12a and 2.14a. For the hedgehog, the surface director can remain largely azimuthally-oriented throughout the defect region, which is favored by saddle-splay (Fig. 2.12a). For the domain wall, however, the surface director must point in the axial direction in the mid-plane of the wall (Fig. 2.14a). Thus, a large enough K_{24} would favor the hedgehog whose surface director is more consistently azimuthally aligned, even though its bulk director is very distorted near the defect core. Using $K = 6.5\,\mathrm{pN}$ from Ref. [26] and $R = 50\,\mu\mathrm{m}$, a typical dimensionless energy difference of $\Delta F/\pi RK = 0.1$ corresponds to $\Delta F = 2.5 \times 10^4 k_B T$, where $T = 298\,\mathrm{K}$ is the experimental temperature. If K_{24} is greater than the crossover value $\approx 4K$, then, according to theory, one should not expect to observe

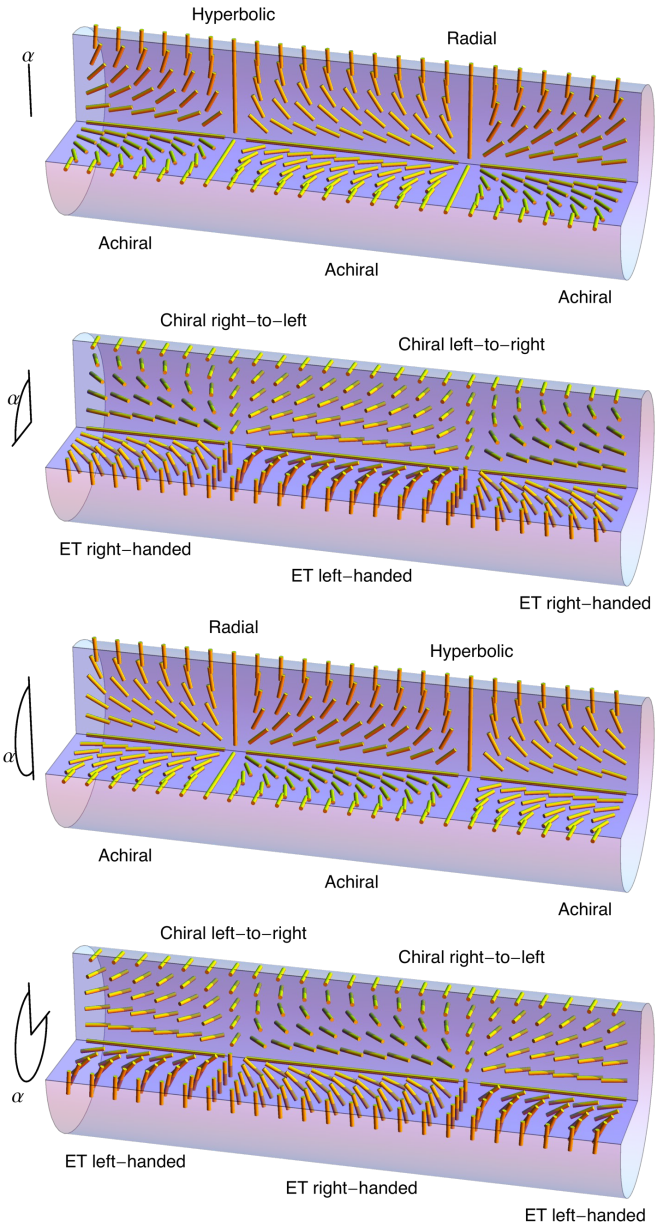

Figure 2.13: Chiral point defects as global rotations of classic achiral hedgehogs. We first plot the director configuration of two point defects corresponding to a classic radial and hyperbolic hedgehogs separating achiral domains. The azimuthal director angle is $\alpha(r, z) = 0$. We then perform a global rotation of the director field about the z-axis through 2π radians, i.e., we let $\alpha(r, z) = \alpha$ increase homogeneously from 0 to 2π. At $\alpha = \pi/2$, the radial hedgehog becomes approximately the chiral right-to-left defect and the hyperbolic hedgehog becomes approximately the chiral left-to-right defect depicted in Fig. 2.12a. They separate ET domains of alternating handedness. At $\alpha = \pi$, the original hedgehogs switch identities and the system loses all local chirality. At $\alpha = 3\pi/2$, the director configuration becomes a mirror image of the $\alpha = \pi/2$ configuration. At $\alpha = 2\pi$, the system returns to its original configuration.

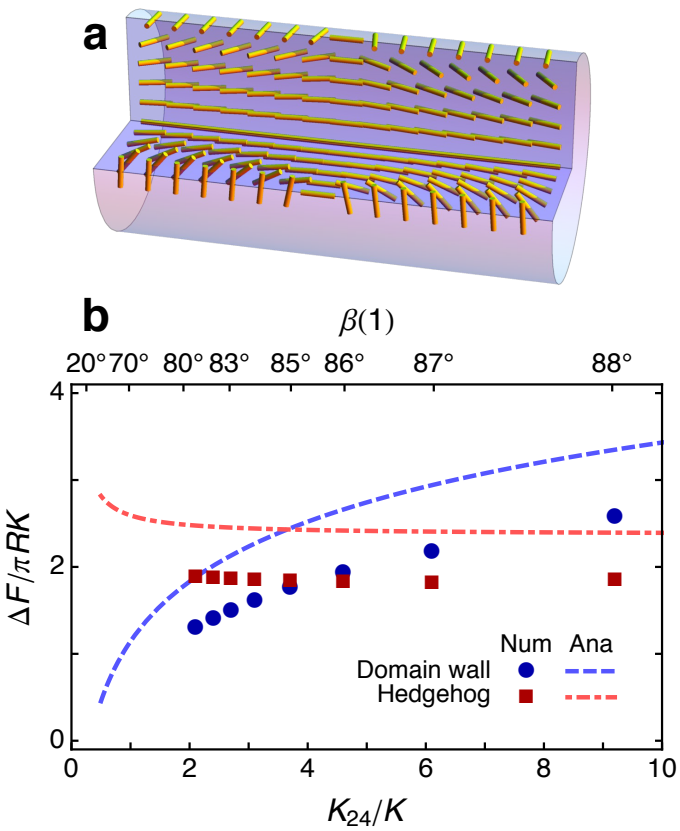

Figure 2.14: Energies of singular hedgehogs and smooth domain walls and energetic selection against domain walls for large K_{24}. (a) Director schematic of a smooth domain wall. (b) Energies of hedgehogs and domain walls relative to the ET energy as a function of either K_{24}/K or equivalently $\beta(1)$, with $K \equiv K_1 = K_3$ and $K_2/K = 0.1$. Points indicate numerical calculations and lines indicate analytical approxmations (Eqs. 2.3.11 and 2.3.9); the latter have higher energy than the former but demonstrate similar qualitative behaviors. Hedgehogs (domain walls) have lower energy than domain walls (point defects) for $K_{24}/K \gtrsim 4$ ($K_{24}/K \lesssim 4$).

smooth domain walls. Thus, the experimental abscence of domain walls sets 4 as an approximate lower bound for K_{24}/K, in agreement with the fluctuation-measured value of $K_{24}/K = 6.6$ [3.8, 9.4] [25].

We finally describe how we obtain very rough analytical expressions for the defect free energies in Fig. 2.14b. We set $K_1 = K_3 \equiv K$, define $k_2 \equiv K_2/K$ and $k_{24} \equiv K_{24}/K$, and assume that $k_2 \ll 1$ and $k_2 \ll k_{24}$. We send the cylinder ends to $\pm\infty$ We first assume that

$\alpha(r,z) = \pi/2$, a constant. The Frank free energy then only depends on β:

$$\frac{F}{\pi RK} = \int_0^1 \mathrm{d}r \int_{-\infty}^{\infty} \mathrm{d}z \left[k_2 r(\partial_r \beta)^2 + r(\partial_z \beta)^2 + k_2 \frac{\sin^2 2\beta}{4r} + \frac{\sin^4 \beta}{r} \right] - \int_{-\infty}^{\infty} \mathrm{d}z \, (k_{24} - k_2) \sin^2 \beta(1,z). \tag{2.3.7}$$

For a domain wall, we assume β is separable inside the arctangent:

$$\beta(r,z) = \arctan \left[g(z) \frac{2\sqrt{k_2 k_{24}(k_{24} - 2k_2)}r}{k_{24} - (k_{24} - 2k_2)r^2} \right].$$

This way, the natural boundary condition at $r = 1$ is always satisfied. We substitute this expression for β into the Frank free energy Eq. 2.3.7 and expand in powers of k_2. To leading order, the defect free energy relative to the ET energy becomes

$$\frac{\Delta F}{\pi RK} = \frac{\pi}{4}\sqrt{k_2} \int_{-\infty}^{\infty} \mathrm{d}z \frac{(1-g)^2 + (\partial_z g)^2}{g}.$$

We need to solve the Euler-Lagrange equation

$$0 = (1-g)^2 - (\partial_z g)^2 \tag{2.3.8}$$

with the boundary condition $g(0) = 0$. This gives

$$g(z) = \mathrm{sgn}(z) \left(1 - \mathrm{e}^{-|z|} \right),$$

where $\mathrm{sgn}(z) = z/|z|$. To get the energy, we have to substitute this $g(z)$ back into Eq. 2.3.7 to avoid a singularity at $z = 0$. Eventually, we get

$$\frac{\Delta F}{\pi RK} \approx \pi \sqrt{k_2} \log \frac{k_{24}}{\sqrt{k_2}}. \tag{2.3.9}$$

For a hedgehog, we also assume that β is separable, but the Euler-Lagrange equation Eq. 2.3.8 cannot be solved with the requisite boundary condition $g(z) \to \infty$ when $z \to 0^+$.

So we adopt another strategy and take a similar separable β:

$$\beta(r,z) = \arctan\left[\frac{1}{g(z)}\frac{2\sqrt{k_2 k_{24}(k_{24}-2k_2)}r}{k_{24}-(k_{24}-2k_2)r^2}\right].$$

We substitute this expression into the Frank free energy Eq. 2.3.7. The resulting integrand has a log-divergence at $g(z) \approx 0$ and is otherwise smooth. But it is comprised of diverging terms that precisely cancel and is thus not amenable to direct expansion. We adopt a different approach: we match the free energy density's behavior asymptotically around $g \approx 0$ and $g \approx 1$. In the latter case, we have to match leading powers of both small quantities $1-g$ and $\partial_z g$. One empirical version that works is

$$\begin{aligned}\frac{\Delta F}{\pi RK} = \int_{-\infty}^{\infty} \mathrm{d}z \Bigg\{ &- \log\left[g(2-g)\right] - \left(\frac{1}{4k_2}+\frac{1}{2k_{24}}\right)\log\left[g(2-g)\right](\partial_z g)^2 \\ &- \left(1-\frac{\pi}{4}\sqrt{k_2}\right)(1-g)^2 + \left(\frac{\pi}{4}\sqrt{k_2}+k_2\log 4k_2\right)(\partial_z g)^2 \\ &+ \left(\frac{1+\log 16k_2}{2}-\frac{\pi}{4}\sqrt{k_2}\right)(1-g)^4 \\ &- \left(\frac{5-2\log 16k_2}{16k_2}+\frac{5-2\log 16k_2}{8k_{24}}+\frac{\pi}{4}\sqrt{k_2}+k_2\log 4k_2\right)(1-g)^2(\partial_z g)^2 \Bigg\}.\end{aligned} \tag{2.3.10}$$

Inspired by the domain wall case, we make the ansatz

$$g(z) = \mathrm{sgn}(z)\left(1-\mathrm{e}^{-|z|/\xi}\right),$$

where ξ is a characteristic defect length. Substituting this back into Eq. 2.3.10 and minimizing over ξ, we get

$$\xi = \sqrt{\frac{3+2\log 16k_2}{2\pi^2-9+3\log 16k_2}\frac{3}{8k_2}}.$$

For $k_2 = 0.1$, $\xi \approx 1.1$. The minimum energy is, to leading orders in k_2,

$$\frac{\Delta F}{\pi RK} = \sqrt{\frac{(3+2\log 16k_2)(2\pi^2-9+3\log 16k_2)}{1536}}\left(\frac{3\pi}{2\pi^2-9+3\log 16k_2}+\frac{4}{\sqrt{k_2}}+\frac{4\sqrt{k_2}}{k_{24}}\right). \tag{2.3.11}$$

Note that for $k_2 \ll 1$ and $k_{24} \gtrsim 1$, the energy only weakly depends on k_{24}.

Chapter 3

Depletion-induced colloidal membranes

3.1 Introduction

3.1.1 The entropic world of colloids

Suspensions of particles with hard-core repulsive interactions form equilibrium phases that minimize the systems' free energy by maximizing their entropy. Since entropy is conventionally associated with disorder, it might be expected that hard-particle fluids form structures that lack long-range order. However, extensive experimental work and theoretical models have repeatedly demonstrated the counterintuitive notion that entropy alone is sufficient to stabilize ordered phases of ever-increasing complexity, such as 3D bulk crystals in suspensions of hard spheres [66], nematic and smectic liquid crystalline phases with hard rods [67, 68], and more exotic binary crystals and diverse microphase-separated states in mixtures of hard particles [69, 70].

Colloidal suspensions are a quintessential model system in soft condensed matter physics. They are not only interesting in their own right but also provide new insights into the structure and dynamics of diverse phases; these insights only depend on the symmetries of the constituent particles and are thus relevant on all lengthscales. For example, engineering

colloidal shapes and interactions makes it possible to mimic many processes found in atomic and molecular systems, including liquid-gas phase separation, wetting, thermal capillary waves, crystal nucleation, and the glass transition [66, 71–75]. In stark contrast to molecular systems, the size of model colloids makes it is possible to directly track the positions of all the constituent particles, thus yielding important information about universal physical processes in various condensed matter systems.

Conventional fluid membranes, assembled from permanently-linked hydrophobic and hydrophilic components, are another interesting and important soft matter system and play an essential role in biology [76]. However, due to our inability to directly visualize real-time dynamics of lipid bilayers at the nanometer scale, many membrane-based processes remain poorly understood. Recent work has demonstrated that a mixture of monodisperse micron-long filamentous bacteriophages and non-adsorbing polymers assemble into 2D one-rod-length-thick colloidal monolayer membranes [77, 78]. Intriguingly, their large-scale elastic deformations are described by the same continuum theories that are used to describe conventional lipid bilayers. Based on this observation and following the analogy between colloids and molecular substances, we hope that colloidal membranes will provide new understanding about universal membrane-mediated behaviors. There have been some recent overtures in this vein. For example, colloidal membranes permit direct visualization and quantitative characterization of liquid raft-like clusters [79], a subject that remains controversial in conventional lipid membranes [79, 80]. Eventual understanding of such complex structures requires a theoretical model that relates mesoscopic properties of colloidal membranes to the microscopic interactions of their constituent building blocks.

3.1.2 Overview of colloidal membranes

Filamentous *fd* viruses are monodisperse semi-rigid filaments with 880 nm contour length, 7 nm diameter, and 2.8 µm persistence length [81]. When suspended in an aqueous solution at increasing concentrations, they undergo a transition to an aligned nematic phase characterized by long-range orientational order. This isotropic-to-nematic phase transition is

quantitatively described by Onsager's theory, indicating that viruses repel one another via hard-core and electrostatic interactions [67, 81, 82]. Filamentous viruses are chiral and form a twisted nematic (cholesteric) phase in which the director field rotates with a well-defined handedness [83]. For wildtype *fd* virus (*fd*-wt), this twist is left-handed and the strength of cholesteric interactions is temperature-dependent and continuously increases with decreasing temperature. A single amino acid substitution in the major coat protein leads to the Y21M virus whose cholesteric phase has a handedness opposite to that of the wildtype [81]. Mixing wildtype and Y21M viruses produces cholesteric phases with intermediate twist pitches; at a certain ratio, the mixture exhibits no macroscopic twist.

The addition of a non-adsorbing polymer, such as dextran, to a dilute isotropic *fd* suspension induces virus-virus attraction via depletion [85, 86]. The geometry of the constituent rods ensures that attractive interactions are strongest for lateral associations, causing the viruses to coalesce into single-layer, disk-shaped mesoscopic clusters [77]. They slowly sediment to the bottom of the glass container, which is coated with a polyacrylamide brush penetrable to dextran in order to suppress depletion-induced virus-wall attractions [87]. Over a certain range of depletant concentrations, protrusion fluctuations induce vertical repulsion between clusters, suppressing their face-on association [78]. Consequently, such clusters continue to associate laterally, forming large equilibrium 2D colloidal membranes that can be millimeters in diameter (Fig. 3.1b). Single molecule tracking indicates liquid-like order within a membrane. Twisting of constituent chiral viruses is inherently incompatible with assembly into a layered membrane-like structure [88], so twist penetrates into the membrane from its edges and is expelled from the bulk. Unique properties of the colloidal membrane allow for direct visualization of the twist field and quantitative measurement of the twist penetration length l_{twist} [88]. When the membrane radius is much bigger than $l_{\text{twist}} \sim 1\,\mu\text{m}$, the edge adopts a surface-area-minimizing rounded shape with the constituent rods significantly tilting into the membrane plane (Fig. 3.1b); when the membrane radius becomes of the order of l_{twist} or smaller, the edge profile becomes more square-like and rods do not significantly tilt away from the membrane normal (Fig. 3.1c). Due to thermal ex-

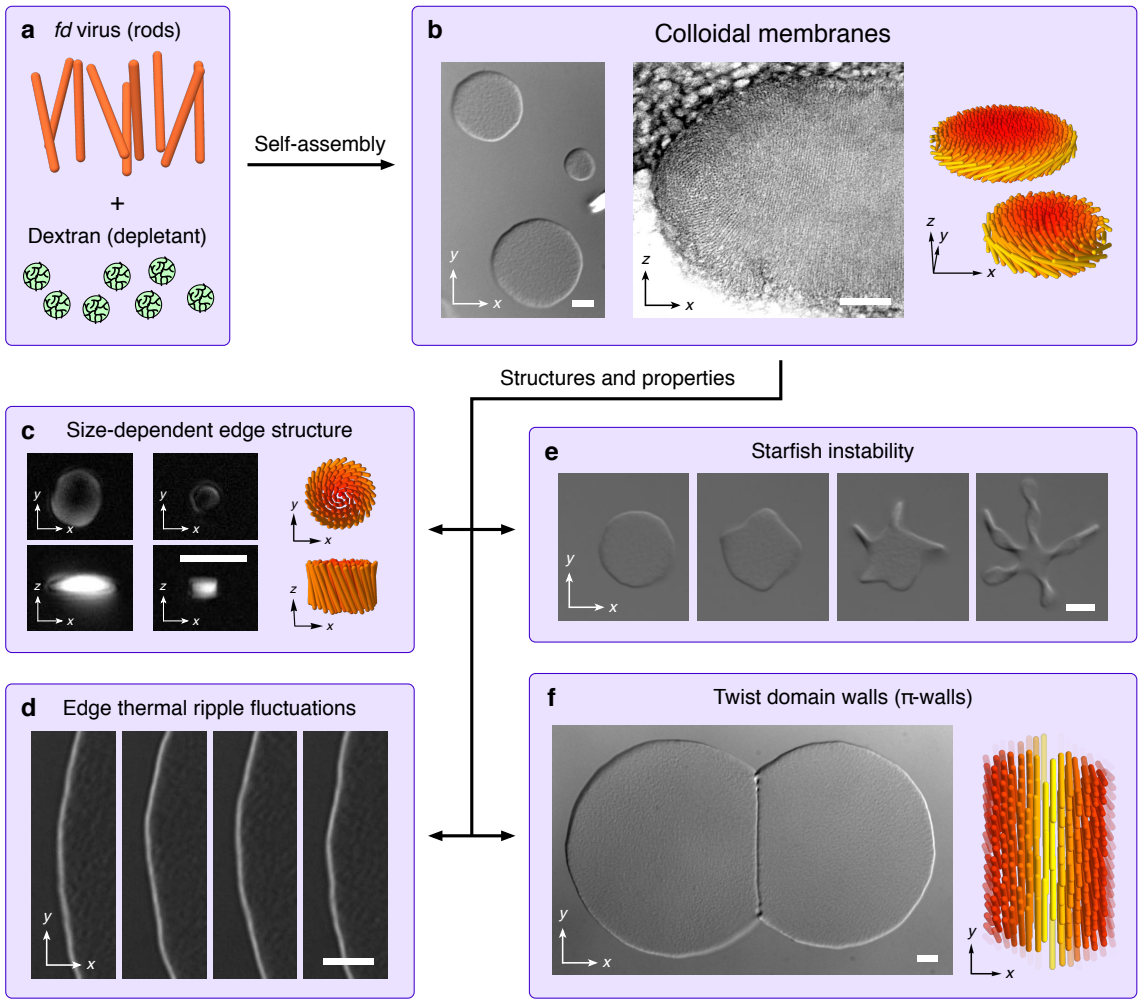

Figure 3.1: Overview of single-component colloidal membranes. (a) *fd* virus particles and dextran molecules act as rod-shaped colloids and spherical depletants, respectively. (b) Depleting molecules condense a dilute isotropic virus suspension into a liquid-like colloidal monolayer of aligned rods. From left to right, differential interference contrast (DIC) image of circular membranes of various sizes, transmission electron microscopy image showing a curved cross-section of the edge of a large membrane, and schematic of two large circular membranes of opposite chirality. (c) From left to right, top- and side-view LC-Polscope images of a medium-sized membrane, top- and side-view LC-Polscope images of a small membrane, and top- and side-view LC schematics of a small membrane. Along with (b), these images illustrate that edges of smaller membranes are more squared. (d) DIC images of thermally-excited ripple fluctuations at four different times. (e) DIC images of a temperature induced transition of a flat 2D colloidal membrane (left) into a structure with a starfish morphology (right). (f) DIC image (left) and schematic (right) of a twist domain wall, or π-wall, formed from two partially-coalesced circular membranes. (b) (left), (c), (d), (e), (f) Scale bars, 4 µm. (b) (middle) Scale bar, 0.2 µm. Experimental data and methods are reported in Ref. [84]

citations, membrane edges undergo ripple fluctuations that can be visualized and precisely quantified (Fig. 3.1d).

When chirality-inverted Y21M viruses (*fd*-Y21M) are used instead of *fd*-wt, rods at the edge twist with the opposite handedness (right instead of left), and when a macroscopically achiral mixture of wildtype and Y21M viruses is used, edge-bound rods in each membrane have equal probability of twisting with one handedness or the other [89]. The achiral mixture exhibits spontaneous symmetry breaking, which has been used in sensors of molecular chirality [13] and which has been observed in Langmuir-Blodgett films [90, 91], another class of two-dimensional structures with nanoscale components. Increasing the rod chirality raises the free energy of interior untwisted rods while lowering the free energy of edge-bound twisted rods, leading to chiral control of edge line tension [89]. At sufficiently high chirality, the edge tension approaches zero, and a flat 2D disk spontaneously transitions into an array of 1D twisted ribbons, called a "starfish" (Fig. 3.1e).

The twist associated with the membranes edge also leads to unconventional pathways of membrane coalescence [92]. As two membranes of same chirality approach each other laterally, the proximal membrane edges can partically coalesce and localize 180° of twist to a 1D structure between the membranes; consequently, such structures are called π-walls (Fig. 3.1f). The rods twist by 180° along the axis connecting the two membranes, from one side of the π-wall to the other. At the middle of the π-wall, the rods point in the plane of the membranes.

A second species of virus called M13KO7 has a longer 1200 nm contour length. Like *fd*-wt virus, it has 7 nm diameter and 2.8 µm persistence length and forms bulk cholesteric phases with right-handed twist [79]. Membranes with remarkable phase-separated structures can be formed from a mixture of these viruses and the shorter, left-handed *fd*-Y21M viruses [79]. At low depletant concentrations, the two species fully mix (Fig. 3.2b), and at high depletant concentrations, the two species completely phase separate with a circular *fd*-Y21M domain surrounded by M13KO7 viruses (Fig. 3.2d). At intermediate depletant concentrations, circular finite-sized rafts of *fd*-Y21M viruses appear in a partially phase-

separated background membrane enriched in M13KO7 viruses (Fig. 3.2c).

After membrane formation, these finite-sized rafts exchange *fd*-Y21M viruses with the background membrane to attain a thermodynamically preferred raft size (Fig. 3.2e). That is, rafts smaller than the preferred size will gain viruses and larger rafts will lose viruses [79]. At long times ($\sim$24 h), membrane rafts all become roughly the same size. These rafts can diffuse within the background membrane, but they repel each other to maintain approximately equal spacing. Moreover, when two rafts are brought close together by optical traps and released, they will move away from each other (Fig. 3.2f) [79].

Colloidal membranes exhibit an exceedingly rich phenomenology. All of these complex mesoscopic behaviors arise from very simple microscopic interactions between constituent particles. Filamentous viruses interact only through an effective hard-rod repulsion. Similarly, the uncharged dextran molecules act as effective Asakura-Oosawa penetrable spheres [85, 86]. From this perspective, the virus particles and dextran molecules comprise a gas of hard rods and hard spheres, and the structures found in colloidal membranes must be stabilized by entropic, hard-core interactions [93]. We formulate a theoretical model based purely on such entropic considerations. Our model explains many known structural features of colloidal membranes and directly relates them to the known entropic interactions in rod/polymer mixtures. Furthermore, it makes a number of new predictions that are directly verified by new experimental results.

3.2 Single-component membrane structures

3.2.1 Membrane parametrization and free energy

We first model single-component membranes formed from *fd* virus. In our model, we treat the membrane as a continuous fluid composed of rods at constant mass density. Once the membrane is stably formed, we assume it does not exchange rods with the surrounding solution; thus, its volume is fixed. The membrane structure is characterized by two coarse-grained degrees of freedom available to the rods: a twist angle $\theta(\mathbf{x})$ about an axis in the

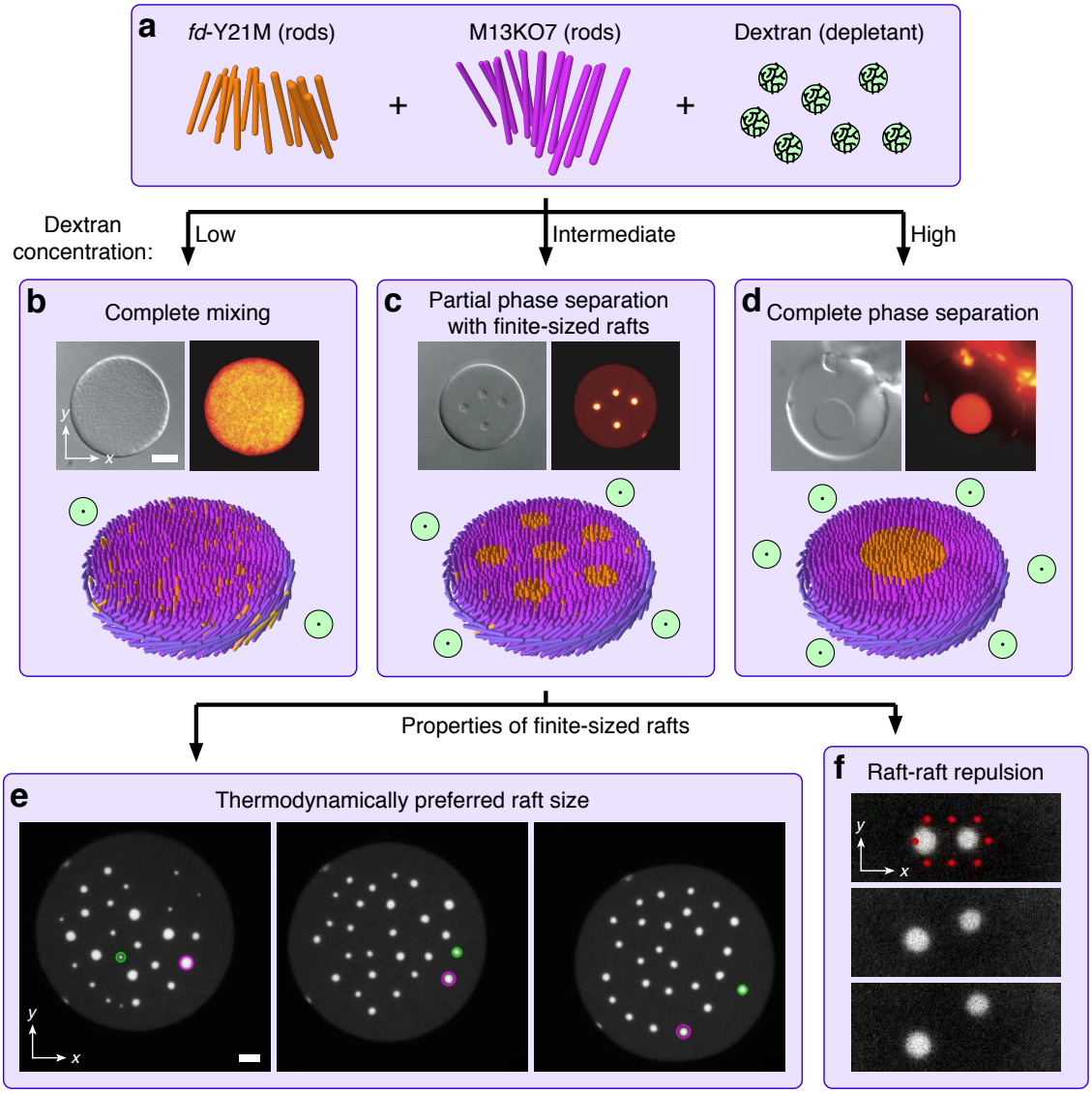

Figure 3.2: Overview of two-component colloidal membranes with rafts. (a) Virus particles and dextran molecules act as rod-shaped colloids and spherical depletants, respectively. *fd*-Y21M viruses are shorter and prefer right-handed twist. M13KO7 viruses are longer and prefer left-handed twist [79]. Each (b)–(d) contains a DIC image (top, left), a fluorescence image with *fd*-Y21M labeled (top, right), and a schematic (bottom) of a depletion-induced colloidal membrane. (b) At a low dextran concentration $n = 34\,\mathrm{mg\,mL^{-1}}$, the two virus species completely mix. (c) At an intermediate dextran concentration $n = 38\,\mathrm{mg\,mL^{-1}}$, finite-sized rafts of *fd*-Y21M virus form in a partially phase-separated background. (d) At a high dextran concentration $n = 52\,\mathrm{mg\,mL^{-1}}$, the two virus species completely phase separate. (e) Rafts exchange rods with the background membrane to attain a thermodynamically preferred size. Fluorescence images with *fd*-Y21M labeled taken 6.7 h apart. Green and purple circles track two rafts that start respectively smaller and larger than the preferred raft size. (f) Rafts repel one another. Fluorescence images with *fd*-Y21M labeled taken 5 s apart. Two optical plows consisting of multiple light beams (red dots) bring two rafts together and are then switched off. Scale bars, 5 µm. Experimental data and methods are reported in Ref. [79].

membrane plane and a root-mean-square amplitude $b(\mathbf{x})$ of height fluctuations perpendicular to the membrane plane. Perpendicular fluctuations increase the effective thickness of the membrane, and instead of using $b(\mathbf{x})$ directly, we will develop a microscopic theoretical model and present its results using the coarse-grained membrane half-thickness $h(\mathbf{x}) = t\cos\theta(\mathbf{x}) + b(\mathbf{x})$, where t is the half-length of the virus. We will first develop the model assuming a circularly-symmetric membrane of radius R and using cylindrical coordinates in which $h(r)$, $b(r)$, and $\theta(r)$ only depend on the radial coordinate (Fig. 3.3).

We model the rods as liquid crystals whose orientations are described by a chiral Frank elastic free energy [14]. In a circular geometry, the rods point in the z-direction but can tilt with angle θ in the azimuthal direction (Figs. 3.3a and b). Using the one-constant approximation, the free energy is:

$$F_{\text{Frank}} = K\int \mathrm{d}^2\mathbf{x}\, h\left[(\boldsymbol{\nabla}\cdot\mathbf{n})^2 + (\boldsymbol{\nabla}\times\mathbf{n})^2 - 2q\mathbf{n}\cdot\boldsymbol{\nabla}\times\mathbf{n}\right] \tag{3.2.1}$$

$$= 2\pi K\int_0^R \mathrm{d}r\, h\left[r(\partial_r\theta)^2 + \sin 2\theta\,\partial_r\theta + \frac{\sin^2\theta}{r} - 2qr\partial_r\theta - q\sin 2\theta\right]. \tag{3.2.2}$$

K is the 3D Frank elastic modulus and q is the preferred twist wavenumber associated with intrinsic chirality of the constituent rods. $\mathbf{n}(r) = \sin\theta(r)\hat{\boldsymbol{\phi}} + \cos\theta(r)\hat{\mathbf{z}}$ is the nematic director. The q term breaks chiral symmetry, such that for $q > 0$, twisted membranes with $\partial_r\theta > 0$ have lower energy than those with $\partial_r\theta < 0$. When $q = 0$, the total free energy is invariant under the chirality inversion $\theta \to -\theta$. We do not include a saddle-splay term proportional to K_{24}. It would presumably depend on the difference between the two principal curvatures at the membrane boundary (Eq. 2.3.2), but the curvature along the z-direction of Figs. 3.3a and b at $r = R$ is not a valid continuum quantity for a monolayer.

The depletant polymers act to minimize the volume excluded to them by the membrane. For polymers small compared to the dimensions of the membrane, this excluded volume is approximately $V_0 + aA$, where V_0 is the volume of the membrane, A is the surface area of the membrane, and a is the characteristic depletant radius [94] (Fig. 3.3c). V_0 is constant, so depletion serves as an effective surface tension. Its free energy is calculated via the

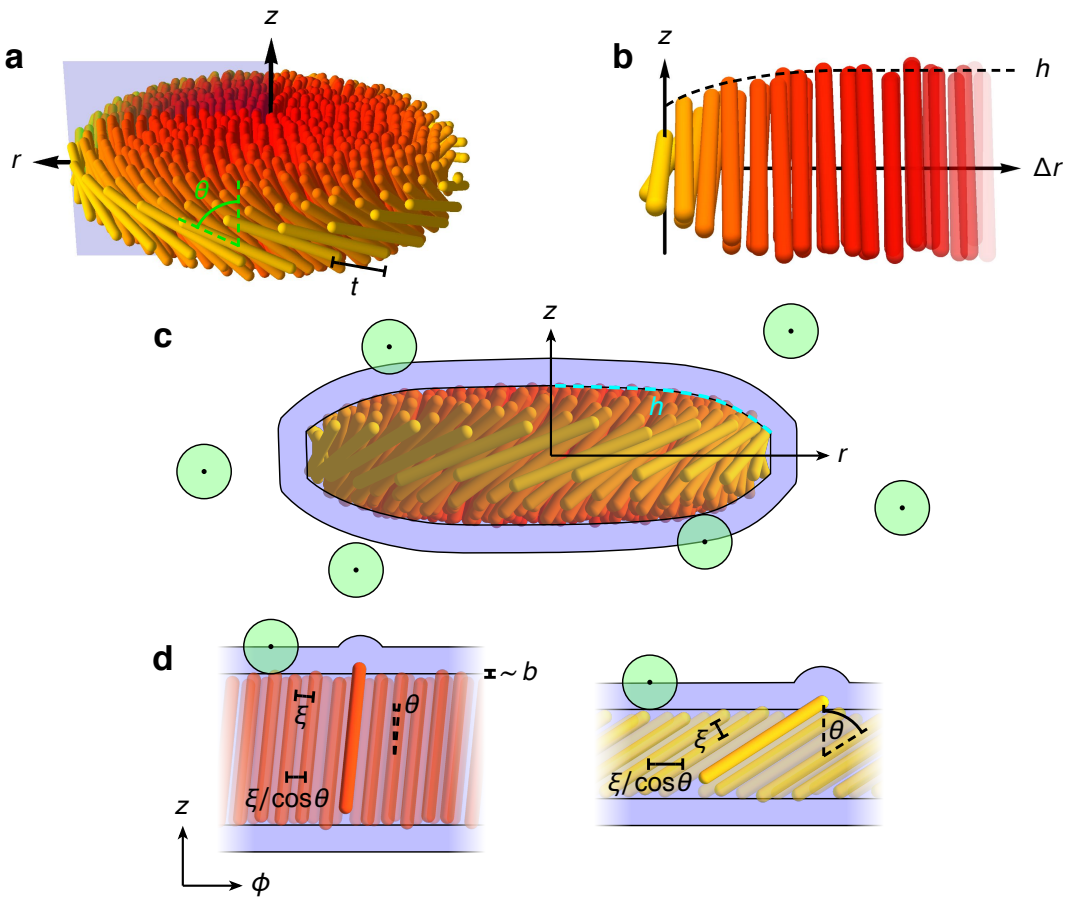

Figure 3.3: Membrane parametrization and depletion contributions to the free energy. Depleting molecules (dextran polymers in our system) are illustrated in green, and the volume excluded to them by the membrane is illustrated in blue. (a) Perspective and (b) cross-section schematics show parametrization of the membrane edge profile and the cylindrical coordinate system. (b) shows rods that intersect the light blue plane in (a). Δr is a reverse radial coordinate where $\Delta r = 0$ corresponds to the membrane edge. h is the membrane half-thickness and θ is the rod tilt angle. t is the half-length of the rods. (c) The volume that is excluded to the depleting polymer due to a smooth membrane is comprised of the volume of the membrane itself and to a first order the membrane surface area times the depletant radius. (d) The free energy density of rod height fluctuations b are calculated in the mean-field limit by considering a single protruding rod amid a membrane of constant local thickness: (top) rods at small tilt angle θ and (bottom) rods at large θ. The magnitude of this free energy density decreases with increasing θ because tilted rods are less dense in the membrane plane by a factor of $\cos\theta$, assuming a constant perpendicular distance ξ between rods. In other words, the surface roughness lengthscale in the ϕ-direction is proportional to $1/\cos\theta$, or equivalently, the extra effective surface area created by fluctuations is proportional to $\cos\theta$.

ideal gas partition function $V^N/N!\Lambda^{3N}$ applied to N depletant molecules, where Λ is their thermal de Broglie wavelength. The volume V available to the depletants can be written as $V = V_\mathrm{t} - V_0 - aA$, where $V_\mathrm{t} \gg V_0$ is the total volume of the virus-and-depletant suspension. Ignoring constant terms, the depletant free energy is

$$\begin{aligned} F_\mathrm{dep} &= -NT \log \frac{V_\mathrm{t} - V_0 - aA}{V_\mathrm{t} - V_0} \\ &\approx nTaA \\ &= 2naT \left[\int \mathrm{d}^2\mathbf{x} \sqrt{1 + (\boldsymbol{\nabla} h)^2} + \int \mathrm{d}l\, h \right] \qquad (3.2.3) \\ &= 4\pi naT \left[\int_0^R \mathrm{d}r\, r \sqrt{1 + (\partial_r h)^2} + Rh(R) \right], \qquad (3.2.4) \end{aligned}$$

where n is the depletant concentration and T is the temperature. $\int \mathrm{d}l$ indicates an integral over the membrane edge boundary.

Finally, we allow rods to fluctuate perpendicular to the membrane plane. Protrusion of each rod increases the effective surface area of the membrane, which decreases the volume accessible to the depletant molecules. In general, these fluctuations have complicated, non-linear effects on the free energy, but for simplicity, we only consider fluctuations of single rods and ignore their interactions and correlations [78]. When a single rod at small tilt angle θ protrudes by a small perpendicular distance z above a flat coarse-grained membrane surface, it introduces an additional spherical cap of volume $\pi a z^2$ that is excluded to the depleting polymers (see Fig. 3.3d). Meanwhile, these protrusions are entropically favored by the rods. For a distribution of vertical rod displacements $p(z)$, the fluctuation free energy for a single rod is a sum of depletant and rod entropy contributions:

$$F_\mathrm{single} = \pi naT \int \mathrm{d}z\, p(z) z^2 + T \int \mathrm{d}z\, p(z) \log p(z).$$

Minimizing this free energy subject to the constraint $\int \mathrm{d}z\, p(z) = 1$ yields $p_0(z) = (2\pi b_0^2)^{-1/2} \exp(-z^2/2b_0^2)$, where $b_0 = (2\pi na)^{-1/2}$. Thus, the preferred magnitude of rod height fluctuations b_0 is determined by a trade-off between rod entropy, which prefers larger b, and the depletion effect,

which tends to minimize b.

If all rods were to fluctuate with the preferred amplitude b_0, then the membrane half-thickness h and rod angle θ would be exactly related as $h = t\cos\theta + b_0$. However, in certain structures such as the mid-planes of π-walls, the Frank and depletion free energies favor profiles $h(x)$ and $\theta(x)$ that significantly deviate from this relationship. To properly describe these structures and account for the energetic cost of $h \neq t\cos\theta + b_0$, we calculate the free energy of Gaussian rod fluctuations of amplitude $b \neq b_0$. Using the distribution $p(z) = (2\pi b^2)^{-1/2}\exp(-z^2/2b^2)$, the single-rod free energy becomes $F_{\text{single}} = 2\pi naT(b-b_0)^2$ to leading order in $b - b_0$. To coarse-grain this expression, we multiply by the rod density and integrate over the membrane area. For simplicity, we assume the rods are packed hexagonally and maintain a constant perpendicular distance ξ between nearest-neighbors. In the small θ limit, the area occupied by each rod is $\sqrt{3}\xi^2/\cos\theta$. Our final expression for the rod fluctuation free energy is

$$F_{\text{rod}} = \frac{8\pi^2 naT}{\sqrt{3}\xi^2}\int_0^R \mathrm{d}r\, r\cos\theta\,(h - t\cos\theta - b_0)^2\,, \tag{3.2.5}$$

where we have written b in terms of h and θ. This term allows h to deviate from $t\cos\theta + b_0$ with an energy penalty corresponding to the magnitude of the deviation.

In our system, the preferred magnitude of this effective surface roughness is very small—$b_0 \ll t$—but the energetic cost of deviations from this value depends on the rod angle θ (Fig. 3.3d). When $\theta \approx 0$, rods are packed more closely in the plane of the membrane, assuming a constant perpendicular distance ξ between rods. Thus, rod fluctuations produce surface roughness on a smaller length scale, which creates more effective surface area and costs more energy. In this case, $b = b_0$ is strongly preferred, so $h \approx t\cos\theta$ and rod entropy can be ignored. When $\theta \sim 1$, rods are spaced farther apart in the plane of the membrane, leading to fluctuation-produced surface roughness on larger length scales. These longer-wavelength fluctuations resist $b = b_0$ more weakly, so h may differ significantly from $t\cos\theta$. In a similar fashion, manipulating the surface roughness of larger colloids can tune their depletion-induced interaction [95, 96]. In summary, the rod fluctuation term couples h to

$t\cos\theta$ with a θ-dependent coupling strength.

We minimize the total free energy with volume-conserving Lagrange multiplier λ

$$F = F_{\text{dep}} + F_{\text{Frank}} + F_{\text{rod}} + \lambda\left[V_0 - 4\pi\int_0^R \mathrm{d}r\, rh\right] \tag{3.2.6}$$

over $h(r)$ and $\theta(r)$ to obtain the edge profile. The boundary conditions are $h(0) = t + b_0$ and $\theta(0) = 0$; $h(R)$ and $\theta(R)$ are free.

Equation 3.2.6 simplifies for large membranes when R is much greater than the penetration depth of edge twist l_{twist}; the edge becomes essentially straight. We can then study the profile of a twisted membrane formed from an untwisted rectangular membrane of length $L_y \to \infty$ along the y-direction and length $2L_x \ll L_y$ along the x-direction. We allow the membrane profile to vary along the x-direction and impose reflection symmetry about the midline $x = L_x$ where the rods are perpendicular to the membrane (analogous to $r = 0$ for the original circular geometry). We are interested in the edge profile at $x = 0$. In this setup, each free energy integral becomes its Cartesian version, with F_{Frank} losing bend distortion terms that arise from a circular geometry. Instead of a Lagrange multiplier term, however, volume conservation can be directly enforced in the following way. The volume of the half of the untwisted membrane between $x = 0$ and $x = L_x$ is $V_0 = 2(t + b_0)L_xL_y$. The change in volume brought about by a varying $h(x)$ is $\Delta V = 2L_y\int_0^{L_x}\mathrm{d}x\,[h(x) - (t + b_0)]$. To compensate for the lost volume, we introduce extra volume at the membrane midline where $h(x) = t + b_0$ by adding a width ΔL_x of untwisted rods; volume conservation requires $\Delta L_x = -\Delta V/[2(t + b_0)L_y] = \int_0^{L_x}\mathrm{d}x\,[1 - h(x)/(t + b_0)]$. This extra width increases the half-membrane's surface area by $\Delta A = 2L_y\Delta L_x$ and, since depletion free energy is proportional to surface area, contributes the additional term $naT\Delta A$ to F_{dep}. Ignoring a constant term

proportional to $L_x L_y$, the total free energy becomes

$$\begin{aligned}\frac{F}{2naTL_y} = &\int_0^{L_x} \mathrm{d}x \left(\sqrt{1+(\partial_x h)^2} - \frac{h}{t+b_0}\right) + h(0) \\ &+ \frac{kt}{2}\int_0^{L_x} \mathrm{d}x\, h\left[(\partial_x\theta)^2 + 2q\partial_x\theta\right] \\ &+ \frac{2\pi}{\sqrt{3}\xi^2}\int_0^{L_x} \mathrm{d}x \cos\theta (h - t\cos\theta - b_0)^2, \end{aligned} \tag{3.2.7}$$

where again, $k = K/natT$. Strictly speaking, the integrals in the last two terms should extend from 0 to $L_x + \Delta L_x$, but the contributions to the integrals from L_x to $L_x + \Delta L_x$ are zero because $\partial_x\theta = 0$, $\theta = 0$, and $h = t + b_0$ in the interior of the membrane. Comparing Eqs. 3.2.6 and 3.2.7, the additional surface area term is analogous to a Lagrange multiplier with value $naT/(t + b_0)$, the effective osmotic pressure exerted by the depletants on the membrane. Also, since this Cartesian parametrization implicitly inverts the membrane orientation compared to the cylindrical parametrization (instead of decreasing r, increasing x moves into the interior of membrane), the q-term in Eq. 3.2.7 has the opposite sign of the q-terms in Eq. 3.2.2.

In order to obtain quantitatively meaningful results, we use parameter values that are extracted from relevant experimental measurements when possible (Table 3.1). Five parameters, whose values are neither experimentally controlled nor directly measured, are allowed to vary as fit parameters: the characteristic depletant size a, the Frank elastic modulus K in the one-constant approximation, the amplitude and transition temperature of the temperature-dependent twist wavenumber $q(T)$, and the virus birefringence Δn. In our theory, we maintain the experimentally-measured square-root behavior of $q(T)$ (see Supplementary Material of [89]). The Frank elastic modulus can be written in dimensionless form as $k(T) \equiv K/natT$, a ratio between the influence of Frank elasticity and that of depletion. Presumably, K depends on temperature in a complicated fashion, as measured for a variety of lyotropic and thermotropic liquid crystals [26, 44, 97, 98], but we ignore this effect.

Table 3.1: Single-component membrane parameters and their values.

Parameter	Variable	Experimental value	Reference(s)	Theoretical fit value
Temperature	T	0–60 °C	experimental	same
Dextran concentration	n	35–51 mg mL^{-1}	experimental	same
Dextran radius	a	∼25 nm	[99–101][1]	31 nm
fd-wt half-length	t	440 nm	[81]	same
Nearest-neighbor *fd*-wt distance	ξ	12 nm	unpublished[2]	same
fd-wt Frank constant	K	0.5 pN	[83][3]	2.8 pN
fd-wt twist wavenumber	$q(T)$	$0.5\,\mu\text{m}^{-1} \times \sqrt{1 - T/60\,^\circ\text{C}}$	[89][3]	$2.5\,\mu\text{m}^{-1} \times \sqrt{1 - T/120\,^\circ\text{C}}$
fd-wt birefringence	Δn	0.0087	[88][4]	0.0065

[1] Hydrodynamic radii for dilute solutions of 500 kDa dextran, whereas our experiments are in the semidilute regime.

[2] Unpublished data extracted from X-ray scattering.

[3] Measured in the bulk cholesteric phase with *fd* virus concentration 100 mg mL^{-1}, which is lower than the membrane virus concentration 230 mg mL^{-1} estimated from the experimentally-measured nearest-neighbor virus distance ξ.

[4] Assuming that the nematic order parameter in membrane is 1. Membrane virus concentration 230 mg mL^{-1} estimated from the experimentally-measured nearest-neighbor virus distance ξ.

3.2.2 Membrane edge structure

We first use our theoretical model to determine how membrane structure depends on its radius. Figure 3.4 plots the vertical membrane profile for membranes with very large radii and varying Frank-to-depletion ratios k and twist wavenumbers q. For all conditions, $h \approx t\cos\theta$, indicating that θ is sufficiently small to suppress rod height fluctuations. Thus, rod entropy does not contribute significantly to the structure of the membrane's edge. First, consider the $q = 0$ profiles in Fig. 3.4 corresponding to a macroscopically achiral rod mixture. When k is greater than a critical value $k_c = 1$, the untwisted configuration with $\theta = 0$ is favored. When $k < k_c$, depletion drives spontaneous chiral symmetry breaking into a twisted configuration with either $\theta > 0$ or $\theta < 0$. In the $k \to 0$ limit where only depletion exists, the vertical edge profile is semicircular to minimize the membrane surface area. Now, consider the $q = 2.2\,\mu\text{m}^{-1}$ case in Fig. 3.4 corresponding to a chiral rod mixture. Twisted configurations of one handedness (here, $\theta > 0$ for $q > 0$) become favored at all k. In the depletion-dominated regime $k \ll 1$, the vertical edge profile again approaches a semicircle. In the Frank-elasticity-dominated regime $k \gg 1$, the rod twist decays with penetration length $l_{\text{twist}} \approx \sqrt{k}/t$, in analogy to the way that twist penetrates into a smectic phase.

For membrane edges calculated in Fig. 3.4, $h \approx t\cos\theta$, which means rod height fluctuations b are strongly suppressed. This motivates simplification of the free energy by taking the infinite coupling limit in which F_{rod} enforces $h = t\cos\theta + b_0$ and therefore disappears from the free energy. Using values in Table 3.1, we calculate $b_0 \approx 0.03t$ and make the further approximation that these protrusion fluctuations contribute only a small fraction to the membrane thickness and can thus be neglected: $b_0 = 0$. Numerical calculations of all edge properties fixing $h = t\cos\theta$ are indistinguishable from those using the full theory. Thus, the precise form of F_{rod}, whose derivation required many assumptions, does not matter for membrane edges as long as it strongly couples h to $t\cos\theta$.

This simplification permits derivation of some analytical results. The free energy can then be expressed in terms of θ only. In a dimensionless form with $\tilde{x} \equiv x/t$, $\tilde{L}_x \equiv L_x/t$,

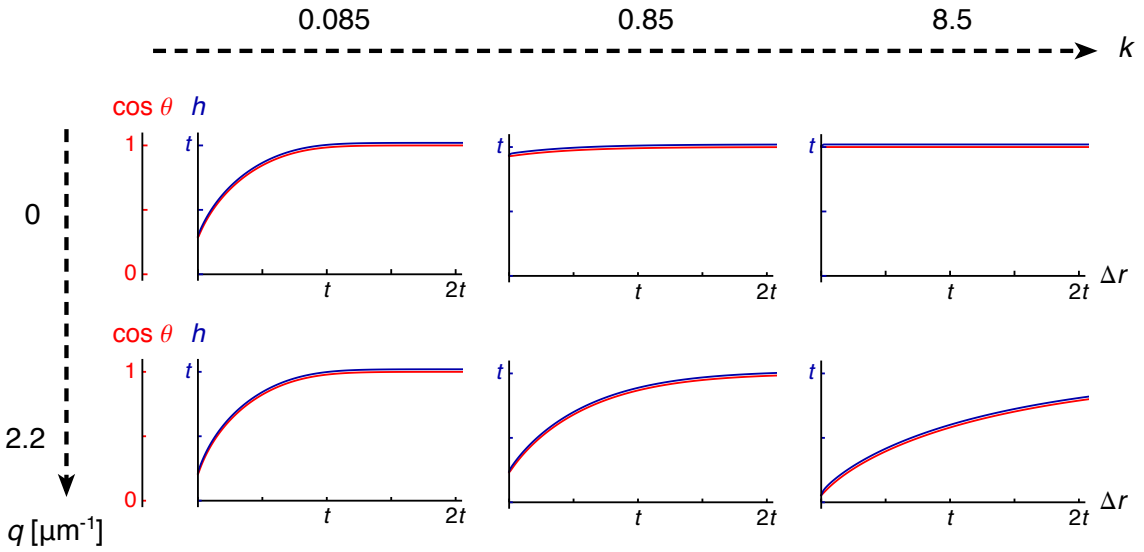

Figure 3.4: Calculated vertical edge profiles of a large membrane (radius $R \gg t$) with various Frank-to-depletion ratios k from left to right and preferred twist wavenumbers q from top to bottom. In all cases, h (blue) is almost indistinguishable from $t\cos\theta$ ($\cos\theta$ in red). Note that for $q = 0$ and $k < 1$, $\theta \neq 0$, demonstrating spontaneous symmetry breaking into a configuration with one handedness ($\theta > 0$) or the other ($\theta < 0$). For $q = 0$ and $k \geq 1$, the untwisted state with $\theta = 0$ has lowest energy. Experimental conditions listed in Table 3.1 are closest to $k = 0.85$ and $q = 2.2\,\mu\text{m}^{-1}$.

$\tilde{q} \equiv qt$, and $\tilde{F} \equiv F/2natTL_y$,

$$\tilde{F} = \int_0^{\tilde{L}_x} \mathrm{d}\tilde{x} \left(\sqrt{1 + \sin^2\theta\,(\partial_{\tilde{x}}\theta)^2} - \cos\theta \right) + \cos\theta(0) + \frac{k}{2}\int_0^{\tilde{L}_x} \mathrm{d}\tilde{x}\, \cos\theta\,(\partial_{\tilde{x}}\theta)^2 - k\tilde{q}\sin\theta(0). \tag{3.2.8}$$

To investigate the onset of twist, we expand this free energy for small θ. To third order, the first integral of the Euler-Lagrange equation gives

$$\sqrt{k}\partial_{\tilde{x}}\theta = -\theta + \frac{12 - 5k}{24k}\theta^3.$$

This equation at $\tilde{x} = 0$ can be combined with the variational boundary condition

$$k\partial_{\tilde{x}}\theta(0) = -k\tilde{q} - \theta(0) + \tilde{q}\theta^2(0) + \frac{3 - k}{3k}\theta^3(0)$$

to obtain $\theta(0)$. We first consider $\tilde{q} = 0$, so $\tilde{F}$ has chiral symmetry. We find a twist solution

when $k < k_c = 1$, where

$$\theta(0) \approx \pm\sqrt{\frac{4}{3}(1-k)} \tag{3.2.9}$$

close to the critical point. When $k > 1$, only the trivial $\theta = 0$ solution exists. If we allow a small nonzero $\tilde{q}$ to break the chiral symmetry, a twist solution appears above k_c:

$$\theta(0) \approx \frac{k\tilde{q}}{\sqrt{k}-1}. \tag{3.2.10}$$

We can integrate the Euler-Lagrange equation to leading order and obtain

$$\theta(\tilde{x}) \approx \theta(0)\exp(-\tilde{x}/\sqrt{k}). \tag{3.2.11}$$

The vertical edge profiles plotted in Fig. 3.4 take this form for $k \gg 1$. $\sqrt{k}t$ acts as a twist penetration depth l_{twist} in analogy to smectic phases. Free energy calculations confirm that the twist solutions are favored whenever they exist. Thus, when $q = 0$, the phase transition at the $k_c = 1$ critical point is second-order and spontaneously breaks chiral symmetry. Above k_c, there is a critical second-order line at $q = 0$.

We also analytically investigate the edge profile when $k \ll 1$. It is more convenient to write the free energy (Eq. 3.2.8) in terms of $\tilde{h} \equiv h/t = \cos\theta$:

$$\tilde{F} = \int_0^{\tilde{L}_x} \mathrm{d}\tilde{x}\left(\sqrt{1+(\partial_{\tilde{x}}\tilde{h})^2} - \tilde{h}\right) + \tilde{h}(0) + \frac{k}{2}\int_0^{\tilde{L}_x} \mathrm{d}\tilde{x}\frac{\tilde{h}(\partial_{\tilde{x}}\tilde{h})^2}{1-\tilde{h}^2} - k\tilde{q}\sqrt{1-\tilde{h}^2(0)}. \tag{3.2.12}$$

We chose the sign of the square-root in the last term assuming $\theta > 0$, so this expression applies for $q > 0$. If $q < 0$, then $\theta < 0$ configurations have lower energy and we should choose the opposite sign. The first integral of the Euler-Lagrange equation gives

$$0 = \frac{1}{\sqrt{1+(\partial_{\tilde{x}}\tilde{h})^2}} - \tilde{h} - \frac{k}{2}\frac{\tilde{h}(\partial_{\tilde{x}}\tilde{h})^2}{1-\tilde{h}^2}.$$

This equation at $\tilde{x} = 0$ can be combined the variational boundary condition

$$0 = \frac{\partial_{\tilde{x}}\tilde{h}(0)}{\sqrt{1 + (\partial_{\tilde{x}}\tilde{h}(0))^2}} - 1 + k\frac{\tilde{h}(0)\partial_{\tilde{x}}\tilde{h}(0)}{1 - \tilde{h}^2(0)} - k\tilde{q}\frac{\tilde{h}(0)}{\sqrt{1 - \tilde{h}^2(0)}}$$

to obtain a twist solution as a power series in k:

$$\tilde{h}(0) \approx \sqrt{\frac{27}{32}}k - \frac{9}{8}k\tilde{q}. \tag{3.2.13}$$

Solving the Euler-Lagrange equation with $k = 0$ yields a circular profile

$$\tilde{h}(\tilde{x}) \approx \begin{cases} \sqrt{2\left(\tilde{x} + \frac{\tilde{h}^2(0)}{2}\right) - \left(\tilde{x} + \frac{\tilde{h}^2(0)}{2}\right)^2} & 0 \leq \tilde{x} \leq 1 - \frac{\tilde{h}^2(0)}{2} \\ 1 & 1 - \frac{\tilde{h}^2(0)}{2} \leq \tilde{x}. \end{cases} \tag{3.2.14}$$

The vertical edge profiles plotted in Fig. 3.4 take this form for $k \ll 1$. However, since $\cos\theta(0) = \tilde{h}(0) \ll 1$, the coupling in F_{rod} may be weak. Calculations using the full free energy should be performed to check if $h = t\cos\theta$ is a valid assumption.

In addition to describing edges of large membranes, our theoretical model also describes how edge profile varies with decreasing membrane diameter. To test these predictions, we measure the retardance of different-sized membranes using quantitative LC-PolScope microscopy, which directly reveals the twisting of rods away from the membrane normal [84]. When polarized light passes through a birefringent material, the components corresponding to the dielectric tensor eigenvectors—the ordinary and extraodinary waves—propagate at different speeds. The resulting phase difference between these components multiplied by the wavelength of the light is the retardance D. For a uniaxial crystal of constant thickness, retardance can be calculated as $D = 2\Delta n h \sin^2\theta$ [102], where Δn is the birefingence. For membranes of various radii, we calculate $D(\Delta r)$ with the fit values given in Table 3.1 and the approximation $h = t\cos\theta$, since our results in Fig. 3.4 demonstrate that rod fluctuations b are insignificant for membrane edges. We use the same parameter values for all membrane sizes; only the radius changes. The raw calculated retardance profiles are convolved with

a Gaussian of width 0.13 µm representing the microscope's resolution function, exactly as done in Ref. [88]. The radially-averaged edge retardance profiles measured for membranes of various radii match well with our theoretical predictions (Fig. 3.5b). These results demonstrate that rods are less tilted at the edges of smaller membranes compared to those of larger membranes (insets of Fig. 3.5b), consistent with observations that larger membranes appear on side-view to have rounded edges while smaller membranes have squared-off edges (Figs. 3.1b and c).

3.2.3 Membrane π-wall structure

We also use our theoretical model to quantitatively explain another prominent and experimentally-characterized feature of colloidal membranes: the π-wall. we use Eq. 3.2.7 without the boundary depletion term proportional to $h(0)$ because $x = 0$ is the middle of the wall and no longer an edge boundary (Figs. 3.6a and b). The rods there must lie in the membrane plane, so we gain the extra boundary condition $\theta(0) = \pi/2$. Fig. 3.6c plots their vertical profiles over a range of Frank-to-depletion ratios k and chiral twist wavenumbers q. In all cases, h is much greater than $t\cos\theta$ at the middle of the wall, since the coupling that sets $h \approx t\cos\theta$ becomes very weak when $\theta \approx \pi/2$. Remember, $h = t\cos\theta + b$, where b is the amplitude of rod fluctuations perpendicular to the membrane. This means these rods undergo position fluctuations in the z-direction that are many times larger than both their projected height $t\cos\theta$ and their diameter $d \approx 0.02t$. Such a phenomenon would require rods to pass through each other, which is theoretically allowed because we ignore rod-rod interactions, but we wish to interpret this result physically. $h \gg t\cos\theta$ and $h \gg d$ indicate that the membrane is thicker than multiple layers of tilted rods, so these large fluctuations may be physically manifested as rods stacking on top of each other. The addition of repulsive rod-rod interactions may further increase the thickness of the π-wall. Now we consider the full π-wall vertical profiles in Fig. 3.6c. In similar fashion to the membrane edge, the depletion-dominated regime $k \ll 1$ leads to a circular profile and the Frank-elasticity-dominated regime $k \gg 1$ leads to slow rod twist decay. With the same parameters used

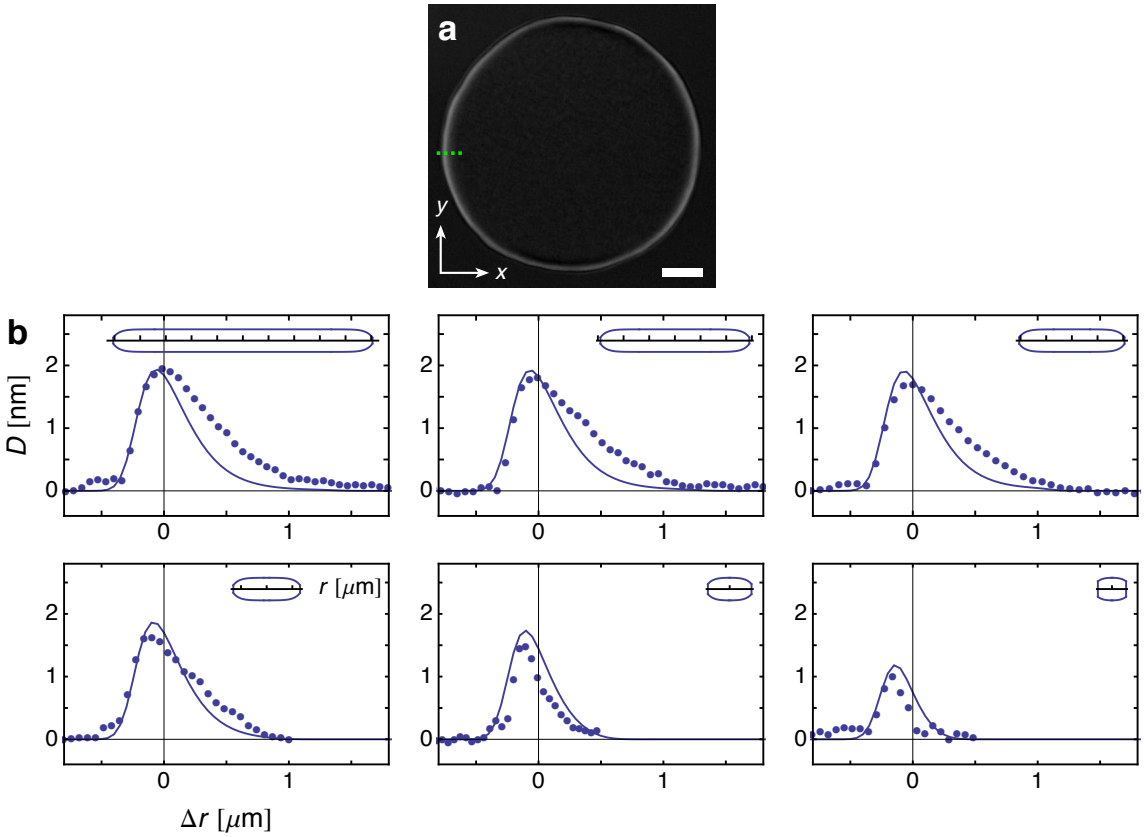

Figure 3.5: Edge retardance for membranes of different sizes. (a) 2D LC-PolScope birefringence map of a large circular membrane with retardance represented as pixel brightness. The dotted green line approximately corresponds to the range of Δr's plotted in (b). Scale bar, 4 µm. (b) Retardance values D for circular membranes of various sizes. The points indicate experimental data at temperature $T = 22\,^{\circ}\mathrm{C}$ and depletant concentration $n = 45\,\mathrm{mg\,mL^{-1}}$. The lines indicate theoretical results calculated with these parameter values and those described in Table 3.1, giving $k = 0.85$ and $q = 2.2\,\mu\mathrm{m}^{-1}$. Membrane radii range from 5.1 µm (top left) to 0.45 µm (lower right). The insets show the calculated membrane profile $h(r)$, plotted with an aspect ratio of 1. Tick marks signify 1 µm increments. $t\cos\theta$, not shown, is strongly coupled to h in all cases. Experimental data and methods reported in Ref. [84].

to calculate the edge structure (Table 3.1), the calculated optical retardance of the π-wall quantitatively matches the experimentally measured profile (Fig. 3.7).

q does not significantly affect the π-wall profile among the parameter values explored; indeed, it appears in a θ-dependent free energy term that can almost be integrated to the boundary, and $\theta(0)$ and $\theta(L_x)$ are fixed. If h were forced to be a function of θ like $h = t\cos\theta$, the q-term could be integrated to a constant and the profiles would not depend on q. However, unlike their counterparts at edges, h and θ are independent near $x = 0$, where calculations show that the vertical mid-wall profile satisfies $h \gg t\cos\theta$; thus, the membrane structures depend slightly on q (Fig. 3.6c). This independence arises from the angle-dependent coupling strength of F_{rod}, whose integrand contains a factor of $\cos\theta$ (Eq. 3.2.5). Away from the middle of the wall, $\cos\theta \approx 1$ and deviations from $h = t\cos\theta + b_0$ are costly for F_{rod}. As $\cos\theta$ approaches 0, these deviations cost less energy in F_{rod}, so other terms such as F_{dep} (Eq. 3.2.4 without the boundary term) gain influence on the profile configuration. The competition between F_{rod}, which prefers h to decrease with $\cos\theta$ towards the middle of the wall, and F_{dep}, which prefers a constant h, sets the mid-wall thickness.

3.3 Membrane edge thermodynamics

3.3.1 Thermal ripple fluctuations

With detailed understanding of the membrane's edge structure, we next study its fluctuations, which are clearly visible and easily quantified with optical microscopy (Fig. 3.1d). In the large membrane limit, we ignore curvature of the edge and, with Cartesian coordinates, place the very edge at $x = 0$ (Fig. 3.8a). θ is now the twist angle about the x-axis. We minimize the free energy over $h(x)$ and $\theta(x)$ to obtain the profile for the unperturbed membrane edge. We then introduce a small edge ripple $u(y)$ with corresponding tangent angle $\alpha(y) \equiv \partial_y u(y)$ (Fig. 3.8a). The unperturbed configuration along lines parallel to the y-axis is mapped onto curves with the same tangent angle $\alpha(y)$, and the rod rotation axis

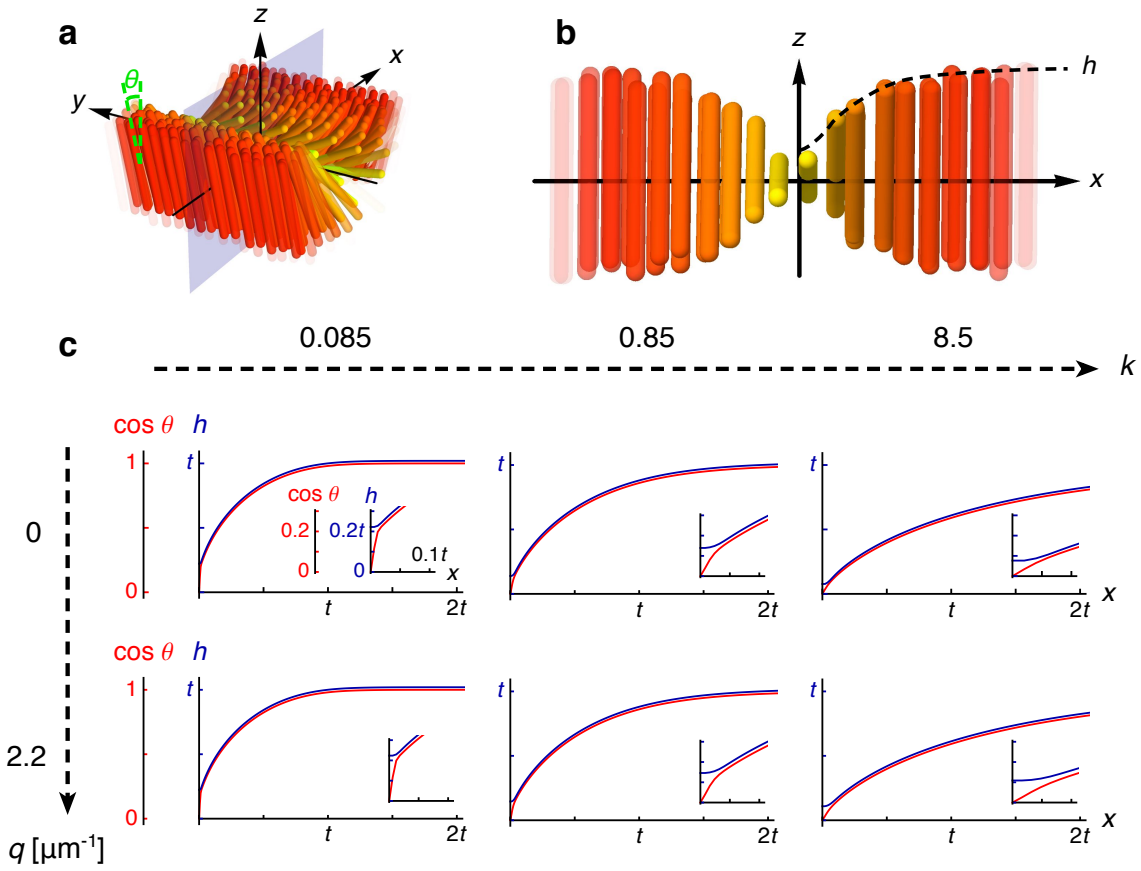

Figure 3.6: Vertical π-wall profiles and their dependence on Frank elasticity and chirality. (a) Perspective and (b) cross-section schematics showing parametrization of π-wall profile and Cartesian coordinate system. (b) shows rods that intersect the light blue plane in (a). h is the membrane half-thickness and θ is the rod tilt angle. t is the half-length of the rods. (c) Calculated vertical π-wall profiles for various Frank-to-depletion ratios k from left to right and preferred twist wavenumbers q from top to bottom. In all cases, h (blue) is almost indistinguishable from $t\cos\theta$ ($\cos\theta$ in red) away from $x = 0$. Near $x = 0$, h approaches a finite mid-wall value while $\cos\theta$ approaches 0. Insets highlight the profile near $x = 0$. Experimental conditions listed in Table 3.1 are closest to $k = 0.85$ and $q = 2.2\,\mu\text{m}^{-1}$.

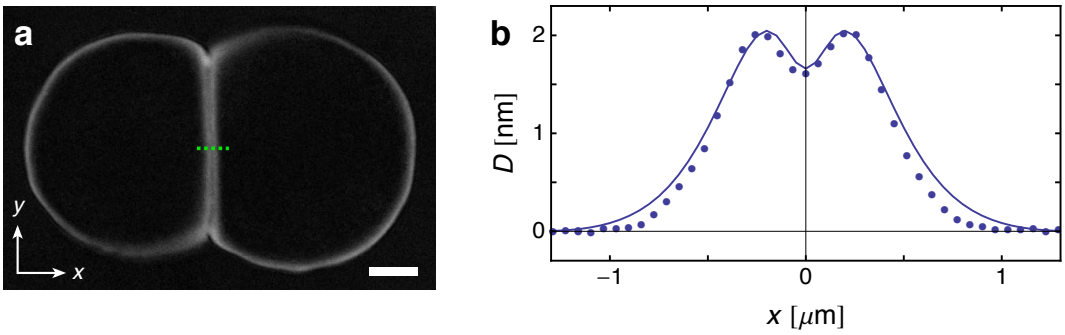

Figure 3.7: π-wall retardance. (a) 2D LC-PolScope birefringence map of two circular membranes joined through a π-wall with retardance represented as pixel brightness. The dotted green line approximately corresponds to the range of x's plotted in (b). Scale bar, 4 µm. (b) Retardance values D. The points indicate experimental data at temperature $T = 22\,^{\circ}\mathrm{C}$ and depletant concentration $n = 45\,\mathrm{mg\,mL^{-1}}$. The lines indicate theoretical results calculated with these parameter values and those described in Table 3.1. Experimental data and methods reported in Ref. [84].

for θ is always perpendicular to these curves. Mathematically, the edge profile becomes $h(x, y) = h(x - u(y))$ and the nematic director changes from $\mathbf{n}(x) = \sin\theta(x)\hat{\mathbf{y}} + \cos\theta(x)\hat{\mathbf{z}}$ to $\mathbf{n}(x, y) = \sin\alpha(y)\sin[\theta(x - u(y))]\hat{\mathbf{x}} + \cos\alpha(y)\sin[\theta(x - u(y))]\hat{\mathbf{y}} + \cos[\theta(x - u(y))]\hat{\mathbf{z}}$. We have to rederive the depletion and Frank terms in Eq. 3.2.7 to allow for gradient terms in the y-direction (expression not shown here).

We expand the ripple tangent angle in Fourier components α_p:

$$\alpha(y) = \sum_p \sqrt{\frac{2}{L_y}}\alpha_p \cos py. \tag{3.3.1}$$

p is the ripple wavenumber [89]. With the help of $\alpha_p = pu_p$, where u_p's are Fourier components for $u(y)$, we can write the free energy in terms of the small α_p's. The free energy relative to the state without ripples becomes

$$\frac{\Delta F}{L_y} = \frac{1}{2}\sum_p \left(\gamma[h, \theta] + \kappa[h, \theta]p^2\right)\alpha_p^2 + \mathcal{O}(\{\alpha_p\}^4), \tag{3.3.2}$$

which describes a 1D interface with effective line tension γ and line bending modulus κ.

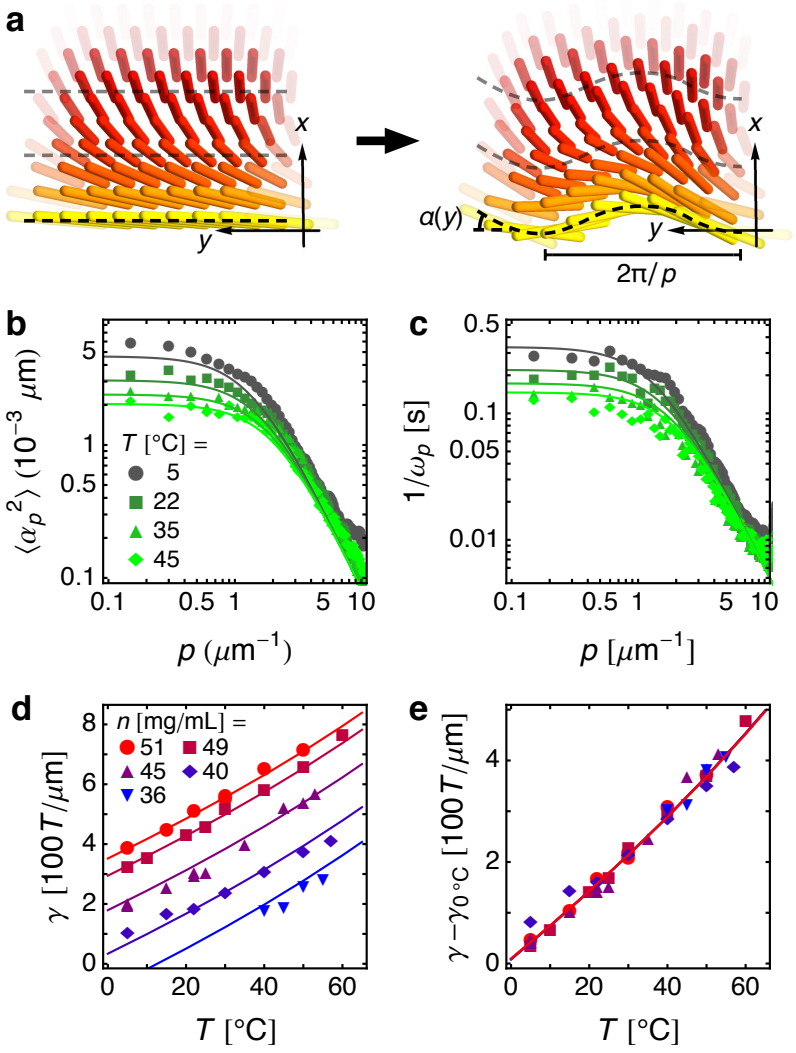

Figure 3.8: Line tension analysis of the membrane edge. The points indicate experimental data at various temperatures T and depletant concentrations n. The lines indicate theoretical results calculated for corresponding parameter values and those described in Table 3.1. (a) Schematic of the membrane ripple ansatz through which line tension and line bending modulus are calculated. $\alpha(y)$ is the angle between the ripple tangent vector and the y-axis. (b) Thermal fluctuation amplitudes $\langle \alpha_p^2 \rangle$ and (c) autocorrelation decay timescales $1/\omega_p$ of ripple fluctuations for depleting concentration $n = 45\,\mathrm{mg\,mL^{-1}}$ and various temperatures T. The theoretical plots of $1/\omega_p$ use the fit value for the 1D membrane edge viscosity $\eta_{1D} = 300\,\mathrm{mPa\,s\,\mu m^2}$. (d) Line tension γ and (e) its relative temperature-dependent behavior as a function of temperature for various n. For each n, $\gamma_{0\,^\circ\mathrm{C}}$ is the line tension extrapolated to $T = 0\,^\circ\mathrm{C}$. Experimental data and methods reported in Ref. [84].

They are given by

$$\gamma[h,\theta] = 2naT\left[\int_0^{L_x} \mathrm{d}x \frac{(\partial_x h)^2}{\sqrt{1+(\partial_x h)^2}} + h(0)\right] + 2K\int_0^{L_x} \mathrm{d}x\, h\left[(\partial_x\theta)^2 + q\partial_x\theta\right], \quad (3.3.3)$$

$$\kappa[h,\theta] = 2K\int_0^{L_x} \mathrm{d}x\, h\sin^2\theta. \quad (3.3.4)$$

At thermal equilibrium, the ripple tangent angle components take the equipartition values

$$\left\langle \alpha_p^2 \right\rangle = \frac{T}{\gamma + \kappa p^2}. \quad (3.3.5)$$

To investigate the dynamics of ripple fluctuations, we view the membrane edge as an effective 1D viscous fluid described by the ripple profile $u(y,t)$, which can vary with time. We estimate the Reynolds number of this motion to be very small $\sim 10^{-6}$–10^{-4}, so the ripple velocity $v = \partial_t u$ obeys overdamped 1D hydrodynamics:

$$-\eta_{1\mathrm{D}}\partial_y^2 v = f_{\mathrm{ext}} = f_{\mathrm{drag}}[v] - \frac{\delta\mathcal{H}_T}{\delta u}. \quad (3.3.6)$$

$\eta_{1\mathrm{D}}$ is the 1D edge viscosity and $f_{\mathrm{drag}}[v]$ is the viscous drag force per unit length arising from membrane edge motion relative to the bulk solvent [6]. We believe that the membrane has much higher viscosity than the solvent, so dissipation of ripple excitations occurs mainly through the membrane. Thus, f_{drag} can be ignored, a claim later self-consistently supported by an experimental estimate of the membrane viscosity. For similar reasons, we ignore friction with the polymer brush substrate, which behaves like an extension of the fluid phase. Using $\mathcal{H}_T = \Delta F/L_y - \sum_p f_p u_p$ for the total Hamiltonian density, where $\Delta F/L_y$ is given by Eq. 3.3.2 and the f_p's are an external field formally included to calculate the response function, we obtain:

$$\eta_{1\mathrm{D}} p^2 \partial_t u_p = -\left(\gamma p^2 + \kappa p^4\right) u_p + f_p.$$

This leads to the response function

$$\chi^{-1}_{u_p u_p}(\omega) = \frac{\partial f_p(\omega)}{\partial u_p(\omega)} = -\mathrm{i}\omega\eta_{1\mathrm{D}}p^2 + \gamma p^2 + \kappa p^4.$$

The fluctuation-dissipation theorem gives the autocorrelation function:

$$S_{u_p u_p}(\omega) = \frac{2T}{\omega}\,\mathrm{Im}\,\chi_{u_p u_p} = \frac{2T}{\eta_{1\mathrm{D}}p^2}\frac{1}{\omega^2 + {\omega_p}^2},$$

where

$$\omega_p \equiv \frac{\gamma + \kappa p^2}{\eta_{1\mathrm{D}}} \tag{3.3.7}$$

is the autocorrelation decay rate. Indeed, temporal ripple angle autocorrelations are given by

$$\langle \alpha_p(t)\alpha_p(0)\rangle = \int \frac{\mathrm{d}\omega}{2\pi}\mathrm{e}^{\mathrm{i}\omega t}p^2 S_{u_p u_p}(\omega) = \left\langle \alpha_p^2 \right\rangle \mathrm{e}^{-\omega_p t}, \tag{3.3.8}$$

with $\langle \alpha_p^2 \rangle$ in Eq. 3.3.5.

Using the fit values in Table 3.1 describing the membrane edge, our theoretical model predicts values for γ and κ, which determine the fluctuation spectra $\langle \alpha_p^2 \rangle$ and $1/\omega_p$. These predictions can be tested experimentally, and the value of γ can be extracted from the low-p limit of $\langle \alpha_p^2 \rangle$. The experimental and theoretical spectra match well over a variety of temperatures (Figs. 3.8b and c). These calculations still assume $h = t\cos\theta$, since Fig. 3.4c demonstrates that rod fluctuations b are insignificant for membrane edges. The ratio between $1/\omega_p$ and $\langle \alpha_p^2 \rangle$ appears constant for all measured values of p—in agreement with our theory—and gives a value for $\eta_{1\mathrm{D}} \approx 300\,\mathrm{mPa\,s\,\mu m^2}$.

We expect the 3D membrane viscosity η to be strongly inhomogeneous and anisotropic at the edge due to the large aspect ratio of the rods. For instance, during a ripple fluctuation, rods oriented more vertically may slide past each other more easily than those tilted more horizontally. To roughly estimate the magnitude of η, we write $\eta_{1\mathrm{D}} \sim \int \mathrm{d}x\,\mathrm{d}z\,\eta \sim A\eta$, where $A \sim 2tl_{\mathrm{twist}} \sim 2t^2$ is an estimated cross-sectional area of the membrane edge participating in these ripple fluctuations. $l_{\mathrm{twist}} \approx \sqrt{k}t$ is the twist penetration depth (Eq. 3.2.11), and

the parameter values provided in Table 3.1 satisfy $k \sim 1$. This gives $\eta \sim 800\,\mathrm{mPa\,s}$, much greater than the solvent viscosity, which is $\eta_s \approx 3\,\mathrm{mPa\,s}$ for 5 w% 500 kDa aqueous dextran [103].

Measurements and calculations of the line tension γ show good quantitative agreement over a variety of temperatures T and depletant concentrations n (Fig. 3.8d). For all n, γ decreases as T is reduced. If we measure γ relative to its value at a standard temperature, say $T = 0\,^\circ\mathrm{C}$, the line tensions for different n all collapse onto a single curve (Fig. 3.8e), indicating that the relative effect of temperature change on γ is independent of the depletant concentration. This effect is largely mediated by the variation of $q(T)$ with temperature. Colloidal membranes assembled from chiral rods are inherently frustrated, because the particles cannot simultaneously twist locally and assemble into a monolayer globally. Consequently, twist is expelled from the membrane interior and localized to its edges. Note that $q(T)$ is a monotonically decreasing function of T (Table 3.1). Decreasing the temperature increases $q(T)$ and lowers the free energy of edge-bound twisted rods (demonstrated explicitly in Eq. 3.3.3, where $\partial_x\theta$ is negative), leading to chiral control of edge line tension [89].

3.3.2 The starfish transition

When circular membranes are subjected to a temperature quench, the line tension decreases significantly and fluctuations at the edge increase in amplitude. For sufficiently low T, the circular membrane becomes unstable and grows arms of twisted ribbons along its entire periphery (Fig. 3.1e). In our model, these starfish arms arise from the aforementioned ripple fluctuations (Fig. 3.9a). As the temperature decreases, the chiral wavenumber $q(T)$ increases and lowers the line tension γ. For sufficiently large q, γ becomes negative and long-wavelength ripple modes along the membrane circumference become unstable, which presumably grow and twist into starfish arms. Again, the term proportional to the chiral twist wavenumber q in Eq. 3.3.3 is negative since $\partial_x\theta < 0$. All the other terms are positive-definite, so this term must be responsible for the line tension becoming negative at low

temperatures, leading to the starfish instability. It is analogous to the chiral line tension term in the theory of Langmuir-Blodgett films, which if sufficiently negative, can drive an instability transition from a circular film to one with similarly extended arms [91].

Figure 3.9b plots the range of unstable wavenumbers p, measured around the circumference, as a function of chiral wavenumber q for constant $k = 0.85$. Above a critical $q_c \approx 3\,\mu\text{m}^{-1}$, low-$p$ modes become unstable. An instability with $p \approx 1\,\mu\text{m}^{-1}$ in a membrane of radius $R \approx 5\,\mu\text{m}$ corresponds to a five-armed starfish structure as depicted in Figs. 3.1e and 3.9a, so the order of magnitude of unstable p's calculated in Fig. 3.9b follows expectations. Note that changing the temperature also changes $k(T)$, but the effect is qualitatively insignificant. The transition from a circular membrane to a starfish structure is reversible, so reheating to a positive γ drives the edge-length-maximizing starfish structure to decrease its edge length and become circular again [89].

3.4 Membrane rafts

3.4.1 Phase separation between virus species

Now we turn our attention to two-component membranes composed of *fd*-Y21M and M13KO7 viruses, which respectively have half-lengths t and $t + d$. Although they can be conceptualized as stiff rods and their contour lengths are known, these contour lengths (0.88 µm and 1.2 µm respectively) are close enough to their persistence lengths (9.9 µm and 2.8 µm respectively) to prevent precise determination of their end-to-end lengths [81]. Thus, we will treat the half-length difference d as a free parameter since it is important to the behavior of our system.

We start by investigating the separation of the viruses into two phases. The structure of the phases, including the number and size of rafts present, does not yet concern us. We assume a large membrane of radius R_t and ignore edge effects (Fig. 3.10a). First consider complete phase separation between the *fd*-Y21M and M13KO7 viruses. The *fd*-Y21M phase occupies an area fraction $\alpha^2 = \alpha_\text{t}^2$ equal to the proportion of *fd*-Y21M viruses experimentally

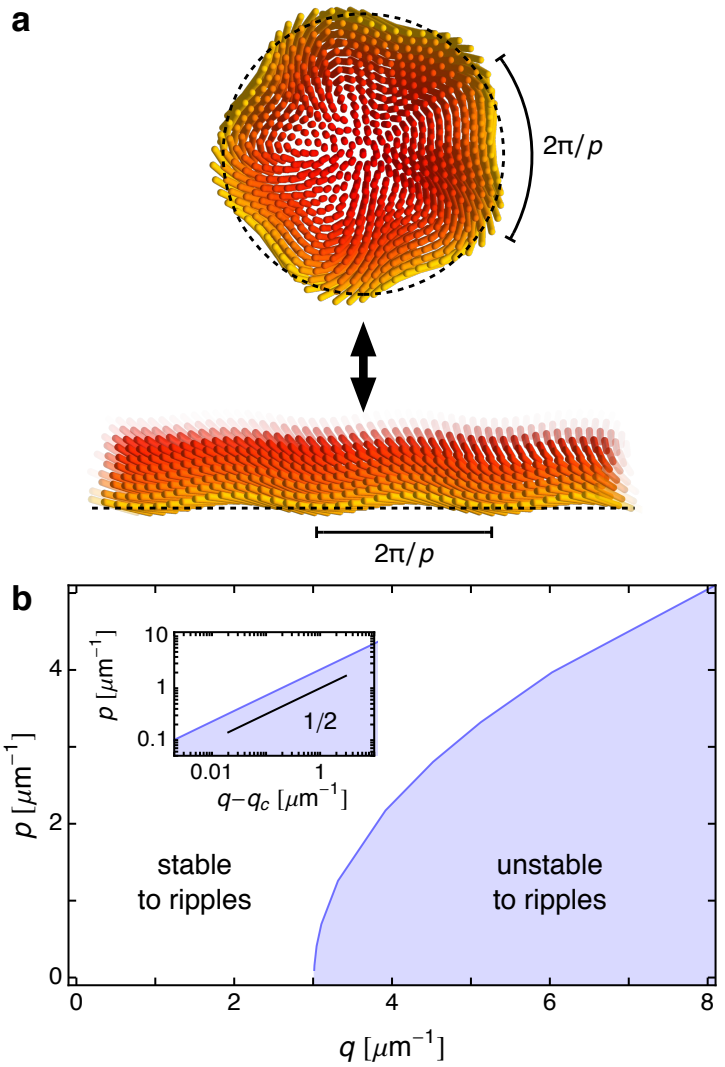

Figure 3.9: Starfish instability transition for large membranes. (a) Starfish arms grow from unstable ripple fluctuations in our theory. For large membranes, we can take the Cartesian limit and ignore the curvature of the edge. (b) The shaded region indicates unstable ripple wavenumbers p calculated for preferred twist wavenumbers q and constant Frank-to-depletion ratio $k = 0.85$. We take p to be continuous, corresponding to the infinite membrane size limit; for finite-sized circular membranes, continuity permits only certain values of p, namely multiples of the inverse radius. The inset plots the same results on a log-log scale to demonstrate that as q increases past a critical $q_c \approx 3\,\mu\text{m}^{-1}$, the range of unstable p's grows as a power law with exponent $1/2$.

provided in the virus mixture; equivalently, if it formed a single circular domain, it would have radius $\alpha_t R_t$. Some *fd*-Y21M viruses can then enter into the M13KO7 phase, reducing the area fraction of the pure *fd*-Y21M phase to $\alpha^2 < \alpha_t^2$. This means that a membrane area fraction of $\alpha_t^2 - \alpha^2$ *fd*-Y21M viruses mixes with a membrane area fraction of $1 - \alpha_t^2$ of M13KO7 viruses. In this case, the entropy of mixing would be

$$S_{\text{mix}} = \phi_{\text{Y21M}} \log \phi_{\text{Y21M}} + (1 - \phi_{\text{Y21M}}) \log(1 - \phi_{\text{Y21M}}), \tag{3.4.1}$$

where

$$\phi_{\text{Y21M}} = \frac{\alpha_t^2 - \alpha^2}{1 - \alpha^2}. \tag{3.4.2}$$

When the pure *fd*-Y21M phase disappears with $\alpha^2 = 0$, complete mixing has occured.

Note that introducing the longer M13KO7 viruses into the *fd*-Y21M-only phase is strongly disfavored by the depletants. Their surface protrusions would be surrounded by extra excluded volume of order da^2 per rod, unlike the smaller amount of excluded volume of order $d(\xi/2)^2$ per rod required to introduce shorter *fd*-Y21M viruses into the M13KO7-rich phase. $a = 31\,\text{nm}$ is the depletant radius and $\xi = 12\,\text{nm}$ is the nearest-neighbor virus separation (Table 3.1). The asymmetric effects of surface convexity and concavity on the depletion free energy, and perhaps on translational entropy, preferentially creates a pure *fd*-Y21M phase.

The degree of phase separation is entropically determined by a competition between the entropy of mixing and the depletion free energy. The entropy of mixing (Eqs. 3.4.1 and 3.4.2) resists phase separation, but sequestering the shorter *fd*-Y21M viruses into a separate phase decreases the volume excluded to depletants (Fig. 3.10b). These effects contribute to the free energy

$$\frac{F_{\text{sep}}}{\pi R_t^2 T} = \left[(1 - \alpha_t^2) \log \frac{1 - \alpha_t^2}{1 - \alpha^2} + (\alpha_t^2 - \alpha^2) \log \frac{\alpha_t^2 - \alpha^2}{1 - \alpha^2} \right] n_{\text{virus}} + 2(\alpha_t^2 - \alpha^2) nd, \tag{3.4.3}$$

where n is the 3D depletant concentration and n_{virus} is the 2D virus concentration in the

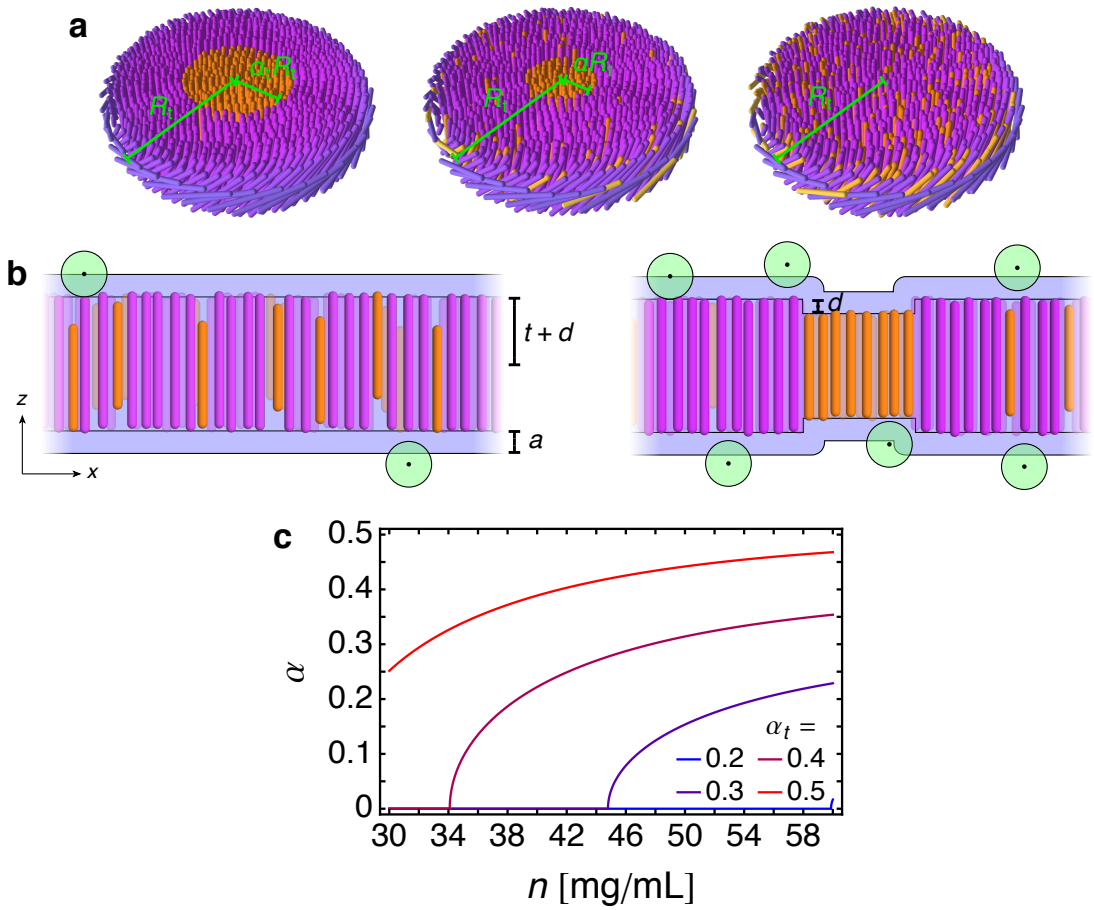

Figure 3.10: Membrane separation into two phases, one containing only *fd*-Y21M (orange) virus and the other containing both *fd*-Y21M and M13KO7 (purple) viruses. (a) Schematics of membranes with different degrees of phase separation as quantified by α. For a completely phase-separated membrane (left), the membrane area fraction of the *fd*-Y21M phase is $\alpha^2 = \alpha_t^2$; equivalently, if the *fd*-Y21M-only phase formed a single circular domain as depicted, it would have radius $\alpha_t R_t$. As *fd*-Y21M viruses enter into the M13KO7-rich phase (middle), the membrane area fraction of the *fd*-Y21M phase decreases to $\alpha^2 < \alpha_t^2$. For a completely mixed membrane (right), $\alpha^2 = 0$. (b) Competition between the entropy of mixing and depletant entropy determines α. Green circles represent depletants and blue regions represent the excluded volume. At low depletant concentration (left), the mixed state is preferred. Phase separation reduces the excluded volume and is preferred at high depletant concentration (right). (c) Preferred amount of phase separation α (Eq. 3.4.4) for various α_t and depletant concentrations n using the membrane virus concentration $n_{\text{virus}} = 5500\,\mu\text{m}^{-2}$.

membrane. We ignore other effects, such as the increased translational entropy of these shorter *fd*-Y21M viruses when they are embedded within the longer M13KO7 viruses, which may be complicated by the different chiralities and persistence lengths of the two species. We minimize this free energy over α to obtain

$$\alpha = \begin{cases} \sqrt{\dfrac{\alpha_t^2 - e^{-2nd/n_{virus}}}{1 - e^{-2nd/n_{virus}}}} & nd/n_{virus} \geq \log 1/\alpha_t \\ 0 & nd/n_{virus} \leq \log 1/\alpha_t. \end{cases} \tag{3.4.4}$$

In Fig. 3.10c, $\alpha(n)$ is plotted for various α_t's using $d = 0.12\,\mu m$ (Table 3.2) and $n_{virus} = 5500\,\mu m^{-2}$, which is consistent with the nearest-neighbor virus separation distance ξ measured in single-component *fd*-wt membranes (Table 3.1). For each α_t, there is complete mixing ($\alpha = 0$) below a critical depletant concentration $(n_{virus}/d)\log 1/\alpha_t$. Above this critical n, the system is partially phase-separated and approaches complete phase separation for $n \to \infty$. This behavior qualitatively agrees with experimental results in Figs. 3.2b–d. This analysis ignores the structure of rafts formed by the *fd*-Y21M phase. We have also tried incorporating the free energy associated with raft structure to be discussed in the next subsection; numerical energy minimization of the combined free energy yields results identical to Fig. 3.10c.

3.4.2 Raft structure

Assuming we are in the regime $nd/n_{virus} > \log 1/\alpha_t$ in which rafts exist, we analyze their structure. Eq. 3.4.4 determines the total amount of *fd*-Y21M viruses sequestered into a separate phase, but do they form a single large raft or several smaller rafts (Fig. 3.11a)? And how do the rods twist in rafts and in the background membrane, the part of tiling domains outside of rafts? To answer these questions, we need to derive their free energy.

We take the large two-component membrane of radius R_t to be approximately tiled by repeated circular domains of radius R (Fig. 3.11b). Another theory that approximately tiles space using circular or spherical unit cells is the muffin-tin approximation of solid

Table 3.2: Membrane raft parameters and their values.

Parameter	Variable	Experimental value	Reference(s)	Theoretical fit value
Temperature	T	22 °C	[79]	same
Dextran concentration	n	40 mg mL^{-1}	[79]	same
Dextran radius	a	∼25 nm	[99–101][1]	31 nm
fd-Y21M half-length	t	≈440 nm	[79][2]	440 nm
M13KO7 half-length	$t + d$	≈600 nm	[79][2]	560 nm
fd-Y21M Frank constant	K_{Y21M}	0.5 pN	[83][3,4]	2.7 pN
M13KO7 Frank constant	K_{M13}	1.1 pN	[104][4]	3.4 pN
fd-Y21M twist wavenumber	q_{Y21M}	0.02 µm^{-1}	[81][4]	0.2 µm^{-1}
M13KO7 twist wavenumber	q_{M13}	−0.1 µm^{-1}	[104][4]	−1.0 µm^{-1}
fd-Y21M birefringence	Δn_{Y21M}	0.0087	[88][3,5]	0.0065
M13KO7 birefringence	Δn_{M13}	0.0087	[88][3,5]	0.0050

[1] Hydrodynamic radii for dilute solutions of 500 kDa dextran, whereas our experiments are in the semidilute regime.
[2] Contour length which is longer than the end-to-end length desired for this parameter.
[3] Measured for *fd*-wt virus.
[4] Measured in the bulk cholesteric phase with virus concentration 50 mg mL^{-1}, which is lower than the membrane virus concentration 230 mg mL^{-1} estimated from the experimentally-measured nearest-neighbor virus distance ξ in Table 3.1.
[5] Assuming that the membrane nematic order parameter is 1. Membrane virus concentration 230 mg mL^{-1} estimated from the experimentally-measured nearest-neighbor virus distance ξ in Table 3.1.

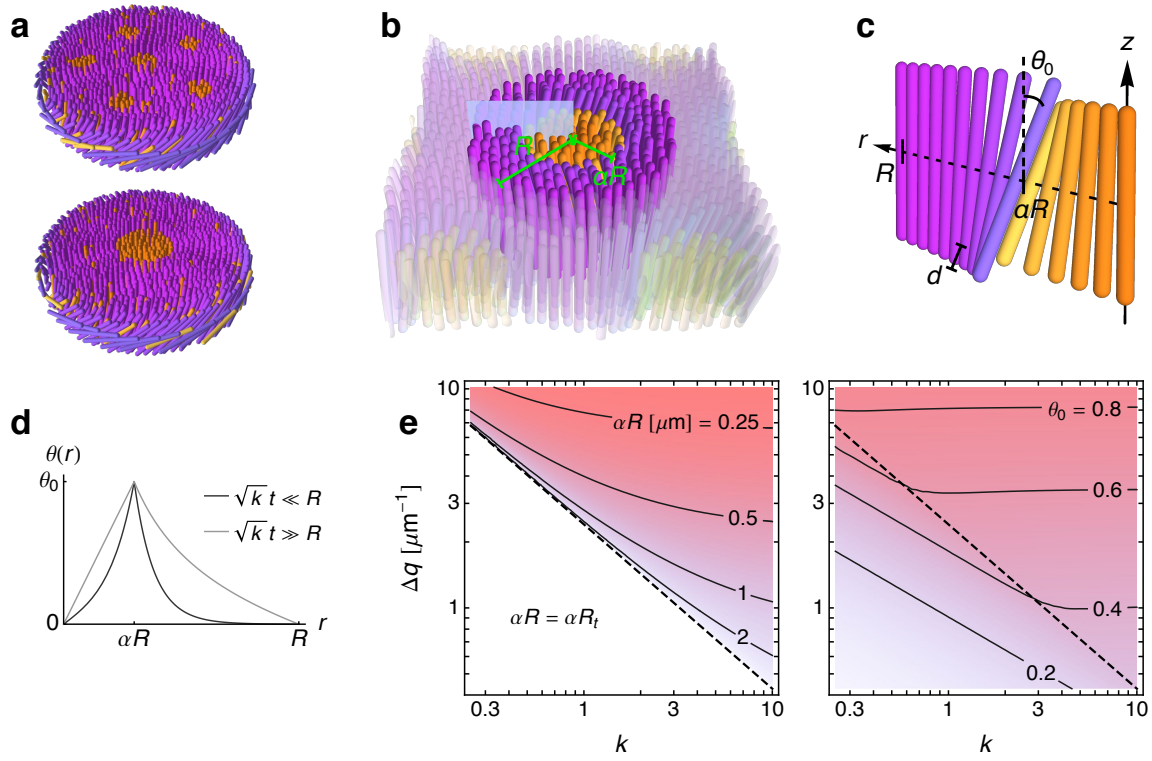

Figure 3.11: The structure of membrane rafts, including their size and their twist behavior. (a) Schematics of two membranes with the same area fraction of rafts α^2 with either many smaller rafts (top) or one larger raft (bottom). (b) Schematic of a single circular domain that is repeated to approximately tile the membrane. Its radius is R, and it contains a circular raft of radius αR. The partially transparent rods belong to other domains in the membrane. (c) Structure of the domain along the blue plane in (b). Along the radial coordinate r, the *fd*-Y21M viruses (orange) twist from $\theta(0) = 0$ to $\theta(\alpha R) = \theta_0$ at the raft-background interface with one handedness, and the background viruses, containing mostly M13KO7 virus (purple), twist from $\theta(\alpha R) = \theta_0$ to $\theta(R) = 0$ at the domain edge, where the next domain would begin. d is the half-length difference between the two virus species. (d) Twist profile $\theta(r)$ for domains whose twist penetration depth $\sqrt{kt}$ is much less or much greater than their radius R (Eq. 3.4.13). $k \equiv k_1 = k_2$ is the common Frank-to-depletion ratio and t is the *fd*-Y21M virus half-length. (e) Preferred raft radius αR and maximum twist angle θ_0 as a function of k and the twist wavenumber difference $\Delta q \equiv q_1 - q_2$. They are calculated by minimizing Eq. 3.4.17 over R and θ_0. We assume the large membrane limit $R_\mathrm{t} \gg t$, where R_t is the membrane radius and t is the half-length of the *fd*-Y21M virus. The maximum raft radius αR_t corresponds to a membrane having only a single raft, a regime separated by dashed lines from membranes with multiple smaller rafts (Eq. 3.4.19).

state physics [105]. Each membrane domain contains one circular raft of radius αR. The *fd*-Y21M viruses point vertically at the center of the raft and twist with one handedness to their interface with the background, where they attain twist angle θ_0. The background viruses, which are mostly M13KO7 with a smaller amount of *fd*-Y21M, twist with opposite handedness from θ_0 at the interface to 0 to the domain edge, where the next domain would begin (see Fig. 3.11c with orange raft viruses and purple background viruses). We assume the rods do not twist very much, so $\theta \ll 1$, and that the difference between the rod lengths is small, so $d \ll t$. We only consider free energy terms up to quadratic order in the small quantities θ and d/t. As argued in Section 3.2.1, vertical rod fluctuations can be ignored and perfect coupling can be assumed between the membrane half- thickness h and the rod twist angle θ. This means $h = t\cos\theta$ for the rafts and $h = (t+d)\cos\theta$ for the background.

We must be careful to maintain volume conservation in this system, so let's conceptualize the raft formation process in two stages. First, the untwisted two-component membrane of radius R_t with raft area fraction α^2 is divided into untwisted tiling domains of radius R that each contain a raft of radius αR (Fig. 3.11b). There are R_t^2/R^2 tiling domains and the total membrane free energy is

$$F = \frac{R_\mathrm{t}^2}{R^2} F_\mathrm{domain}, \tag{3.4.5}$$

where F_domain is the free energy of a single domain illustrated in Fig. 3.11b. Second, the rods in each of these domains can twist with angle $\theta(r) \ll 1$ (Fig. 3.11c). Doing so, however, decreases the thickness of the membrane slightly and to conserve volume in both the raft and the background, each domain has to grow slightly from radius R to R' and its raft must grow slightly from radius αR to $\alpha' R'$. Mathematically, volume conservation for the raft and the background appears respectively as

$$\int_0^{\alpha' R'} \mathrm{d}r\, rt\cos\theta = \int_0^{\alpha R} \mathrm{d}r\, rt, \qquad \int_{\alpha' R'}^{R'} \mathrm{d}r\, r(t+d)\cos\theta = \int_{\alpha R}^{R} \mathrm{d}r\, r(t+d).$$

If we expand to quadratic order in θ, we get

$$\int_0^{\alpha' R'} \mathrm{d}r\, r = \int_0^{\alpha R} \mathrm{d}r\, r + \frac{1}{2}\int_0^{\alpha' R'} \mathrm{d}r\, r\theta^2, \qquad \int_{\alpha' R'}^{R'} \mathrm{d}r\, r = \int_{\alpha R}^{R} \mathrm{d}r\, r + \frac{1}{2}\int_{\alpha' R'}^{R'} \mathrm{d}r\, r\theta^2. \quad (3.4.6)$$

Thus, the projected areas in the x-y plane of the raft and the background increase by terms proportional to θ^2 due to rod twist and volume conservation.

The free energy of the raft and the background are each described by the single-component membrane free energies F_{Frank} (Eq. 3.2.2) and F_{dep} [Eq. 3.2.4 without the boundary term proportional to $h(R)$]. We do not need the F_{rod} and Lagrange multiplier terms in Eq. 3.2.6 because we assume perfect coupling between h and θ and maintain volume conservation explicitly. In addition, the shift in membrane half-thickness by $d\cos\theta_0$ at the raft-background interface (Fig. 3.11c) creates extra excluded volume (the rounded blue regions in the right panel of Fig. 3.10b), which leads to an interfacial tension. The combination of these effects, to quadratic order in θ and d, gives

$$\begin{aligned}\frac{F_{\mathrm{domain}}}{2\pi naT} = d\alpha' R' &+ \int_0^{\alpha' R'} \mathrm{d}r \left[r + \frac{k_1 t^2}{2}\left(r(\partial_r\theta)^2 + 2\theta\partial_r\theta + \frac{\theta^2}{r} - 2q_1 r\partial_r\theta - 2q_1\theta \right)\right] \\ &+ \int_{\alpha' R'}^{R'} \mathrm{d}r \left[r + \frac{k_2 (t+d)^2}{2}\left(r(\partial_r\theta)^2 + 2\theta\partial_r\theta + \frac{\theta^2}{r} - 2q_2 r\partial_r\theta - 2q_2\theta \right)\right],\end{aligned}$$

where

$$k_1 = \frac{K_{\mathrm{Y21M}}}{natT} \qquad \text{and} \qquad q_1 = q_{\mathrm{Y21M}} \quad (3.4.7)$$

are the Frank-to-depletion ratio and the preferred twist wavenumber of the raft, which contains only *fd*-Y21M virus. The corresponding expressions for the background must account for a mixture of virus species. Experiments demonstrate that cholesteric mixtures of *fd*-wt and *fd*-Y21M viruses have intermediate twist wavenumbers that linearly interpolate between their separate values as a function of relative concentration [81]. We assume that

the same behavior applies here to Frank constants and twist wavenumbers:

$$k_2 = \frac{1-\alpha_\mathrm{t}^2}{1-\alpha^2}\frac{K_\mathrm{M13}}{na(t+d)T} + \frac{\alpha_\mathrm{t}^2-\alpha^2}{1-\alpha^2}\frac{K_\mathrm{Y21M}}{natT} \qquad \text{and} \qquad q_2 = \frac{1-\alpha_\mathrm{t}^2}{1-\alpha^2}q_\mathrm{M13} + \frac{\alpha_\mathrm{t}^2-\alpha^2}{1-\alpha^2}q_\mathrm{Y21M}. \tag{3.4.8}$$

Using $2\theta\partial_r\theta = \partial_r(\theta^2)$, $r\partial_r\theta+\theta = \partial_r(r\theta)$, and Eqs. 3.4.6, the domain free energy becomes

$$\begin{aligned}\frac{F_\mathrm{domain}}{2\pi naT} = \frac{1}{2}R^2 + d\alpha' R' - \left[k_1 q_1 t^2 - k_2 q_2 (t+d)^2\right]\alpha' R'\theta_0 \\ + \int_0^{\alpha' R'} \mathrm{d}r \left[\frac{1}{2}r\theta^2 + \frac{k_1 t^2}{2}\left(r(\partial_r\theta)^2 + \frac{\theta^2}{r}\right)\right] + \frac{k_1 t^2}{2}\theta_0^2 \\ + \int_{\alpha' R'}^{R'} \mathrm{d}r \left[\frac{1}{2}r\theta^2 + \frac{k_2 (t+d)^2}{2}\left(r(\partial_r\theta)^2 + \frac{\theta^2}{r}\right)\right] + \frac{k_2 (t+d)^2}{2}\theta_0^2.\end{aligned}$$

Every term with $\alpha' R'$ and R' is either linear or quadratic in d and θ, so to quadratic order, we can use αR and R instead:

$$\begin{aligned}\frac{F_\mathrm{domain}}{2\pi naT} = \frac{1}{2}R^2 + d\alpha R - \left[k_1 q_1 t^2 - k_2 q_2 (t+d)^2\right]\alpha R\theta_0 \\ + \int_0^{\alpha R} \mathrm{d}r \left[\frac{1}{2}r\theta^2 + \frac{k_1 t^2}{2}\left(r(\partial_r\theta)^2 + \frac{\theta^2}{r}\right)\right] + \frac{k_1 t^2}{2}\theta_0^2 \\ + \int_{\alpha R}^{R} \mathrm{d}r \left[\frac{1}{2}r\theta^2 + \frac{k_2 (t+d)^2}{2}\left(r(\partial_r\theta)^2 + \frac{\theta^2}{r}\right)\right] + \frac{k_2 (t+d)^2}{2}\theta_0^2.\end{aligned} \tag{3.4.9}$$

To be precise, the radii αR and R in Fig. 3.11 should actually be their primed counterparts, but this correction is quadratic in θ and thus small. Note that the chiral terms containing q_1 and q_2 in Eq. 3.4.9 have opposite signs because the raft rods and the background rods twist with opposite handednesses. The free energy of the membrane (Eq. 3.4.5), without a constant term proportional to R_t^2, is

$$\begin{aligned}\frac{F}{2\pi naT} = \frac{R_\mathrm{t}^2}{R^2}\Bigg\{d\alpha R - \left[k_1 q_1 t^2 - k_2 q_2 (t+d)^2\right]\alpha R\theta_0 \\ + \int_0^{\alpha R} \mathrm{d}r \left[\frac{1}{2}r\theta^2 + \frac{k_1 t^2}{2}\left(r(\partial_r\theta)^2 + \frac{\theta^2}{r}\right)\right] + \frac{k_1 t^2}{2}\theta_0^2 \\ + \int_{\alpha R}^{R} \mathrm{d}r \left[\frac{1}{2}r\theta^2 + \frac{k_2 (t+d)^2}{2}\left(r(\partial_r\theta)^2 + \frac{\theta^2}{r}\right)\right] + \frac{k_2 (t+d)^2}{2}\theta_0^2\Bigg\}.\end{aligned} \tag{3.4.10}$$

The free parameters are $\theta(r)$, including θ_0, and R. We first determine $\theta(r)$. We can write the raft integral in a dimensionless manner and solve its Euler-Lagrange equations with the substitutions $s_1 = r/\sqrt{k_1}t$ and $S_1 = R/\sqrt{k_1}t$:

$$\begin{aligned}\int_0^{\alpha R} \mathrm{d}r \left[\frac{1}{2}r\theta^2 + \frac{k_1 t^2}{2}\left(r(\partial_r\theta)^2 + \frac{\theta^2}{r}\right)\right] &= \frac{k_1 t^2}{2}\int_0^{\alpha S_1} \mathrm{d}s_1 \left[s_1\theta^2 + \frac{\theta^2}{s_1} + s_1(\partial_{s_1}\theta)^2\right] \\ &= \frac{k_1 t^2}{2}\int_0^{\alpha S_1} \mathrm{d}s_1 \left[s_1\theta\partial_{s_1}^2\theta + \theta\partial_{s_1}\theta + s_1(\partial_{s_1}\theta)^2\right] \\ &= \frac{k_1 t^2}{2}\left(s_1\theta\partial_{s_1}\theta\right)\Big|_{s_1=0}^{\alpha S_1}, \end{aligned} \tag{3.4.11}$$

where the last two expressions were obtained through the Euler-Lagrange equation

$$s_1^2\partial_{s_1}^2\theta + s_1\partial_{s_1}\theta - (s_1^2+1)\theta = 0, \tag{3.4.12}$$

which is a Bessel differential equation. The boundary conditions for the raft are $\theta(0) = 0$ and $\theta(\alpha S_1) = \theta_0$. We can obtain the same equation for the background with the substitutions $s_2 = r/\sqrt{k_2}(t+d)$ and $S_2 = R/\sqrt{k_2}(t+d)$, and its boundary conditions are $\theta(\alpha S_2) = \theta_0$ and $\theta(S_2) = 0$. Solving for $\theta(r)$ gives

$$\theta(r) = \begin{cases} \theta_0 \dfrac{I_1(s_1)}{I_1(\alpha S_1)} & 0 \le r \le \alpha R \\ \theta_0 \dfrac{K_1(s_2)/K_1(S_2) - I_1(s_2)/I_1(S_2)}{K_1(\alpha S_2)/K_1(S_2) - I_1(\alpha S_2)/I_1(S_2)} & \alpha R \le r \le R, \end{cases} \tag{3.4.13}$$

where I_ν and K_ν are modified Bessel functions of the first and second kind, respectively, of order ν.

We can make our analysis simpler and more meaningful by assuming that the raft and the background have the same twist lengthscales $\sqrt{k_1}t = \sqrt{k_2}(t+d) \equiv \sqrt{k}t$, where k is approximately a common Frank-to-depletion ratio shared by the two virus species. This assumption is supported by the experimental values in Table 3.2. Using this simplification, Eq. 3.4.13 is plotted in Fig. 3.11d. Generally, θ increases exponentially in the raft towards the interface to its maximum θ_0 and then decays exponentially in the background towards

the domain edge. The characteristic decay length, or twist lengthscale, is $\sqrt{k}t$; if the domain radius R is much smaller than this length, $\theta(r)$ remains in the linear regime of the exponential function throughout the domain.

We briefly abandon the equal-twist-lengthscale assumption and use Eqs. 3.4.13 and 3.4.11 to evaluate the integrals in F (Eq. 3.4.10):

$$\frac{F}{2\pi naR_{\mathrm{t}}^2T} = \frac{\alpha}{R}\Bigg\{d - \left[k_1q_1t^2 - k_2q_2(t+d)^2\right]\theta_0 + \frac{1}{2}\left[\sqrt{k_1}t\frac{I_0(\alpha S_1)}{I_1(\alpha S_1)} + \sqrt{k_2}(t+d)\frac{K_0(\alpha S_2)/K_1(S_2) + I_0(\alpha S_2)/I_1(S_2)}{K_1(\alpha S_2)/K_1(S_2) - I_1(\alpha S_2)/I_1(S_2)}\right]\theta_0^2\Bigg\}. \tag{3.4.14}$$

Minimizing over θ_0, we get

$$\theta_0 = \frac{k_1q_1t^2 - k_2q_2(t+d)^2}{\sqrt{k_1}t\frac{I_0(\alpha S_1)}{I_1(\alpha S_1)} + \sqrt{k_2}(t+d)\frac{K_0(\alpha S_2)/K_1(S_2)+I_0(\alpha S_2)/I_1(S_2)}{K_1(\alpha S_2)/K_1(S_2)-I_1(\alpha S_2)/I_1(S_2)}}, \tag{3.4.15}$$

which still depends on R through S_1 and S_2. Substituting this expression into F,

$$\frac{F}{2\pi naR_{\mathrm{t}}^2T} = \frac{\alpha}{R}\left\{d - \frac{1}{2}\frac{\left[k_1q_1t^2 - k_2q_2(t+d)^2\right]^2}{\sqrt{k_1}t\frac{I_0(\alpha S_1)}{I_1(\alpha S_1)} + \sqrt{k_2}(t+d)\frac{K_0(\alpha S_2)/K_1(S_2)+I_0(\alpha S_2)/I_1(S_2)}{K_1(\alpha S_2)/K_1(S_2)-I_1(\alpha S_2)/I_1(S_2)}}\right\}, \tag{3.4.16}$$

which only depends on the free parameter R.

Returning to the assumption $\sqrt{k_1}t = \sqrt{k_2}(t+d) \equiv \sqrt{k}t$, the free energy becomes

$$\frac{F}{2\pi naR_{\mathrm{t}}^2T} = \frac{\alpha}{R}\left\{d - \frac{1}{2}\frac{k^{3/2}\Delta q^2t^3}{\frac{I_0(\alpha S)}{I_1(\alpha S)} + \frac{K_0(\alpha S)/K_1(S)+I_0(\alpha S)/I_1(S)}{K_1(\alpha S)/K_1(S)-I_1(\alpha S)/I_1(S)}}\right\}, \tag{3.4.17}$$

where $S = R/\sqrt{k}t$ and $\Delta q = q_1 - q_2$ is the chiral twist wavenumber difference. We numerically minimize this free energy over R to obtain the preferred raft size αR and, via Eq. 3.4.15, the maximum twist angle θ_0. In Fig. 3.11e, we plot the results as functions of k and Δq for $\alpha_{\mathrm{t}} = 0.3$, $d/t = 0.28$, and large membranes $R_{\mathrm{t}} \gg t$. Let's first discuss raft size for constant k. When Δq exceeds a certain critical value, the membrane prefers to have

multiple rafts of a particular radius, as observed in Fig. 3.2e. Increasing Δq leads to more numerous, smaller rafts and thus greater total interfacial length between rafts and background. A longer interface is disfavored by the depletants but favored by the viruses when Δq is large as it faciliates the two species to twist with opposite handednesses. Now for constant Δq, increasing k—or equivalently decreasing n—leads to more numerous, smaller rafts, which qualitatively agrees with experimental observations in Figs. 3.2c and d. θ_0 is largely controlled by only Δq in the multiple-raft regime. Upon the parity transformation $\Delta q \to -\Delta q$, θ_0 would change sign and αR would not be affected.

We can investigate the transition from a single raft to multiple smaller rafts in a very large membrane of radius $R_\mathrm{t} \to \infty$, corresponding to the critical dashed line of Fig. 3.11e, by considering the $R \gg t$ limit. The free energy Eq. 3.4.17 becomes

$$\frac{F}{2\pi n a R_\mathrm{t}^2 T} \sim \frac{\alpha}{R}\left\{d - \frac{1}{4}k^{3/2}\Delta q^2 t^3 + \frac{3}{32}\frac{k^{5/2}\Delta q^2 t^5}{\alpha^2 R^2} + \frac{1}{4}k^{3/2}\Delta q^2 t^3 \mathrm{e}^{-2(1-\alpha)R/\sqrt{kt}}\right\}. \quad (3.4.18)$$

This expression is analogous to the free energy of the 2D Frenkel-Kontorova around the commensurate-incommensurate transition, with the first two terms corresponding to an effective interfacial tension of rafts, the third corresponding to three-raft interactions arising from the 2D membrane geometry, and the fourth corresponding to raft-raft repulsion [6, 106]. Note that the effective interfacial tension $d - \frac{1}{4}k^{3/2}\Delta q^2 t^3$ precisely captures the competition between depletion and virus chirality, and when it becomes negative, the system prefers multiple finite-sized rafts. Thus, the critical dashed line of Fig. 3.11e is second-order and given by

$$\Delta q = 2d^{1/2}k^{-3/4}t^{-3/2}. \quad (3.4.19)$$

To quantitatively test the validity of our model, we can compare measurements of optical retardance to those calculated in our model. Fig. 3.12a shows an LC-Polscope image of a membrane with rafts of various radii; the rafts have yet to reach their preferred size. Retardance D can be calculated in our theory using $D = 2\Delta n h \sin\theta^2$ [102]. Again, $h = t\cos\theta$ in the raft and $h = (t+d)\cos\theta$ in the background. The virus birefringences Δn_{Y21M} and

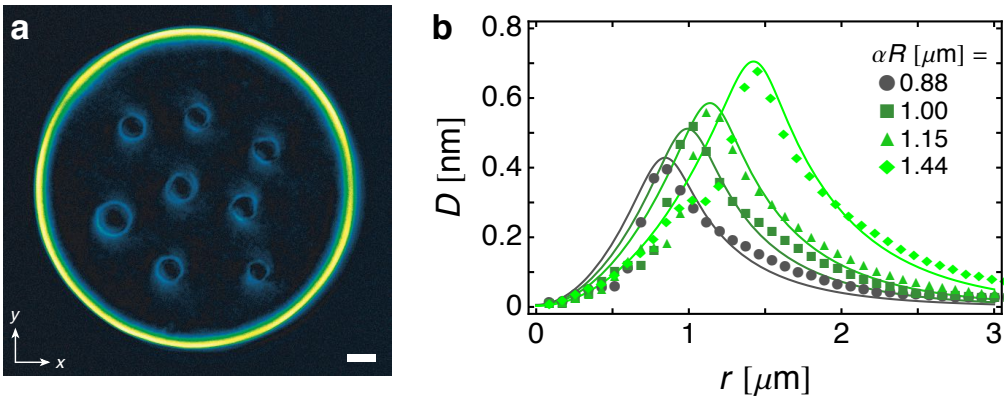

Figure 3.12: Raft retardance for rafts of different sizes. (a) 2D LC-PolScope birefringence map of a large circular membrane containing rafts of different sizes. Retardance is represented as pixel brightness. Scale bar, 2.5 µm. (b) Retardance values D for rafts of various radii αR. The points indicate experimental data at temperature $T = 22\,^{\circ}\mathrm{C}$ and depletant concentration $n = 40\,\mathrm{mg\,mL^{-1}}$. The lines indicate theoretical results calculated with these parameter values and those described in Table 3.2, giving common Frank-to-depletion ratio $k = 3$ and twist wavenumber difference $\Delta q = 1.2\,\mu\mathrm{m}^{-1}$. Experimental data and methods reported in Ref. [79].

Δn_{M13} are fit parameters, as are other parameters in Table 3.2. The raw calculated retardance profiles are convolved with a Gaussian of width 0.13 µm representing the microscope's resolution function, exactly as previously reported [88]. We generate profiles for different raft radii αR by adjusting α. Fig. 3.12b shows excellent agreement between theoretical and experimental retardance profiles. The maximum twist angle (Eq. 3.4.15) calculated with the parameter values in Table 3.2 is $\theta_0 \approx 0.35$, which, along with $d/t = 0.28$, is not quite an order of magnitude less than 1. However, our expansion of the free energy to quadratic order in θ and d/t has the benefit of mathematical tractability, which has provided deep insight into the behavior of membrane rafts, while still quantitatively matching experimental measurements with physically reasonable parameter values.

3.4.3 Raft-raft repulsion

To model the interaction between two rafts as they approach each other, we shift each circular raft within its circular tiling domain off-center by a distance b_0 towards each other (Fig. 3.13a). To accomplish this, the background membrane must be deformed. We parametrize this deformation by a shift profile $b(r)$ such that the Cartesian coordinates are

given in terms of shifted polar coordinates by

$$x = r\cos\phi + b(r) \qquad \text{and} \qquad y = r\sin\phi. \tag{3.4.20}$$

In other words, the curves of constant r are nested non-concentric circles of radius r centered at $x = b(r)$. If $b(r) = \sqrt{r^2 + \zeta^2}$ for some ζ, they would be circles of Apollonius [107]. In our system, the shift must vanish at the edge of the tiling domain where the neighboring domains begin, so $b(R) = 0$, and the shift must equal b_0 at the raft interface, so $b(\alpha R) = b_0$. See Fig. 3.13b for a schematic of this coordinate system.

This shift breaks the circular symmetry of the circular domain, so the director $\mathbf{n}$ need not be independent of ϕ. It creates a dipole moment, but no higher harmonics, so we expand θ in circular harmonics and keep only the first, dipolar term: $\theta(r, \phi) = \theta(r) + \delta\theta(r)\cos\phi$. For simplicity, we assume that the maximum twist angle at the raft-background interface does not change, so $\theta(\alpha R) = \theta_0$ and $\delta\theta(\alpha R) = 0$. This way, the raft configuration remains unchanged and all the deformation occurs in the background membrane. θ still describes rod tilt in the $\hat{\boldsymbol{\phi}}$-direction, which is still $\hat{\boldsymbol{\phi}} = -\sin\phi\,\hat{\mathbf{x}} + \cos\phi\,\hat{\mathbf{y}}$. With circular symmetry broken, there could also be tilt in the $\hat{\mathbf{r}}$-direction, but we ignore this effect in our deformation ansatz.

To calculate the free energy of the deformation, we turn to Eq. 3.4.9, which describes the free energy of one undeformed domain. Our deformation ansatz does not change R, α, θ_0, or the raft structure, so its free energy must only affect the second integral over the background, comprised of a depletion energy term due to volume conservation and the achiral terms of the Frank free energy. We must carefully recalculate these terms

$$\frac{F_{\text{def}}}{2\pi naT} = \int_{\alpha R}^{R} \mathrm{d}r \int_0^{2\pi} \frac{\mathrm{d}\phi}{2\pi} h_r h_\phi \left\{ \frac{1}{2}\theta^2 + \frac{k_2(t+d)^2}{2} \left[(\boldsymbol{\nabla}\cdot\mathbf{n})^2 + (\boldsymbol{\nabla}\times\mathbf{n})^2 \right] \right\} \tag{3.4.21}$$

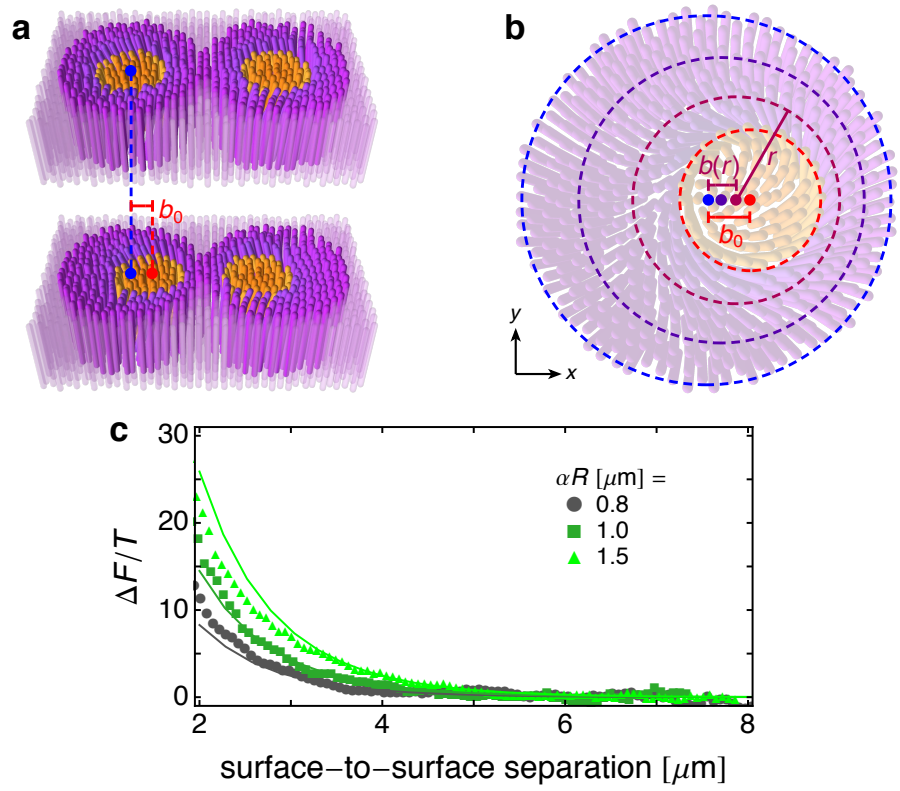

Figure 3.13: Raft-raft repulsion for rafts of different sizes. (a) Schematic depicting the approach of two rafts modeled as off-center shifts b_0 of rafts with respect to their circular tiling domains. The undeformed configuration is at the top and the shifted configuration is at the bottom. (b) Shifted polar coordinate system of the background membrane. Dashed lines indicate curves of constant r from $r = \alpha R$ (red) to $r = R$ (blue), which are circles of radius r centered at $x = b(r)$. The center of each circle is indicated with a solid dot of the same color. The off-center shift of the raft is $b(\alpha R) = b_0$. (c) Raft-raft repulsion energy ΔF for rafts of various radii αR. The points indicate experimental data at temperature $T = 22\,^{\circ}\mathrm{C}$ and depletant concentration $n = 40\,\mathrm{mg\,mL^{-1}}$. The lines indicate theoretical results calculated with these parameter values and those described in Table 3.2, giving common Frank-to-depletion ratio $k = 3$ and twist wavenumber difference $\Delta q = 1.2\,\mu\mathrm{m}^{-1}$. Experimental data and methods reported in Ref. [79].

in our coordinate system Eq. 3.4.20 using the scale factors

$$h_r = \sqrt{(\partial_r x)^2 + (\partial_r y)^2} = \sqrt{1 + 2\cos\phi\,\partial_r b + (\partial_r b)^2}, \qquad h_\phi = \sqrt{(\partial_\phi x)^2 + (\partial_\phi y)^2} = r \tag{3.4.22}$$

and the director $\mathbf{n} = \cos[\theta(r) + \delta\theta(r)\cos\phi]\hat{\boldsymbol{\phi}} + \sin[\theta(r) + \delta\theta(r)\cos\phi]\hat{\mathbf{z}}$.

We first consider only small deformations with $\partial_r b \ll 1$. Thus, the twist angle perturbation $\delta\theta \ll 1$ is also small and θ retains its undeformed profile (Eq. 3.4.13). To quadratic order in $\partial_r b$ and $\delta\theta$, Eq. 3.4.21 becomes, relative to the undeformed free energy,

$$\frac{\Delta F_{\text{def}}}{2\pi naT} = \int_{\alpha R}^{R} \mathrm{d}r \Bigg\{ \frac{1}{8}\left[2r\delta\theta^2 + r\theta^2(\partial_r b)^2\right] + \frac{k_2(t+d)^2}{8}\left[2r(\partial_r\delta\theta)^2 + 4\delta\theta\partial_r\delta\theta + 4\frac{\delta\theta^2}{r} + \left(r(\partial_r\theta)^2 + 2\theta\partial_r\theta + 3\frac{\theta^2}{r}\right)(\partial_r b)^2\right]\Bigg\}.$$

First, note that $\delta\theta$ and b are uncoupled. The terms corresponding to $\delta\theta$ can be written as a sum of squares, so $\delta\theta = 0$. Thus,

$$\frac{\Delta F_{\text{def}}}{2\pi naT} = \int_{\alpha R}^{R} \mathrm{d}r \left[\frac{1}{8}r\theta^2 + \frac{k_2(t+d)^2}{8}\left(r(\partial_r\theta)^2 + 2\theta\partial_r\theta + 3\frac{\theta^2}{r}\right)\right](\partial_r b)^2. \tag{3.4.23}$$

Its Euler-Lagrange equation immediately gives $b(r)$ in integral form. In the large radius limit where $\alpha R \gg \sqrt{k_2}t$, this integral can be evaluated to give

$$b(r) \approx b_0 \frac{\arctan\tanh[(R-r)/\sqrt{k_2}(t+d)]}{\arctan\tanh[(R-\alpha R)/\sqrt{k_2}(t+d)]}. \tag{3.4.24}$$

Substituting this into Eq. 3.4.23 yields the energy of the small deformation

$$\frac{\Delta F_{\text{def}}}{2\pi naT} \approx \frac{\sqrt{k_2}(t+d)}{8}\alpha R\theta_0^2 \frac{\operatorname{csch}^2[(R-\alpha R)/\sqrt{k_2}(t+d)]}{\arctan\tanh[(R-\alpha R)/\sqrt{k_2}(t+d)]} b_0^2. \tag{3.4.25}$$

Experiments like Fig. 3.2f, however, do not create small deformations satisfying $\partial_r b \ll 1$. To describe larger deformations, we keep $\delta\theta = 0$ for simplicity and carefully recalculate

Eq. 3.4.21 without quadratic-order expansions to obtain

$$\frac{\Delta F_{\text{def}}}{2\pi naT} = \frac{1}{2\pi}\int_{\alpha R}^{R}\frac{\mathrm{d}r}{r}\Bigg[\left(2r^2 - k_2(t+d)^2\right)\theta^2(1+\partial_r b)E\left(\tfrac{2\sqrt{\partial_r b}}{1+\partial_r b}\right) + k_2(t+d)^2\frac{2r^2(\partial_r\theta)^2 + 4r\theta\partial_r\theta + 3\theta^2 + \theta^2(\partial_r b)^2}{1+\partial_r b}K\left(\tfrac{2\sqrt{\partial_r b}}{1+\partial_r b}\right)\Bigg], \tag{3.4.26}$$

where K and E are complete elliptic integrals of the first and second kinds, respectively. For various raft shifts b_0, we can numerically solve the Euler-Lagrange equations for $\theta(r)$ and $b(r)$ via a relaxational method (Appendix A) and then calculate ΔF_{def}. We then convert ΔF_{def} as a function of b_0 to the interaction energy between two rafts ΔF, which is just twice ΔF_{def}, as a function of raft surface-to-surface separation (Fig. 3.13c). Using theoretical fit values given in Table 3.2, we obtain good agreement with experimental measurements for various raft radii αR. Thus, despite our relatively simple ansatz, our results quantitatively demonstrate that deformation of the background membrane structure as two rafts approach each other can lead to the observed repulsion between rafts.

Chapter 4

Conclusion

In achiral LC systems such as the ones we have studied, twist deformation always comes with an energetic cost. However, if it can decrease the free energy corresponding to other physical effects by a greater amount than its intrinsic cost, twist deformation will be stabilized. By tuning parameters that control the magnitude of these other effects past a critical point at which the total free energy is zero, we can see the onset of chiral twist through spontaneous symmetry breaking. In our systems, this phase transition is second-order, though it is conceivable that sponatneous chiral symmetry breaking could appear as a first-order transition in systems where the free energy has an important sixth-order term or where the order parameter is a vector or tensor [6].

Twist in chromonic LC systems described in Chapter 2 is stabilized by the energies of other deformation modes, namely bend and saddle-splay for homeotropic and degenerate planar anchoring, respectively. The magnitudes of Frank moduli govern the competition between different terms in the Frank free energy and can be adjusted by changing the temperature or the LC concentration. When these moduli become sufficiently greater than the twist modulus, the system adopts chiral configurations. On the other hand, the single-component colloidal membranes of Chapter 3 composed of a macroscopically achiral mixture of rods are induced to twist by depletion, an external agent (which, interestingly, disfavors rod tilt in the interior of the membrane). Depletant concentration is an easily tunable

parameter that drives twist of edge-bound rods at high enough depletion strength.

The presence of degenerate configurations arising from spontaneous symmetry breaking leads to domain walls and topological defects. Chromonic LCs in capillaries have degenerate twist directions under planar anchoring and degenerate twist and bend directions under homeotropic anchoring. Chiral hedgehogs and domain walls with a rich phenomenology arise between domains of different configurations. There are topological restrictions on the configuration of individual or successive domain walls and hedgehogs, but within these restrictions, the system chooses the configuration that minimizes its energy. The domain walls formed through partial coalescence of two colloidal membranes of the same handedness do not separate degenerate domains of different physical configurations. Instead, the degeneracy lies in the nematic director or polar tilt angle of the rods, whose transformations $\mathbf{n} \rightarrow -\mathbf{n}$ or $\theta \rightarrow \theta + \pi$ produce no physical effect. Indeed, the absolute signs of $\mathbf{n}$ or phases of θ for two separate membranes can be arbitrarily assigned. However, once they coalescence, their relationship is fixed by the continuous twisting that connects them. θ of one membrane must be greater by π than θ of the other, and the handedness of twist determines which one has greater θ.

Yet, handedness is more than an interesting topological property. Intrinsic chirality in LC systems such as colloidal membranes appears as a preferred twist wavenumber q and can create remarkable structures. It destabilizes the edges of circular membranes and induces a striking morphological change into starfish with twisted arms. Membrane rafts arise in mixtures of viruses of different lengths and opposite chiralities, and their size and structure are strongly dependent on the difference in q between the two virus species.

The ability of boundary conditions to dictate bulk structure is a common theme in physics and is exemplified by our LC systems. For chromonic LCs confined in capillaries, homeotropic anchoring generates bulk bend distortion that can be alleviated by twist and degenerate planar anchoring permits surface saddle-splay energy to favor bulk twist. Moreover, the cylinder radius can be scaled out of the Frank free energy in both cases, so these boundary effects will create the same scaled bulk distortion independent of capillary size.

Saddle-splay is in fact an independent distortion mode present in the bulk whose energy can be integrated to the boundary, like the twist term proportional to q in the membrane raft free energy. Although these terms do not affect the bulk Euler-Lagrange equations, they set natural boundary conditions that drive bulk chiral behaviors in their respective systems.

Chromonic LCs are organic molecules dissolved in water, so although any applications of our work are currently speculative, they would be compatible with biological systems, in which chirality plays a fundamental role. Our investigation of colloidal membranes uses generalizable principles that can qualitatively apply to systems of different scales that have the same fundamental symmetries, such as biomembranes. Instead of depletion, electrostatic interactions that favor alignment of hydrophilic and hydrophobic molecular groups assign energetic costs for phospholipid tilt in the bulk and for interface between different kinds of phospholipids. We explained in colloidal membranes how raft size is determined by a competition between preferred chiral twist and interfacial tension, and how raft-raft repulsion is mediated by structural distortions of the twisted background membrane. This suggests that chirality contributes not only biochemically but also physically to the behavior of lipid rafts in biomembranes, which provides an alternate explanation for the observed dependence of anesthetic strength on the chirality of the volatile anesthetic molecule. The mechanism of action of inhalational anesthetics remains contested after decades of investigation, but two possibilities are non-specific disruption of lipid membrane structure and specific binding to membrane ion channels, respectively representing perspectives from physical chemistry and biochemistry [108]. Recent observations that the two mirror-image enantiomers of molecularly chiral anesthetics have different anesthetic strengths rallied support for the channel-binding model, since physical membrane properties were throught to be independent of chirality [109–111]. However, our work suggests that chirality-dependent membrane raft changes can still arise from a physical process. Indeed, volatile anesthetics have been shown to disrupt lipid rafts [112, 113]—maybe they do so in a chirality-dependent way.

The importance of chirality is inescapable in aligned systems that spin or have twist.

Helicies, braids, and decorated tetrahedra abound in the living and non-living world. Understanding their properties and harnessing them for practical purposes will require an appreciation of their chiral nature.

Appendix A

Free energy functional minimization

A.1 Calculus of variations

We want to minimize the functional

$$I = \int_a^b \mathrm{d}x \; L[y, y'; x] + K[y; b], \tag{A.1.1}$$

where K is a boundary term at $x = b$, and both a and $y(a)$ are fixed. The functional's variation to first order is

$$\begin{aligned}
\delta I &= \int_a^{b+\delta b} \mathrm{d}x \; L[y + \delta y, y' + \delta y'; x] + K[y + \delta y; b + \delta b] - \int_a^b \mathrm{d}x \; L[y, y'; x] - K[y; b] \\
&= \int_a^b \mathrm{d}x \left(\frac{\partial L}{\partial y} \delta y + \frac{\partial L}{\partial y'} \delta y' \right) + L(b)\delta b + \frac{\partial K}{\partial y} \delta y(b) + \frac{\partial K}{\partial y} y'(b)\delta b + \frac{\partial K}{\partial b} \delta b \\
&= \int_a^b \mathrm{d}x \left(\frac{\partial L}{\partial y} - \partial_x \frac{\partial L}{\partial y'} \right) \delta y + \frac{\partial L}{\partial y'}(b)\delta y(b) + L(b)\delta b + \frac{\partial K}{\partial y} \delta y(b) + \frac{\partial K}{\partial y} y'(b)\delta b + \frac{\partial K}{\partial b} \delta b.
\end{aligned} \tag{A.1.2}$$

Stationarity of the functional, $\delta I = 0$, implies that the coefficient of each infinitesimal variation must be 0. Thus,

$$0 = \frac{\partial L}{\partial y} - \partial_x \frac{\partial L}{\partial y'} \quad \text{for} \quad a \leq x \leq b. \tag{A.1.3}$$

For the boundary conditions at $x = b$, we first allow both b and $y(b)$ to vary. Then,

$$\begin{aligned} 0 &= L + y' \frac{\partial K}{\partial y} + \frac{\partial K}{\partial b} \quad \text{at} \quad x = b, \\ 0 &= \frac{\partial L}{\partial y'} + \frac{\partial K}{\partial y} \qquad\quad \text{at} \quad x = b. \end{aligned} \tag{A.1.4}$$

If we fix b but allow $y(b)$ to vary, we set $\delta b = 0$ and obtain

$$0 = \frac{\partial L}{\partial y'} + \frac{\partial K}{\partial y} \quad \text{at} \quad x = b. \tag{A.1.5}$$

If we fix $y(b)$ but allow b to vary, we require the perturbed function at the perturbed endpoint to equal the unperturbed function at the unperturbed endpoint: $y(b) = y(b + \delta b) + \delta y(b + \delta b) \approx y(b) + y'(b)\delta b + \delta y(b)$. Thus, $\delta y(b) \approx -y'(b)\delta b$, so

$$0 = L - y' \frac{\partial L}{\partial y'} + \frac{\partial K}{\partial b} \quad \text{at} \quad x = b. \tag{A.1.6}$$

Meanwhile, if a and/or $y(a)$ were not fixed, and if the functional contained a boundary term $J[y; a]$, we would also get analogous boundary conditions at $x = a$ with $b \to a$, $K \to J$, and $L \to -L$ because a is the lower boundary of the integration domain.

A.2 Numerical relaxational method

Suppose we wish to minimize a free energy functional F that depends on $\alpha(r, z)$ and $\beta(r, z)$. We can solve their Euler-Lagrange equations (Eq. A.1.3) numerically. We introduce a time coordinate t on which the functions $\alpha(r, z, t)$ and $\beta(r, z, t)$ now depend. We provide initial

guesses $\alpha(r, z, 0)$ and $\beta(r, z, 0)$ use the numerical method of lines to solve

$$\partial_t \alpha = -\Gamma_\alpha \frac{\delta F}{\delta \alpha} \quad \text{and} \quad \partial_t \beta = -\Gamma_\beta \frac{\delta F}{\delta \beta}, \tag{A.2.1}$$

where $\frac{\delta F}{\delta \alpha}$ and $\frac{\delta F}{\delta \beta}$ correspond to the right-hand side of Eq. A.1.3. We do this up to some $t = t_{\max}$ when α and β do not appreciably change; $\partial_t \alpha \approx 0$ and $\partial_t \beta \approx 0$ means that the functions α and β have converged to solutions of the Euler-Lagrange equations. The Γ factors are relaxational rates.

Bibliography

[1] R. Bentley, "Chiral: A confusing etymology," Chirality (2010).

[2] C. L. Kane and E. J. Mele, "Quantum spin Hall effect in graphene," Phys. Rev. Lett. **95**, 226801 (2005).

[3] M. Z. Hasan and C. L. Kane, "Colloquium: Topological insulators," Rev. Mod. Phys. **82**, 3045–3067 (2010).

[4] A. B. Harris, R. D. Kamien, and T. C. Lubensky, "Molecular chirality and chiral parameters," Rev. Mod. Phys. **71**, 1745–1757 (1999).

[5] E. Efrati and W. T. M. Irvine, "Orientation-dependent handedness and chiral design," Phys. Rev. X **4**, 011003 (2014).

[6] P. M. Chaikin and T. C. Lubensky, *Principles of Condensed Matter Physics* (Cambridge University Press, Cambridge, 1995).

[7] P.-G. de Gennes and J. Prost, *The Physics of Liquid Crystals*, 2nd ed., The International Series of Monographs on Physics (Clarendon Press, Oxford, 1993).

[8] F. Reinitzer, "Beiträge zur Kenntniss des Cholesterins," Monatsh Chem **9**, 421–441 (1888).

[9] G. H. Brown and J. J. Wolken, *Liquid Crystals and Biological Structures* (Academic Press, New York, 1979).

[10] P. J. Collings, *Liquid Crystals: Nature's Delicate Phase of Matter*, 2nd ed. (Princeton University Press, Princeton, 2002).

[11] F. Livolant, "Ordered phases of DNA in vivo and in vitro," Phys. A **176**, 117–137 (1991).

[12] G. Weerts, "3D gets second look," SPIE Professional (2012).

[13] T. Ohzono, T. Yamamoto, and J.-i. Fukuda, "A liquid crystalline chirality balance for vapours," Nat. Commun. **5** (2014).

[14] F. C. Frank, "I. Liquid crystals. On the theory of liquid crystals," Discuss. Faraday Soc. **25**, 19–28 (1958).

[15] E. G. Virga, *Variational Theories for Liquid Crystals* (Chapman and Hall, London, 1994).

[16] M. J. Press and A. S. Arrott, "Theory and experiments on configurations with cylindrical symmetry in liquid-crystal droplets," Phys. Rev. Lett. **33**, 403–406 (1974).

[17] O. D. Lavrentovich and E. M. Terent'ev, "Phase transition altering the symmetry of topological point defects (hedgehogs) in a nematic liquid crystal," Sov. Phys. JETP **64**, 1237–1244 (1986).

[18] P. S. Drzaic, "A case of mistaken identity: Spontaneous formation of twisted bipolar droplets from achiral nematic materials," Liq. Cryst. **26**, 623–627 (1999).

[19] J. Jeong, Z. S. Davidson, P. J. Collings, T. C. Lubensky, and A. G. Yodh, "Chiral symmetry breaking and surface faceting in chromonic liquid crystal droplets with giant elastic anisotropy." Proc. Natl. Acad. Sci. U. S. A. **111**, 1742–1747 (2014).

[20] P. Prinsen and P. van der Schoot, "Parity breaking in nematic tactoids," J. Phys.: Condens. Matter **16**, 8835–8850 (2004).

[21] L. Tortora and O. D. Lavrentovich, "Chiral symmetry breaking by spatial confinement in tactoidal droplets of lyotropic chromonic liquid crystals." Proc. Natl. Acad. Sci. U. S. A. **108**, 5163–5168 (2011).

[22] J. Jeong, L. Kang, Z. S. Davidson, P. J. Collings, T. C. Lubensky, and A. G. Yodh, "Chiral structures from achiral liquid crystals in cylindrical capillaries." Proc. Natl. Acad. Sci. U. S. A. **112**, E1837–E1844 (2015).

[23] G. Crawford, D. Allender, and J. Doane, "Surface elastic and molecular-anchoring properties of nematic liquid crystals confined to cylindrical cavities," Phys. Rev. A **45**, 8693–8708 (1992).

[24] V. Koning, B. C. van Zuiden, R. D. Kamien, and V. Vitelli, "Saddle-splay screening and chiral symmetry breaking in toroidal nematics," Soft Matter **10**, 4192–4198 (2014).

[25] Z. S. Davidson, L. Kang, J. Jeong, T. Still, P. J. Collings, T. C. Lubensky, and A. G. Yodh, "Chiral structures and defects of lyotropic chromonic liquid crystals induced by saddle-splay elasticity," Phys. Rev. E **91**, 050501 (2015).

[26] S. Zhou, Y. A. Nastishin, M. M. Omelchenko, L. Tortora, V. G. Nazarenko, O. P. Boiko, T. Ostapenko, T. Hu, C. C. Almasan, S. N. Sprunt, J. T. Gleeson, and O. D. Lavrentovich, "Elasticity of lyotropic chromonic liquid crystals probed by director reorientation in a magnetic field," Phys. Rev. Lett. **109**, 037801 (2012).

[27] N. V. Madhusudana and R. Pratibha, "Elasticity and orientational order in some cyanobiphenyls: Part IV. Reanalysis of the data," Mol. Cryst. Liq. Cryst. **89**, 249–257 (1982).

[28] G. P. Alexander, B. G.-g. Chen, E. A. Matsumoto, and R. D. Kamien, "Colloquium: Disclination loops, point defects, and all that in nematic liquid crystals," Rev. Mod. Phys. **84**, 497 (2012).

[29] P. C. Mushenheim, R. R. Trivedi, H. H. Tuson, D. B. Weibel, and N. L. Abbott, "Dynamic self-assembly of motile bacteria in liquid crystals," Soft Matter **10**, 88–95 (2014).

[30] S. Zhou, A. Sokolov, O. D. Lavrentovich, and I. S. Aranson, "Living liquid crystals," in *Proc. Natl. Acad. Sci. U. S. A.* (2014).

[31] J. Jeong, G. Han, A. T. C. Johnson, P. J. Collings, T. C. Lubensky, and A. G. Yodh, "Homeotropic Alignment of Lyotropic Chromonic Liquid Crystals Using Noncovalent Interactions," Langmuir **30**, 2914–2920 (2014).

[32] V. G. Nazarenko, O. P. Boiko, H.-S. Park, O. M. Brodyn, M. M. Omelchenko, L. Tortora, Y. A. Nastishin, and O. D. Lavrentovich, "Surface alignment and anchoring transitions in nematic lyotropic chromonic liquid crystal," Phys. Rev. Lett. **105**, 017801 (2010).

[33] C. Williams, P. Pierański, and P. E. Cladis, "Nonsingular $S = +1$ screw disclination lines in nematics," Phys. Rev. Lett. **29**, 90–92 (1972).

[34] P. E. Cladis and M. Kleman, "Non-singular disclinations of strength $S = +1$ in nematics," J. Phys. France **33**, 591–598 (1972).

[35] R. B. Meyer, "On the existence of even indexed disclinations in nematic liquid crystals," Philos. Mag. **27**, 405–424 (1973).

[36] C. Williams and Y. Bouligand, "Fils et disinclinaisons dans un nématique en tube capillaire," J. Phys. France **35**, 589–593 (1974).

[37] H. Hakemi, "The determination of the elastic constants of a series of *n*-alkylcyanobiphenyls by anisotropy of turbidity," J. Chem. Phys. **78**, 1513–1518 (1983).

[38] F. Giavazzi, S. Crotti, A. Speciale, F. Serra, G. Zanchetta, V. Trappe, M. Buscaglia, T. Bellini, and R. Cerbino, "Viscoelasticity of nematic liquid crystals at a glance," Soft Matter **10**, 3938–3949 (2014).

[39] S. Zhou, K. Neupane, Y. A. Nastishin, A. R. Baldwin, S. V. Shiyanovskii, O. D. Lavrentovich, and S. Sprunt, "Elasticity, viscosity, and orientational fluctuations of a lyotropic chromonic nematic liquid crystal disodium cromoglycate ," Soft Matter **10**, 6571–6581 (2014).

[40] A. Sparavigna, O. Lavrentovich, and A. Strigazzi, "Periodic stripe domains and hybrid-alignment regime in nematic liquid crystals: Threshold analysis." Phys. Rev. E **49**, 1344–1352 (1994).

[41] O. D. Lavrentovich, "Geometrical anchoring at an inclined surface of a liquid crystal," Phys. Rev. A **46**, R722–R725 (1992).

[42] V. Fréedericksz and V. Zolina, "Forces causing the orientation of an anisotropic liquid," Trans. Faraday Soc. **29**, 919–930 (1933).

[43] P. P. Karat and N. V. Madhusudana, "Elastic and optical properties of some 4'-*n*-alkyl-4-cyanobiphenyls," Mol. Cryst. Liq. Cryst. **36**, 51–64 (1976).

[44] P. P. Karat and N. V. Madhusudana, "Elasticity and orientational order in some 4'-*n*-alkyl-4-cyanobiphenyls: Part II," Mol. Cryst. Liq. Cryst. **40**, 239–245 (1977).

[45] A. Bogi and S. Faetti, "Elastic, dielectric and optical constants of 4'-pentyl-4-cyanobiphenyl," Liq. Cryst. **28**, 729–739 (2001).

[46] J. Nehring and A. Saupe, "On the elastic theory of uniaxial liquid crystals," J. Chem. Phys. **54**, 337–343 (1971).

[47] G. P. Crawford and S. Zumer, "Saddle-splay elasticity in nematic liquid crystals," Int. J. Mod. Phys. B **9**, 2469–2514 (1995).

[48] V. Schmidt, "Normal-distortion-mode approach to liquid crystal elastic energy," Phys. Rev. Lett. **64**, 535–538 (1990).

[49] A. A. Joshi, J. K. Whitmer, O. Guzmán, N. L. Abbott, and J. J. de Pablo, "Measuring liquid crystal elastic constants with free energy perturbations," Soft Matter **10**, 882–893 (2014).

[50] M. Schadt, K. Schmitt, V. Kozinkov, and V. Chigrinov, "Surface-induced parallel alignment of liquid crystals by linearly polymerized photopolymers," Jpn. J. Appl. Phys. **31**, 2155–2164 (1992).

[51] N. Zimmermann, G. Jünnemann-Held, P. J. Collings, and H.-S. Kitzerow, "Self-organized assemblies of colloidal particles obtained from an aligned chromonic liquid crystal dispersion," Soft Matter **11**, 1547–1553 (2015).

[52] B.-w. Lee and N. A. Clark, "Alignment of liquid crystals with patterned isotropic surfaces." Science **291**, 2576–2580 (2001).

[53] E. Willman, L. Seddon, M. Osman, A. Bulak, R. James, S. E. Day, and F. A. Fernandez, "Liquid crystal alignment induced by micron-scale patterned surfaces," Phys. Rev. E **89**, 052501 (2014).

[54] C. K. McGinn, L. I. Laderman, N. Zimmermann, H.-S. Kitzerow, and P. J. Collings, "Planar anchoring strength and pitch measurements in achiral and chiral chromonic liquid crystals using 90-degree twist cells," Phys. Rev. E **88**, 062513 (2013).

[55] R. Kamien, "The geometry of soft materials: A primer," Rev. Mod. Phys. **74**, 953–971 (2002).

[56] E. Pairam, J. Vallamkondu, V. Koning, B. C. van Zuiden, P. W. Ellis, M. A. Bates, V. Vitelli, and A. Fernandez-Nieves, "Stable nematic droplets with handles," Proc. Natl. Acad. Sci. U. S. A. **110**, 9295–9300 (2013).

[57] L. E. Hough, H. T. Jung, D. Krüerke, M. S. Heberling, M. Nakata, C. D. Jones, D. Chen, D. R. Link, J. Zasadzinski, G. Heppke, J. P. Rabe, W. Stocker, E. Körblova, D. M. Walba, M. A. Glaser, and N. A. Clark, "Helical nanofilament phases," Science **325**, 456–460 (2009).

[58] R. Ondris-Crawford, G. Crawford, S. Zumer, and J. Doane, "Curvature-induced configuration transition in confined nematic liquid crystals," Phys. Rev. Lett. **70**, 194–197 (1993).

[59] D. Melzer and F. R. N. Nabarro, "Optical studies of a nematic liquid crystal with circumferential surface orientation in a capillary," Philos. Mag. **35**, 901–906 (1977).

[60] D. W. Allender, G. P. Crawford, and J. W. Doane, "Determination of the liquid-crystal surface elastic constant K_{24}," Phys. Rev. Lett. **67**, 1442–1445 (1991).

[61] R. D. Polak, G. P. Crawford, B. C. Kostival, J. W. Doane, and S. Zumer, "Optical determination of the saddle-splay elastic constant K_{24} in nematic liquid crystals," Phys. Rev. E **49**, R978–R981 (1994).

[62] J. L. Ericksen, "Inequalities in Liquid Crystal Theory," Phys. Fluids **9**, 1205–1207 (1966).

[63] J. D. Pryce, *Numerical Solution of Sturm-Liouville Problems*, Monographs on Numerical Analysis (Claredon Press, Oxford, 1993).

[64] P. Biscari and E. M. Terentjev, "Nematic membranes: Shape instabilities of closed achiral vesicles," Phys. Rev. E **73**, 051706 (2006).

[65] Y. K. Murugesan, D. Pasini, and A. D. Rey, "Microfibril organization modes in plant cell walls of variable curvature: A model system for two dimensional anisotropic soft matter," Soft Matter **7**, 7078–7093 (2011).

[66] P. N. Pusey and W. van Megen, "Phase behaviour of concentrated suspensions of nearly hard colloidal spheres," Nature **320**, 340–342 (1986).

[67] L. Onsager, "The effects of shape on the interaction of colloidal particles," Ann. N. Y. Acad. Sci. **51**, 627–659 (1949).

[68] D. Frenkel, H. N. W. Lekkerkerker, and A. Stroobants, "Thermodynamic stability of a smectic phase in a system of hard rods," Nature **332**, 822–823 (1988).

[69] M. D. Eldridge, P. A. Madden, and D. Frenkel, "Entropy-driven formation of a superlattice in a hard-sphere binary mixture," Nature **365**, 35–37 (1993).

[70] M. Adams, Z. Dogic, S. L. Keller, and S. Fraden, "Entropically driven microphase transitions in mixtures of colloidal rods and spheres," Nature **393**, 349–352 (1998).

[71] D. G. A. L. Aarts, M. Schmidt, and H. N. W. Lekkerkerker, "Direct visual observation of thermal capillary waves." Science **304**, 847–850 (2004).

[72] U. Gasser, E. R. Weeks, A. Schofield, P. N. Pusey, and D. A. Weitz, "Real-space imaging of nucleation and growth in colloidal crystallization." Science **292**, 258–262 (2001).

[73] A. P. Gast, C. K. Hall, and W. B. Russel, "Polymer-induced phase separations in nonaqueous colloidal suspensions," J. Colloid Interface Sci. **96**, 251–267 (1983).

[74] H. N. W. Lekkerkerker, W. C. K. Poon, P. N. Pusey, A. Stroobants, and P. B. Warren, "Phase Behaviour of Colloid + Polymer Mixtures," Europhys. Lett. **20**, 559–564 (2007).

[75] E. Weeks, J. Crocker, A. Levitt, A. Schofield, and D. Weitz, "Three-dimensional direct imaging of structural relaxation near the colloidal glass transition," Science **287**, 627–631 (2000).

[76] B. Alberts, A. Johnson, J. Lewis, M. Raff, K. Roberts, and P. Walter, *Molecular Biology of the Cell: Reference Edition*, 5th ed. (Garland Science, New York, 2008).

[77] E. Barry and Z. Dogic, "Entropy driven self-assembly of nonamphiphilic colloidal membranes." Proc. Natl. Acad. Sci. U. S. A. **107**, 10348–10353 (2010).

[78] Y. Yang, E. Barry, Z. Dogic, and M. F. Hagan, "Self-assembly of 2D membranes from mixtures of hard rods and depleting polymers," Soft Matter **8**, 707–714 (2012).

[79] P. Sharma, A. Ward, T. Gibaud, M. F. Hagan, and Z. Dogic, "Hierarchical organization of chiral rafts in colloidal membranes," Nature **513**, 77–80 (2014).

[80] D. Lingwood and K. Simons, "Lipid rafts as a membrane-organizing principle," Science **327**, 46–50 (2009).

[81] E. Barry, D. Beller, and Z. Dogic, "A model liquid crystalline system based on rodlike viruses with variable chirality and persistence length," Soft Matter **5**, 2563–2570 (2009).

[82] K. R. Purdy, Z. Dogic, S. Fraden, A. Rühm, L. Lurio, and S. G. J. Mochrie, "Measuring the nematic order of suspensions of colloidal fd virus by x-ray diffraction and optical birefringence," Phys. Rev. E **67**, 031708 (2003).

[83] Z. Dogic and S. Fraden, "Cholesteric phase in virus suspensions," Langmuir **16**, 7820–7824 (2000).

[84] L. Kang, T. Gibaud, Z. Dogic, and T. C. Lubensky, "Entropic forces stabilize diverse emergent structures in colloidal membranes," arXiv (2015), 1507.00746v1 .

[85] S. Asakura and F. Oosawa, "On interaction between two bodies immersed in a solution of macromolecules," J. Chem. Phys. **22**, 1255–1256 (1954).

[86] S. Asakura and F. Oosawa, "Interaction between particles suspended in solutions of macromolecules," J. Polym. Sci. **33**, 183–192 (1958).

[87] A. W. C. Lau, A. Prasad, and Z. Dogic, "Condensation of isolated semi-flexible filaments driven by depletion interactions," Europhys. Lett. **87**, 48006 (2009).

[88] E. Barry, Z. Dogic, R. B. Meyer, R. A. Pelcovits, and R. Oldenbourg, "Direct measurement of the twist penetration length in a single smectic A layer of colloidal virus particles," J. Phys. Chem. B **113**, 3910–3913 (2009).

[89] T. Gibaud, E. Barry, M. J. Zakhary, M. Henglin, A. Ward, Y. Yang, C. Berciu, R. Oldenbourg, M. F. Hagan, D. Nicastro, R. B. Meyer, and Z. Dogic, "Reconfigurable self-assembly through chiral control of interfacial tension." Nature **481**, 348–351 (2012).

[90] R. Viswanathan, J. A. Zasadzinski, and D. K. Schwartz, "Spontaneous chiral symmetry breaking by achiral molecules in a Langmuir–Blodgett film," Nature **368**, 440–443 (1994).

[91] D. Pettey and T. C. Lubensky, "Stability of texture and shape of circular domains of Langmuir monolayers," Phys. Rev. E **59**, 1834–1845 (1999).

[92] M. J. Zakhary, T. Gibaud, C. N. Kaplan, E. Barry, R. Oldenbourg, R. B. Meyer, and Z. Dogic, "Imprintable membranes from incomplete chiral coalescence," Nat. Commun. **5** (2014).

[93] D. Frenkel, "Order through disorder: Entropy strikes back," Phys. World **6**, 24–25 (1993).

[94] C. B. Allendoerfer, "Steiner's formulae on a general S^{n+1}," Bull. Amer. Math. Soc. **54**, 128–135 (1948).

[95] K. Zhao and T. G. Mason, "Suppressing and enhancing depletion attractions between surfaces roughened by asperities," Phys. Rev. Lett. **101**, 148301 (2008).

[96] D. J. Kraft, R. Ni, F. Smallenburg, M. Hermes, K. Yoon, D. A. Weitz, A. van Blaaderen, J. Groenewold, M. Dijkstra, and W. K. Kegel, "Surface roughness directed self-assembly of patchy particles into colloidal micelles." Proc. Natl. Acad. Sci. U. S. A. **109**, 10787–10792 (2012).

[97] D. B. DuPré, "Temperature, concentration, and molecular weight dependence of the twist elastic constant of cholesteric poly-γ-benzyl-L-glutamate," J. Chem. Phys. **63**, 143–148 (1975).

[98] F. Leenhouts, F. Van der Woude, and A. J. Dekker, "The twist elastic constant as a function of temperature for nematic MBBA," Phys. Lett. **58**, 242–244 (1976).

[99] C. E. Ioan, T. Aberle, and W. Burchard, "Structure properties of dextran. 2. Dilute solution," Macromolecules **33**, 5730–5739 (2000).

[100] J. K. Armstrong, R. B. Wenby, H. J. Meiselman, and T. C. Fisher, "The hydrodynamic radii of macromolecules and their effect on red blood cell aggregation." Biophys. J. **87**, 4259–4270 (2004).

[101] D. S. Banks and C. Fradin, "Anomalous diffusion of proteins due to molecular crowding." Biophys. J. **89**, 2960–2971 (2005).

[102] M. Born and E. Wolf, *Principles of Optics*, 7th ed. (Cambridge University Press, Cambridge, 2005).

[103] R. Cush, P. S. Russo, Z. Kucukyavuz, Z. Bu, D. Neau, D. Shih, S. Kucukyavuz, and H. Ricks, "Rotational and translational diffusion of a rodlike virus in random coil polymer solutions," Macromolecules **30**, 4920–4926 (1997).

[104] F. Tombolato, A. Ferrarini, and E. Grelet, "Chiral nematic phase of suspensions of rodlike viruses: Left-handed phase helicity from a right-handed molecular helix," Phys. Rev. Lett. **96**, 258302 (2006).

[105] J. C. Slater, "Wave functions in a periodic potential," Phys. Rev. **51**, 846–851 (1937).

[106] P. Bak, "Commensurate phases, incommensurate phases and the devil's staircase," Rep. Prog. Phys. **45**, 587–629 (1982).

[107] M. B. Partensky, "The circle of Apollonius and its applications in introductory physics," Phys. Teach. **46**, 104–108 (2008).

[108] J. A. Campagna, K. W. Miller, and S. A. Forman, "Mechanisms of actions of inhaled anesthetics," N Engl J Med **348**, 2110–2124 (2003).

[109] G. S. Lysko, J. L. Robinson, R. Casto, and R. A. Ferrone, "The stereospecific effects of isoflurane isomers in vivo." Eur. J. Pharmacol. **263**, 25–29 (1994).

[110] R. Dickinson, I. White, W. R. Lieb, and N. P. Franks, "Stereoselective loss of righting reflex in rats by isoflurane." Anesthesiology **93**, 837–843 (2000).

[111] A. Won, I. Oh, M. J. Laster, J. Popovich, E. I. Eger, II, and J. M. Sonner, "Chirality in anesthesia I: minimum alveolar concentration of secondary alcohol enantiomers," Anesth. Analg. **103**, 81–84 (2006).

[112] M. Weinrich, H. Nanda, D. L. Worcester, C. F. Majkrzak, B. B. Maranville, and S. M. Bezrukov, "Halothane changes the domain structure of a binary lipid membrane," Langmuir **28**, 4723–4728 (2012).

[113] M. Weinrich and D. L. Worcester, "Xenon and other volatile anesthetics change domain structure in model lipid raft membranes," J. Phys. Chem. B **117**, 16141–16147 (2013).